Separation control in low pressure turbines using plasma actuators with passing wakes

A DISSERTATION
SUBMITTED TO THE FACULTY OF THE GRADUATE SCHOOL
OF THE UNIVERSITY OF MINNESOTA
BY

Debashish Burman

IN PARTIAL FULFILLMENT OF THE REQUIREMENTS
FOR THE DEGREE OF
DOCTOR OF PHILOSOPHY

Advisor: Terrence W. Simon

September, 2013

Acknowledgements

The funding for this work by NASA Glenn Research Center (NASA Cooperative Agreement NNX07AB94A), and the support of Philip Poinsatte and David Ashpis, both of NASA, is gratefully acknowledged.

I would like to thank my advisor, Professor Terry Simon, for his guidance, encouragement, and endless patience over the years. I would also like to thank Professor Francis Kulacki and Professor Alex Lubet (University of Minnesota), and Professor John Abraham (University of St. Thomas) for their strong support.

I am indebted to the exceptional expertise of the machinists at the University of Minnesota: Pat Nelsen, Dave Hultman, and Robin Russell.

It has been my privilege to learn, teach, collaborate, and conduct research with many remarkable individuals during my graduate schools years – thank you all.

Abstract

A Dielectric Barrier Discharge (DBD) plasma actuator is operated in flow over the suction surface of a Pack-B Low Pressure Turbine (LPT) airfoil at a Reynolds number of 50,000 (based on exit velocity and suction surface length) and inlet free-stream turbulence intensity of 2.5%.

Preliminary characterization studies were made of the effect of varying actuator pulsing frequency and duty cycle, actuator edge effects, and orientation of the actuator with the flow. Flow control was demonstrated with the actuator imparting momentum opposite to the stream-wise flow direction, showing that it is possible to use disturbances alone to destabilize the flow and effect transition. No frequencies of strong influence were found over the range tested, indicating that a broad band of effective frequencies exists. Edge effects were found to considerably enhance separation control.

Total pressure measurements of the flow without passing wakes were taken using a glass total-pressure tube. Corrections for streamline displacement due to shear and wall effects were made, and comparisons with previous hot-wire measurements were used to validate data. Performance features of conventional two-electrode and a novel three-electrode actuator configuration were compared.

Hot-wire anemometry was used to take time-varying ensemble-averaged near-wall velocity measurements of the flow with periodic passing wakes. Corrections were made for near-wall effects, temperature effects, and interference of the electric field. The wakes were generated by a wake generator mechanism located upstream of the airfoil passage.

The near-suction-surface total pressure field (flow without wakes) and velocity field (flow with wakes) in the trailing part of the airfoil passage, and the wall-normal gradient of these quantities, were used to demonstrate effective prevention of flow separation

using the plasma actuator. Both flows (with and without passing wakes) showed fully attached flow (or very thin separation zones) when the actuator was activated. The flow with passing wakes and the actuator on showed relatively little time variation in the boundary layer, and qualitative similarities to the corresponding flow without passing wakes and with the actuator on were noted.

Table of Contents

List of Tables vi

List of Figures vii

1. Introduction 1

1.1. Motivation 1

1.2. Background and relevant literature 3

1.3. Scope 41

2. Experimental test facility 42

2.1. Low-speed wind tunnel 42

2.2. Low pressure turbine airfoil passage 46

2.3. Wake Generator 48

2.4. Plasma Actuator 53

2.5. Data Acquisition equipment 56

2.6. Ozone-related safety equipment 57

3. Instrumentation, experimental procedures, and data processing 59

3.1. Background 59

3.2. Total pressure measurements 60

3.3. Hot-wire anemometry 69

4. Preliminary experimental characterization 79

4.1. Effect of varying pulsing frequency and duty cycle 79

4.2. Effect of aligned and reversed actuator orientation 84

4.3. Span-wise variation and edge effects 90

5. Steady flow results 100

5.1. Actuator construction, configuration, and operating parameters 100

5.2. Results and discussion 101

6. Unsteady flow results 108

6.1. Background 108

6.2. Measurement considerations 108
6.3. Results and discussion 111
7. Discussion on aspects of flow control physics 137
8. Conclusions and recommendations 148
Bibliography 152
Appendix – Dielectric selection for the plasma actuator 165

List of Tables

Table 1-1 Conditions relating to timescales of initiation and maximum growth of a starting vortex, from the literature 34
Table 2-1 Components of the wake generator driving mechanism 49
Table 2-2 Pack-B turbine passage parameters 51
Table 2-3 Specification of the high voltage amplifiers used in this study 55
Table 4-1 Experimental parameters for study on variation of pulsing frequency and duty cycle 80
Table 4-2 Experimental parameters for studies on actuator orientation and edge effects 84

List of Figures

Figure 1-1 Variation of Reynolds number through the engine (Hourmouziadis, 1989) 2
Figure 1-2 LPT loss co-efficients at low Reynolds numbers (Sharma, 1998) 2
Figure 1-3 K-type and H-type natural transition (Criminale et al., 2003) 5
Figure 1-4 Smoke visualization of K-type secondary instability (Samimy et al., 2003) 6
Figure 1-5 Spatial evolution of H-type transition (Sayadi et al., 2011) 7
Figure 1-6 Illustration of natural transition in boundary-layer flow over a flat plate (Kachanov, 1994) 7
Figure 1-7 Transient growth: superposition of two decaying non-orthogonal vectors (Schmid and Henningson, 2001) 10
Figure 1-8 Smoke visualization of a flat plate boundary layer (Boiko et al., 2012) 12
Figure 1-9 Schematic of the bypass transition process (Lundell, 2007) 12
Figure 1-10 Longitudinal backward and forward jets in streaks (Mandal et al., 2010) 13
Figure 1-11 Klebanoff streaks in a separating flow (McAuliffe and Yaras, 2010) 16
Figure 1-12 Passage of wakes, showing distortion of the turbulent kinetic energy field (Stieger and Hodson, 2004) 19
Figure 1-13 Suction surface boundary layer loss vs. Reynolds number (Howell et al., 2000) 19
Figure 1-14 Space-time diagram of unsteady separation and wake-induced transition (Coull and Hodson, 2011) 21
Figure 1-15 Schematic of Vortex Generating Jet (VGJ) injection geometry (Postl et al., 2011) 23
Figure 1-16 Flow structures produced by a jet (Zhang and Zhong, 2010) 24
Figure 1-17 Schematic of actuator; a photograph of the discharge (Corke et al., 2009) 25
Figure 1-18 Actuator in quiescent air: smoke visualization (Enloe et al., 2004) 26
Figure 1-19 Flow visualization showing starting vortex formed after plasma initiation (Whalley and Choi, 2010) 30

Figure 1-20 Evolution of horizontal velocity near the actuator (Kotsonis and Ghaemi, 2012) 32
Figure 1-21 Maximum velocity induced by the actuator vs. time (Whalley and Choi, 2012) 33
Figure 1-22 Effective leading-edge separation control at high angle-of-attack (Post and Corke, 2003) 38
Figure 1-23 A signal timing diagram for pulsed control (Corke et al., 2004) 39
Figure 2-1 Low-speed wind tunnel, development section, and the Pack-B airfoil passage (Simon et al., 2000) 44
Figure 2-2 Rod grid generator (Kaszeta et al., 2003) 45
Figure 2-3 Cascade simulation test section (Kaszeta et al., 2003) 47
Figure 2-4 Pack-B airfoil with steady flow: separation and transition locations (Simon et al., 2000) 48
Figure 2-5 Pack-B turbine passage dimensions (Kaszeta et al., 2003) 50
Figure 2-6 Cross-sectional view of the wake generator (Kaszeta et al., 2003) 51
Figure 2-7 A schematic of the wake generator (Yuan, 1999) 52
Figure 2-8 Motor and push bar mechanism in the wake generator (Yuan, 1999) 53
Figure 2-9 Actuator arrangement for the three-electrode geometry 54
Figure 2-10 Device used for monitoring ozone levels in the test environment 57
Figure 3-1 Glass total pressure tube used for total pressure measurements 61
Figure 3-2 Schematic showing micro-manometer used in present study 62
Figure 3-3 Streamline displacement due to the presence of the wall, and due to shear 64
Figure 3-4 Corrected total pressure tube vs. hot-wire measurements, attached flow 66
Figure 3-5 Sense of the static pressure gradient for re-attaching flow 67
Figure 3-6 Corrected total pressure tube vs. hot-wire data, separated flow 68
Figure 3-7 Hot-wire probe schematic 70
Figure 3-8 Hot-wire calibration apparatus (adapted from Adolfson, 2003) 71
Figure 3-9 Hot-wire calibration curve 71
Figure 3-10 Velocity data showing drop in signal amplitude with actuator on 76

Figure 4-1 Variation of total pressure with duty cycle 80
Figure 4-2 Variation of total pressure with pulsing frequency 83
Figure 4-3 Intermittent actuation timing: actuator orientation and edge effects studies 84
Figure 4-4 Flow response to reversed orientation of actuator 87
Figure 4-5 Wall-normal gradient of total pressure: effect of actuator orientation 88
Figure 4-6 Difference of total pressure: reversed actuator orientation 89
Figure 4-7 Difference of total pressure: aligned actuator orientation. 90
Figure 4-8 Topography of the study of span-wise variation. 91
Figure 4-9 Difference of total pressure at a wall-normal distance of 0.5 mm 93
Figure 4-10 Total pressure at a wall-normal distance of 0.5 mm 94
Figure 4-11 Difference of total pressure at a wall-normal distance of 1.5 mm 95
Figure 4-12 Total pressure at a wall-normal distance of 1.5 mm 96
Figure 4-13 Difference of total pressure at a wall-normal distance of 2.5 mm 97
Figure 4-14 Total pressure at a wall-normal distance of 2.5 mm 98
Figure 5-1 Actuator arrangement for the three-electrode geometry. 101
Figure 5-2 Total pressure with the actuator off and on (two- and three-electrode) 104
Figure 5-3 Wall-normal gradient of total pressure with the actuator off and on (two- and three-electrode) 106
Figure 6-1 Time-averaged structure of a laminar separation bubble (Horton, 1968) 113
Figure 6-2 Velocity field: first one-third of the wake-passing cycle, actuator off 117
Figure 6-3 Velocity field: middle one-third of the wake-passing cycle, actuator off 118
Figure 6-4 Velocity field: final one-third of the wake-passing cycle, actuator off 119
Figure 6-5 Wall-normal velocity gradient: first one-third of the wake-passing cycle, actuator off 120
Figure 6-6 Wall-normal velocity gradient: middle one-third of the wake-passing cycle, actuator off 121
Figure 6-7 Wall-normal velocity gradient: final one-third of the wake-passing cycle, actuator off 122
Figure 6-8 Velocity field: first one-third of the wake-passing cycle, actuator on 123

Figure 6-9 Velocity field: middle one-third of the wake-passing cycle, actuator on 124
Figure 6-10 Velocity field: final one-third of the wake-passing cycle, actuator on 125
Figure 6-11 Wall-normal velocity gradient: first one-third of the wake-passing cycle, actuator on 126
Figure 6-12 Wall-normal velocity gradient: middle one-third of the wake-passing cycle, actuator on 127
Figure 6-13 Wall-normal velocity gradient: final one-third of the wake-passing cycle, actuator on 128
Figure 6-14 Time-varying velocity at s/L_{ss} = 0.703: actuator off and on 129
Figure 6-15 Time-varying wall-normal velocity gradient at s/L_{ss} = 0.703: actuator off and on 130
Figure 6-16 Time-varying velocity at s/L_{ss} = 0.76: actuator off and on 131
Figure 6-17 Time-varying wall-normal velocity gradient at s/L_{ss} = 0.76: actuator off and on 132
Figure 6-18 Time-varying velocity at s/L_{ss} = 0.84: actuator off and on 133
Figure 6-19 Time-varying wall-normal velocity gradient at s/L_{ss} = 0.84: actuator off and on 134
Figure 7-1 Rescaled results: effect of pulsing frequency and duty cycle 146
Figure 7-2 Flow control model based on size and patterns of vortices produced 147
Figure A-1 Actuator during normal operation, and during burn-through failure 168
Figure A-2 Site of the burn-through failure on PET polyester dielectric 169
Figure A-3 Electrical characteristics of the discharge at saturation conditions. 169
Figure A-4 Structure of discharge at saturation, showing coarse, bright streamers 170
Figure A-5 A dielectric sample that was deformed by use of a heat gun, to better conform to the airfoil shape 170
Figure A-6 A replaceable airfoil insert section 170

1. Introduction

1.1. Motivation

The low pressure turbine (LPT) section of an aviation gas turbine engine comprises the last few stages of turbomachinery for work extraction from the flow before it is accelerated through a nozzle and released to the atmosphere. It is a very significant part of the engine in most respects. For instance, the LPT accounts for about 20-30% of the engine weight (Hodson and Howell, 2005). In terms of fuel efficiency, a 1% increase in LPT polytropic efficiency results in a 0.5-1% drop in fuel consumption (Wisler, 1998). In 2002, a 1% reduction in jet fuel consumption was estimated to be worth $1.25M per day (Seifert et al., 2002).

The major loss mechanism in the LPT is flow separation on the suction surface of the blades. In a modern aircraft engine, the LPT is typically constrained to operate at low rotational speed, equal to that of the intake fan. Designed for peak performance under sea-level take-off conditions, the turbine blades experience low chord-based Reynolds numbers (Figure 1-1), typically in the range of 0.5×10^5 to 5×10^5 (Howell, 2000) at cruise conditions at higher altitudes. At these Reynolds numbers, large portions of the suction surface boundary layer of an LPT stage are laminar or transitional, and flow separation is likely.

The drop in lift and increase in losses accompanying separation causes a large drop in efficiency of the LPT (Figure 1-2). A representative component efficiency drop is about 2-7%, with the lower figure representative of commercial aircraft engines, and the higher figure representative of smaller engines at higher altitudes (Hultgren and Ashpis, 2003).

Further exacerbating the likelihood of separation is the drive toward higher aerodynamic loading per turbine blade. Higher loadings per blade permit the turbine designer to employ fewer blades per stage in the turbine, which reduces overall component weight and cost.

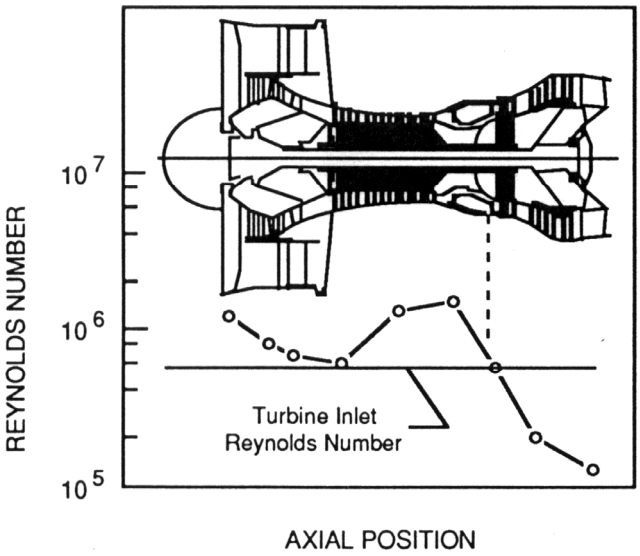

Figure 1-1 Variation of Reynolds number through the engine (Hourmouziadis, 1989)

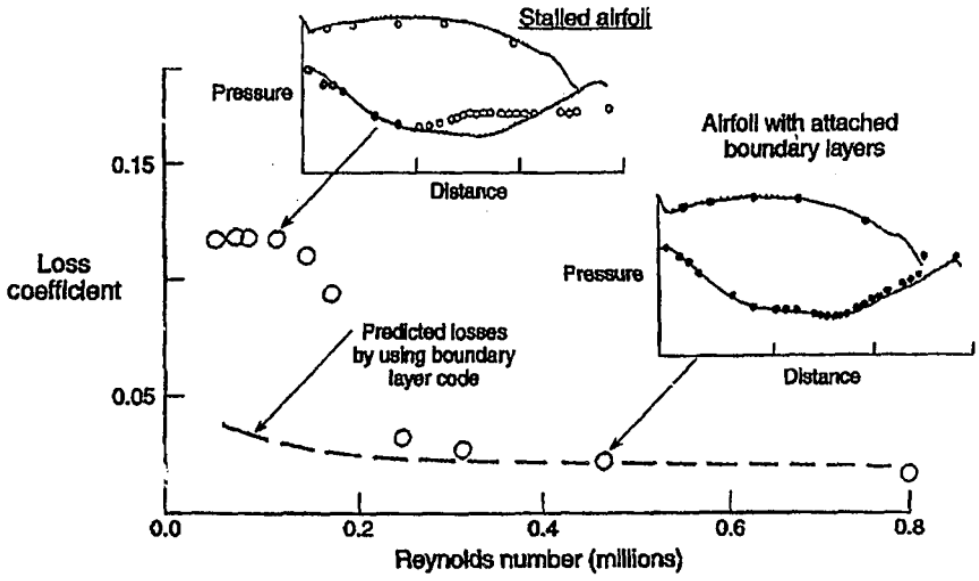

Figure 1-2 Strong increase in loss co-efficient at low Reynolds numbers in low pressure turbine (Sharma, 1998)

Since the laminar or transitional boundary layers that are typically observed on the suction surface of LPT blades are highly prone to separation, efforts to control flow separation in LPTs frequently focus on promoting transition to turbulence.

Depending on the specific geometry of the airfoil, the flow Reynolds number, and the turbulence levels in the free-stream, this transition to turbulence may occur upstream or downstream of separation. If transition occurs upstream of separation, i.e., in the attached boundary layer, then the resulting turbulent boundary layer is much more resistant to separation. If separation occurs first, followed by transition in the separated shear layer, then the enhanced mixing of momentum in the newly-formed turbulent shear layer can lead to partial or complete flow re-attachment.

Adding to the complexity of the flow in this environment are the wakes of upstream stages that are transported through the LPT. These passing wakes interact with the unstable and separation-prone boundary layers on the suction surface of the airfoils, periodically promoting transition, and/or re-attachment.

1.2. Background and relevant literature

Low pressure turbine flow characteristics

The flow field in turbomachinery is complex, being unsteady on time-scales longer than eddy turnover times, and highly three-dimensional, even in the mean. It has been described as a "fluid-dynamical zoo" of flow features (Narasimha, 1998). In a low pressure turbine environment, separation, transition, and re-attachment often occur in the same unsteady flow. Some of these flow features are discussed here.

Large regions of the suction surface airfoil of a low pressure turbine stage are laminar or transitional. Transition to turbulence may occur before or after separation, depending on the airfoil geometry, flow Reynolds number and free-stream turbulence levels. Turbulent boundary layers are more resistant to separation, making attached-flow

separation less likely if transition occurs first. Separated-flow transition is common in LPT flows, where the laminar flow separates, and transition occurs in the separated shear layer. Transition to turbulence in separated shear layers produces enhanced mixing of high- and low-momentum fluid that can lead to partial or complete re-attachment.

Transition to turbulence involves the amplification of initial disturbances that enter as fluctuations. Potential sources of these initial external disturbances include roughness, acoustic disturbances, leading edge effects and geometric discontinuities, wall curvature, vorticity, and free-stream turbulence. The selectivity (or receptivity) of the shear layer determines whether these disturbances decay, or enter the shear layer, amplify and eventually cause transition to turbulence. The vital initial conditions of amplitude, frequency, and phase for breakdown are determined by receptivity (Reed et al., 1996).

Natural transition

Natural transition to turbulence occurs for cases where the initial amplitude of the forcing external disturbance is small, such as in relatively quiet external flows. The initial breakdown to turbulence is dominated by slow, linear growth processes of the primary instabilities, which appear as long, two-dimensional waves. The least stable finite-amplitude two-dimensional wave is commonly referred to as a Tollmien-Schlichting (TS) wave.

When the TS instability amplitudes have grown to about 1-2% of the free-stream velocity, these two-dimensional waves become susceptible to secondary instabilities through the amplification of three-dimensional perturbations. The secondary instability process involves two possible arrangements (Figure 1-3) of span-wise peak-and-valley regions of increased and decreased fluctuation velocity amplitudes, called Λ vortices (the Greek letter lambda, owing to their shape).

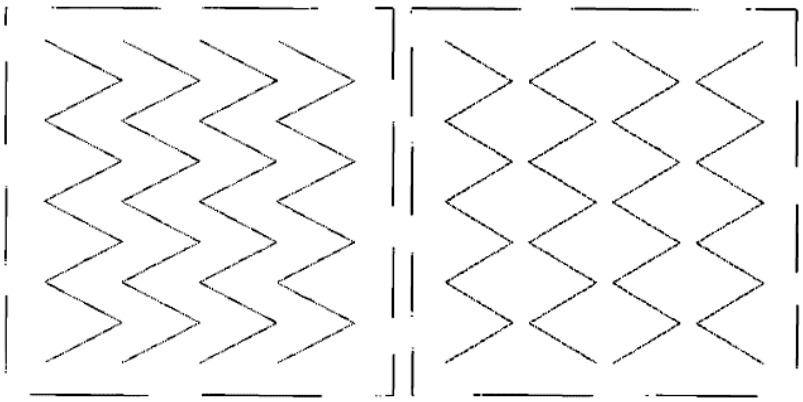

Figure 1-3 A sketch illustrating the pattern of peak-valley structures that form the K-type instability (left), and the H-type instability (right) (Criminale et al., 2003)

K-type ('K' for Klebanoff): the peak-valley aligned arrangement is called the K-type arrangement. This mode is characterized by large (up to 40%), frequent spikes in the stream-wise velocity trace at the peaks. The span-wise scale of the peaks and valleys is of the same order as the stream-wise wavelength of the original TS wave, so the frequency of the secondary fluctuations coincides with the fundamental frequency. Figure 1-4 shows smoke visualization of K-type natural transition.

H-type ('H' for Herbert): the peak-valley staggered arrangement is called the H-type or N-type ('N' for Novosibirsk, or for 'new') arrangement. It is associated with the generation of disturbances of sub-harmonic frequencies, i.e., less than the original disturbing frequency ω. This mode is characterized by the notable absence of spikes associated with the K-type. Instead, a weak signal of the harmonics of the fundamental frequency grows to produce a broad spectrum of low frequency three-dimensional oscillations, including a sub-harmonic frequency. These are then rapidly amplified, and become quasi-random in amplitude, with frequency peaks near $3\omega/2$, $5\omega/2$, $7\omega/2$ etc.

The selected mode depends on the amplitude of the forcing function that generates the TS waves. For low amplitudes, the H-type arrangement is more likely, which corresponds to most natural conditions. For forcing amplitudes greater than about 1% of the free-

stream velocity, the K-type arrangement is more likely. The transition scenarios of both types involving aligned or staggered rows of Λ-vortices evolve into non-linear stages, producing packets of hairpin-shaped eddies. Figure 1-5 from the DNS study of Sayadi et al. (2011) shows these features for the spatial evolution of H-type natural transition. The K-type transition from their work (not shown) produced regions of isolated turbulent spots, which merged to form a fully-developed turbulent flow regime. As seen in the figure, they did not observe distinct isolated turbulent spots in the case of H-type transition.

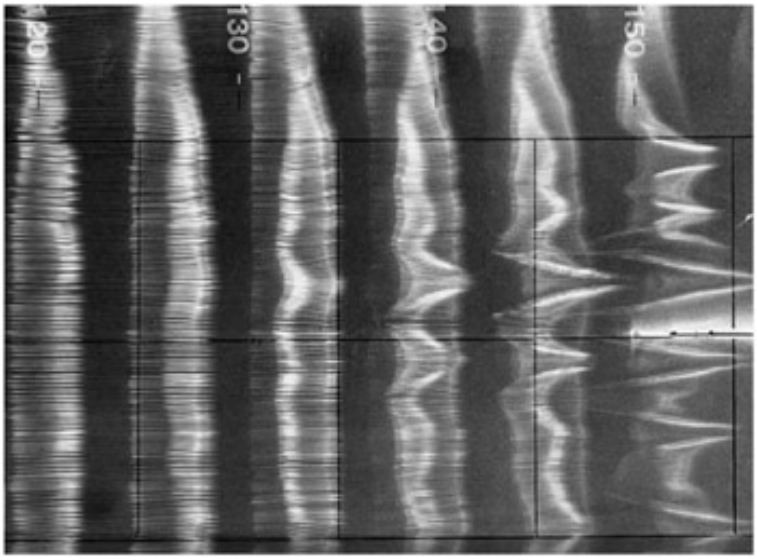

Figure 1-4 Smoke visualization of the ordered peak-valley structures observed in K-type secondary instability, where u` = 1%. 2-D TS waves can be seen at the upstream (left) side of the image. Image by W. S. Saric, from Samimy et al., (2003).

Since the stream-wise extent of the linear regime typically dominates the natural transition process (Figure 1-6), linear stability analysis is commonly used for characterization and prediction. For two-dimensional boundary layers, the linear regime is more pronounced and susceptible to modification by pressure gradients, suction, blowing, or temperature gradients. Three-dimensional boundary layers may exhibit early non-linear distortion (Reed et al., 1996).

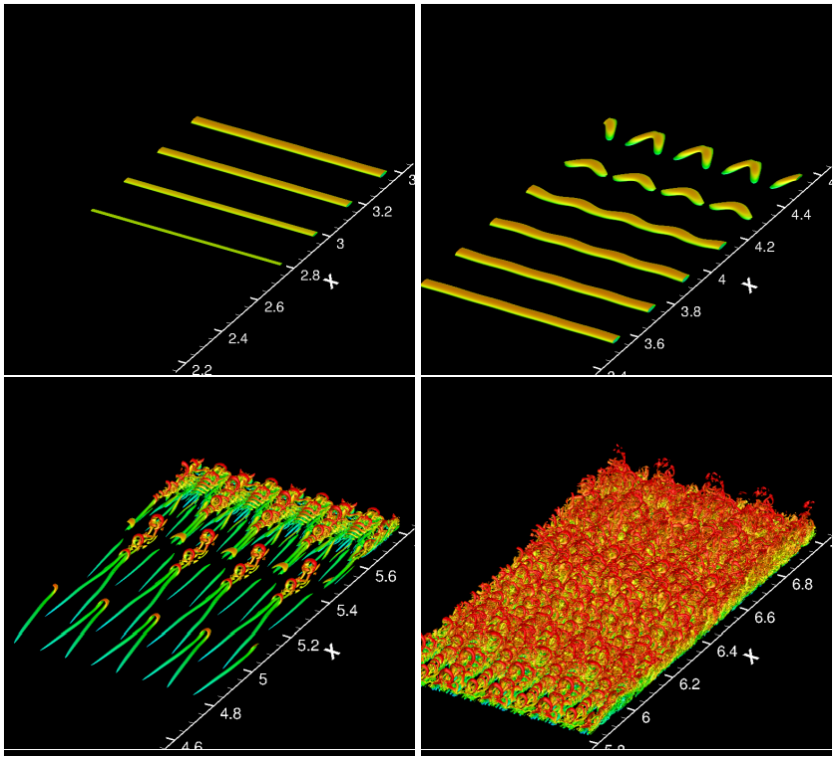

Figure 1-5 Spatial evolution of H-type natural transition, from the DNS of Sayadi et al. (2011). The numbers correspond to $Re_x \times 10^{-5}$.

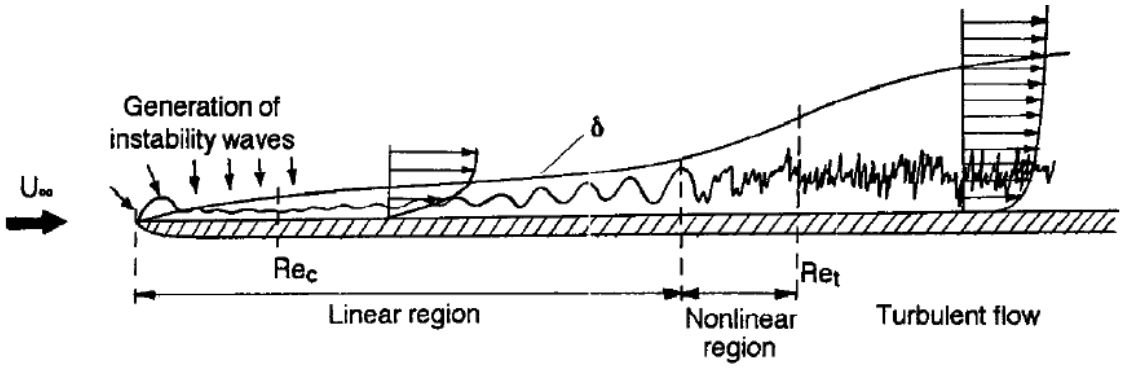

Qualitative sketch of the process of turbulence onset in a boundary layer

Figure 1-6 Illustration of the spatial zones, velocity profiles and representative hot-wire traces of natural transition in boundary-layer flow over a flat plate. (Kachanov, 1994)

The unique experiments of Schubauer and Skramstad (1948) are considered to be the first to demonstrate the physical applicability of linear stability theory, and the existence of TS waves (van Ingen, 2008; Boiko et al., 2012). In a low (0.01 – 0.03%) free-stream turbulence environment, they used a vibrating ribbon stretched in the span-wise direction to generate small disturbances of specific frequencies corresponding to normal modes of the flat-plate boundary layer. Using a hot-wire probe, they studied the evolution of the disturbances downstream, and found good qualitative agreement with the neutral stability curve calculations.

Bypass transition

Under conditions other than controlled laboratory situations, disturbance growth is widely observed at low Reynolds numbers that correspond to damped eigenmodes of the linearized disturbance equations, i.e., subcritical to TS wave growth. This is especially true for situations involving high free-stream turbulence levels (exceeding about 1% (Morkovin, 1984; Suder et al., 1988)), or elements of surface roughness. Morkovin introduced the term "bypass transition" to refer to this strongly amplifying alternative to linear stability theory, since the TS wave mechanism is considered to have been bypassed. This mode of transition is relevant to low pressure turbine flows, where turbulence levels typically range from 2 to 10% (Simon and Kaszeta, 2001).

Role of stream-wise vortices, and the formation of streaks

The existence of an inviscid lift-up mechanism that permits the linear (i.e., algebraic) growth of a disturbance in parallel shear flows was noted by Ellingson and Palm (1975). While viscous effects eventually cause the decay of these disturbances, they can survive extended periods of considerable transient growth, which can alter the base flow significantly, creating a new steady (or quasi-steady) state. This newly altered state may become susceptible to secondary disturbances, to which it may have originally been stable. Additionally, the disturbances may grow to amplitudes where non-linear effects become important. Given the numerous paths leading to transition that it enables,

transient growth is a significant growth mechanism candidate in several examples of bypass transition. This includes flows that are unconditionally stable to TS disturbances (e.g., plane Couette and Poiseuille pipe flows), as well as subcritical transition in flows that are otherwise susceptible to TS disturbances (such as Blasius flows).

As pointed out by Reshotko and Tumin (2006), optimal disturbances for transient growth involved in bypass transition have a "decided three-dimensionality." It is also well recognized that the late stages of natural transition involve strong three-dimensionality. Squire's theorem, which states that for every three-dimensional disturbance, there exists a more unstable two-dimensional disturbance at a lower Reynolds number, caused much of the early work in stability to ignore three-dimensional effects. This lasted until the observation of turbulent spots by Emmons (Andersson, 1999). Butler and Farrell (1992) attribute the misreading of Squire's theorem to its frequently overlooked limitation of considering only a single eigenmode. A combination of non-orthogonal modes can lead to much stronger transient growth of three-dimensional disturbances, as compared to two-dimensional ones. Figure 1-7 illustrates the transient disturbance growth that can occur if the coupled decaying modes are non-orthogonal.

Optimal initial disturbances correspond to those that undergo maximum transient growth, and prolonged existence (in time or space) before undergoing viscous decay. Transient growth is largest for disturbances that are span-wise periodic, with low stream-wise wavenumbers or frequencies. For a number of wall bounded flows, the optimal disturbances capable of the greatest growth have been found to consist of stream-wise vortices (see, for e.g., Butler and Farrell, 1992; Fransson et al., 2004; Schmid and Henningson, 2001; Boiko et al., 2012). Stream-wise vortices are effective means of transporting momentum across the shear layer: low momentum fluid away from the wall, and high momentum fluid towards the wall. This re-distribution of disturbance kinetic energy is large relative to the decay associated with the weak viscous damping

experienced by the stream-wise vortex. As a result, even weak stream-wise vortices evolve to produce strong quasi-stationary longitudinal streaks, which are span-wise variations of stream-wise velocity.

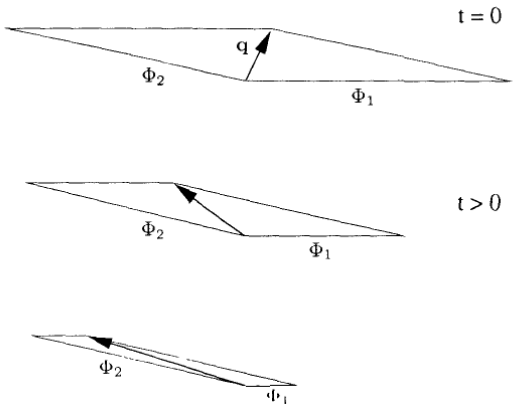

Figure 1-7 Sketch illustrating the possibility of transient growth due to superposition of two vectors decaying at different rates, if they are not orthogonal. (Schmid and Henningson, 2001)

The low-speed streaks correspond to the vortex motion moving fluid away from the wall; the high-speed streaks correspond to vortex motion toward the wall. Relative to the local mean flow, Jacobs and Durbin (2001) considered the positive and negative stream-wise velocity fluctuations to be high-speed forward (relative to the local flow) jets that occur near the wall, and low-speed backward jets that lift away from the wall, respectively. The streaky structures oscillate slowly in the boundary layer (Fransson et al., 2004), as well as meander in the span-wise direction (Mandal et al., 2010) as they continue to spatially grow in stream-wise velocity amplitude and stream-wise length. Due to the thinning and thickening effect produced on the boundary layer, the streaks were called "breathing modes" by Klebanoff. Others have referred to them as "Klebanoff modes." These streaks commonly appear in transition experiments, and are ubiquitous in cases with high free-stream turbulence. As Andersson (1999) finds for the spatial evolution of algebraic disturbances, "almost any steady initial disturbance will develop into a stream-wise streak given a large enough Reynolds number."

For a Blasius boundary layer, the streaks have a span-wise scale of the order of the boundary layer thickness (see Fransson et al., 2004, for example). Figure 1-8 shows the flow visualization results of a flat plate flow undergoing natural transition, and bypass transition due to elevated free-stream disturbance levels. Figure 1-9 is a schematic of the latter process.

Late stages of bypass transition: breakdown of streaks

The stream-wise streaks found in bypass transition have been observed to become wavy prior to their breakdown and formation of turbulent spots. Some researchers (for example, Asai et al., 2002; Brandt et al., 2004; Mans et al., 2007) have found that the waviness can have a sinuous or varicose nature, associated with secondary instability. Brandt et al. (2004) noted that the sinuous-like breakdown mode is driven by span-wise shear, while the varicose mode is driven by wall-normal shear. The sinuous mode due to span-wise oscillation of the low speed streaks is considered by some researchers (for example, Andersson et al., 2001; Asai et al., 2002) to be the more unstable mode.

Zaki and Durbin (2005) observed from their DNS results that the site of the breakdown process is associated with the near-free-stream edge of the lifted up backward jets. The PIV measurements of Mandal et al. (2010) show kink-like patterns and vortex shedding from this oscillating high-shear region, as in Figure 1-10.

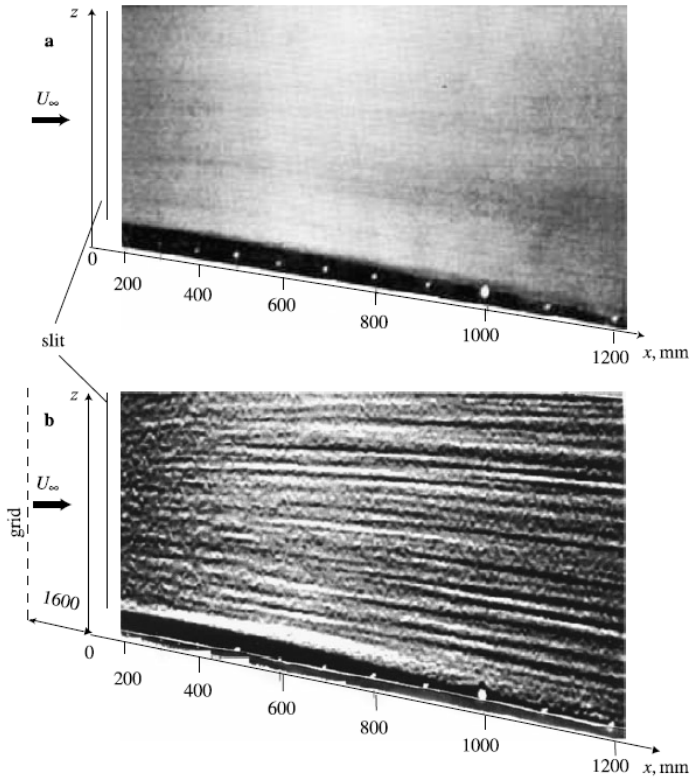

Figure 1-8 Smoke visualization (Matsubara et al., 1996) of a flat plate boundary layer at U_∞ = 6 m/s, with FSTI ≤ 0.02% (top), and FSTI = 1.5% (bottom). Adapted from Boiko et al. (2012).

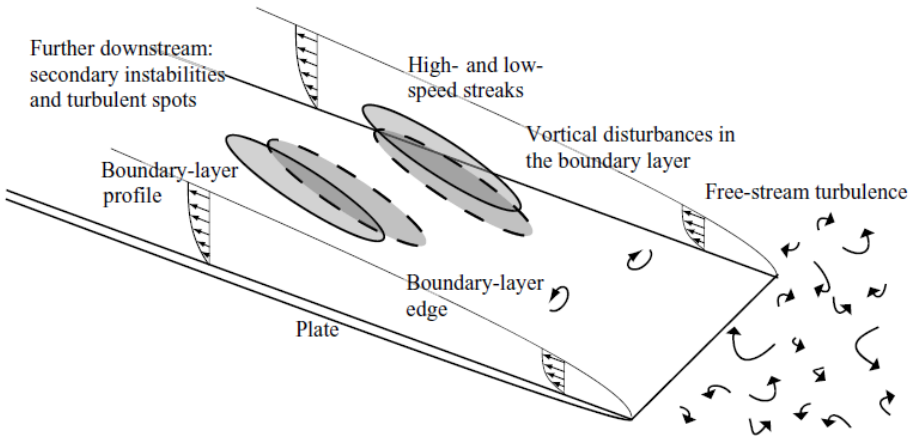

Figure 1-9 Schematic of the bypass transition process due to elevated free-stream turbulence. (Lundell, 2007)

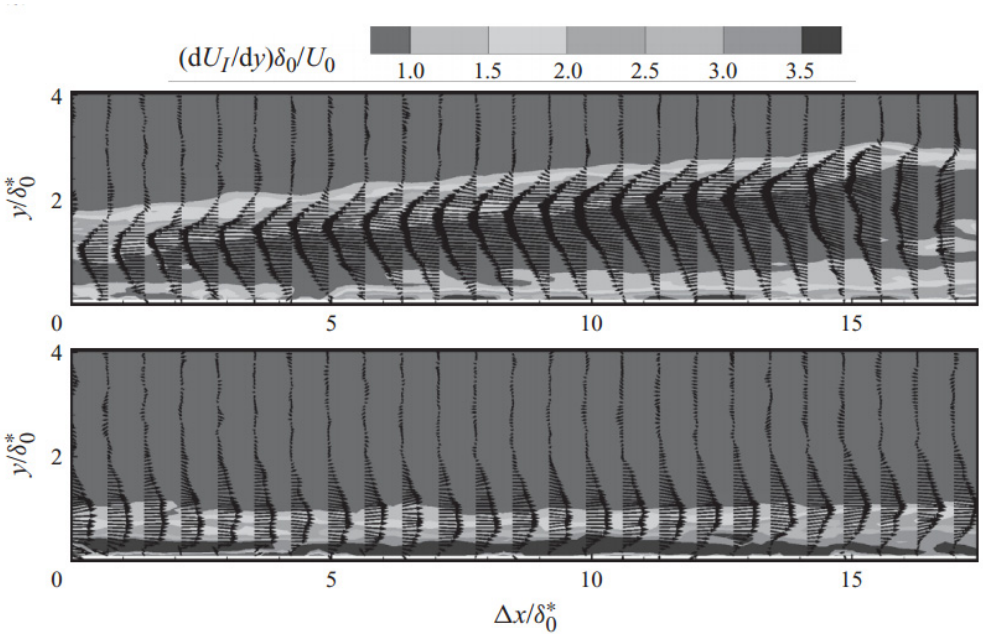

Figure 1-10 Longitudinal backward and forward jets found in streaks. Fluctuating velocity vectors are marked over the normalized instantaneous shear. Backward jets rise towards the edge of the thick and inclined shear layer; forward jets form a thin shear layer near the wall. PIV measurements of Mandal et al. (2010).

From DNS results of a study on bypass transition in a boundary layer, Zaki and Durbin (2005) found that the combination of one low frequency mode and one high frequency mode of free-stream turbulence was sufficient to generate streaks as well as trigger transition to turbulence. In contrast, they found that two low frequency modes could generate streaks, but could not produce induce further breakdown to turbulence. Based on this, they suggested that both low and high frequency components of free-stream turbulence are essential for breakdown to turbulence, and promote shear layer instability at different stages of the transition process. In a phenomenon called shear-sheltering, low frequency disturbance modes from the free-stream are able to penetrate the shear layer. While high frequency disturbances experience rapid decay, the low frequency modes that were effective at entering generate Klebanoff breathing modes within the shear layer, in the form of forward and backward jet-like structures. While the forward jets remain close to the wall, the backward jets experience lift-up due to upward

displacement of low momentum fluid from the bottom of the shear layer. The tops of these backward jets rise to the top of the shear layer, where they produce inflections that are exposed to the free-stream. Interaction of the inflectional profiles with the high frequency disturbances from the free-stream trigger Kelvin-Helmholtz type instabilities, which grow to produce turbulent spots. The spots rapidly grow as they are convected downstream, and merge to produce full turbulence.

Tollmien-Schlichting waves have been difficult to detect in experiments where the free-stream turbulence levels exceeded 1%, and natural and bypass transition have long been studied separately. Studies (Liu et al., 2008; Hughes and Walker, 2001), however, suggest that both mechanisms may co-exist, and interact. Fransson et al. (2005) experimentally confirmed previous numerical predictions that streaks of moderate amplitudes associated with bypass transition can stabilize TS wave instabilities to the point of complete suppression.

Transition mechanisms in laminar separation bubbles

Under low free-stream turbulence levels, separated shear layers undergo transition through their inviscid Kelvin-Helmholtz (KH) instability to disturbances (McAuliffe and Yaras, 2010). The disturbances grow and lead to roll-up of the shear layer into discrete span-wise vortices, which may show grouping behavior. The span-wise vortices eventually break down to small-scale turbulence. Recent investigations indicate that the frequency of the primary inviscid KH mechanism is very close to the dominant Tollmien-Schlichting (TS) frequency of the pre-separation boundary layer, suggesting the possibility of interaction between the TS structures found in the attached boundary layer with the inviscid KH instability after separation. Brinkerhoff and Yaras (2011) conducted a DNS study of separating flow under low free-stream conditions. The two-dimensional span-wise TS waves in the pre-separation boundary layer evolved into Λ-vortices, as expected. The amplitude of stream-wise vorticity associated with the legs of these vortices remained low and constant while the flow decelerated before separation, but

underwent strong growth as they were convected into the separated shear layer. The coherent span-wise shedding vortices of the separated shear layer associated with the inviscid KH instability showed a span-wise non-uniformity consistent with these stream-wise vortices from the pre-separation flow field.

The visualizations from the Large Eddy Simulations of Rao et al. (2013) with laminar (i.e., low free-stream turbulence) inflow show similar characteristics: the large coherent span-wise vortices were two-dimensional as they were shed by the separated shear layer, but continued to interact with the stream-wise hairpin vortices beneath that originated upstream of separation. The span-wise waviness produced in the shed vortex amplified, leading to breakdown to smaller structures, and finally turbulent re-attachment.

Viscous instabilities may also influence the transition process for cases of very thin separation bubbles, and/or cases with large levels of reversed flow. The latter case of strong reversed (greater than about 15-20% of free-stream velocity, from Alam and Sandham, 2000) flow may also lead to absolute instability, where the disturbances from the flow in the downstream part of the bubble may propagate upstream, and produce a self-sustaining unstable situation. Levels of flow reversal found in airfoil laminar separation bubbles are usually much lower, keeping the instability convective in nature (McAuliffe and Yaras, 2010).

At high free-stream turbulence levels, streak formation occurs in the attached boundary layer upstream of separation. In the adverse pressure gradient of the shear flow prior to separation, the backward or low-speed streaks dominate the field, and the laminar stream-wise fluctuation levels of the streaks can be as high as 25% of the local free-stream velocity. Localized secondary instability produced by the strong shear of the streaks leads to the formation of turbulent spots in the separated shear layer. Figure 1-11 from the numerical simulations of McAuliffe and Yaras (2010) illustrates these features.

Despite the difference in physical path to transition relative to the low free-stream turbulence case, the characteristic frequency of this secondary instability is found to agree well with that of the inviscid KH mechanism (McAuliffe and Yaras, 2010).

As discussed previously, an alternative physical mechanism for bypass transition turbulent spot formation from the work of Zaki and Durbin (2005) proposes that the tops of the backward jets of the streaks make the outer (adjacent to the free-stream) shear layer unstable to KH disturbances. The backward jets are those parts of the streaky structures which are formed due to upward displacement of low-speed, near-wall fluid.

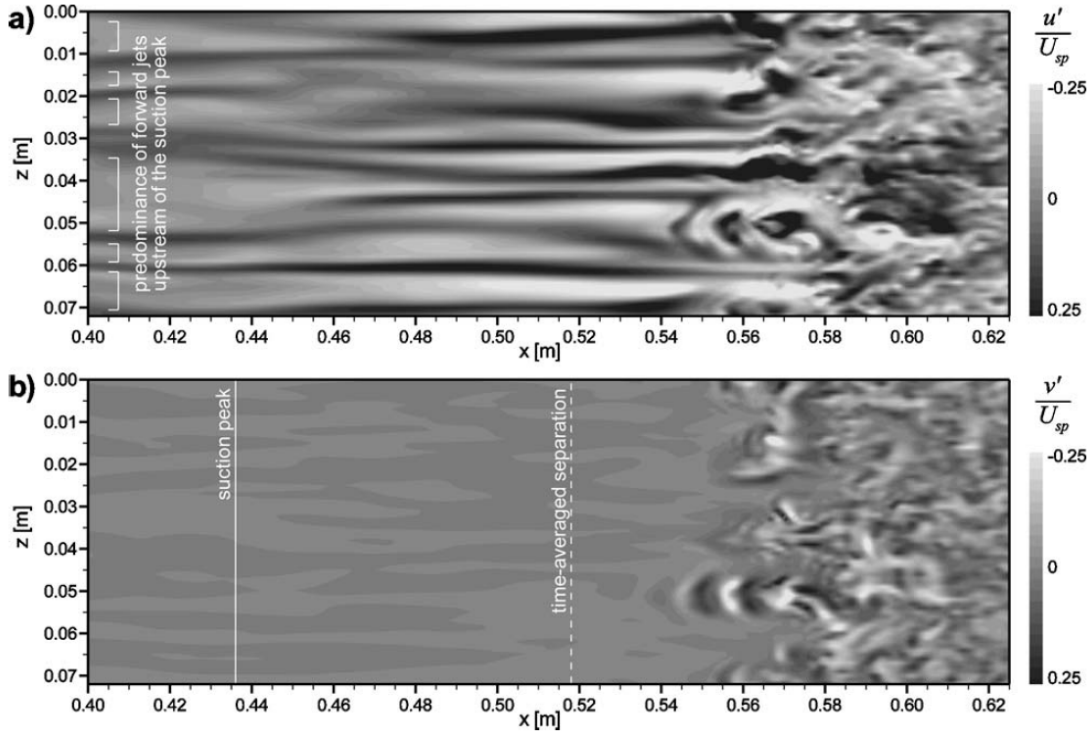

Figure 1-11 Longitudinal streaks in a separating flow at high free-stream turbulence levels, at a wall normal plane of half the free-stream velocity. (a) stream-wise fluctuations. (b) wall-normal fluctuations. (McAuliffe and Yaras, 2010).

It is seen that while multiple interpretations of the exact physical mechanism of turbulent spot formation and breakdown in the final stages of bypass transition exist, there is agreement that the disturbance frequencies leading to breakdown correspond closely with the KH frequency of the separated shear layer. As a result, the Kelvin-Helmholtz instability can be considered to be a mechanism of central importance for transition to turbulence in separated shear layers (Diwan and Ramesh, 2009; Simoni et al., 2012).

Interaction with upstream wakes

The flow field in a low pressure turbine passage experiences high periodic unsteadiness. The unsteadiness is primarily due to wakes from upstream stages that are convected through the engine. Potential interaction from upstream and downstream stages may also contribute to unsteadiness.

Upstream wakes passing through an LPT passage experience bowing, reorientation, and elongation (Hodson and Howell, 2005), and persist through many blade-rows. Relative to the time-mean velocity field, the wake has been considered to be a "negative jet" that has been superimposed on the free-stream (Meyer, 1958). It causes impingement of the jet on the suction surface, producing acceleration of the flow downstream and deceleration of the flow upstream of the passing wake. These features are shown in Figure 1-12.

Passing wakes behave like packets of high levels of turbulence that can cause early transition. Transition due to wakes is known to be bypass transition (Zhong et al., 1998). Mandal and Dey (2011) experimentally studied the interaction of a flat plate boundary layer under low (0.1%) free-stream turbulence conditions with the wakes shed by a stationary upstream circular cylinder. The cylinder was located one cylinder diameter upstream and 3-4 cylinder diameters above the leading edge of the flat plate in the wall-normal direction, and oriented parallel to it. The wakes shed behind the cylinder appeared

in the early flow field as two-dimensional, span-wise vortices, which then evolved into Λ structures. Staggered patterns of these Λ structures were identified, which corresponded to sub-harmonics of the wake-shedding frequency, analogous to the H-type natural transition process described previously. Finally, in the late stages of the transition process, they identified the formation of stream-wise streaks, and sinuous secondary instability oscillations of these streaks following the growth of streak amplitude to about 35% of free-stream velocity. Despite the low free-stream turbulence conditions, wake induced transition showed these features of bypass transition in the late stages.

Because of their propensity for triggering transition, passing wakes are known to reduce separation losses, especially at lower Reynolds numbers (Figure 1-13). At high Reynolds numbers, when the flow is likely to experience little or no separation, passing wakes may even result in higher overall losses (Stadtmüller, 2000). If separation of the laminar flow does occur, passing wakes may induce transition in the separated shear layer. If the wake passing frequency is low, the flow can show an unsteady pattern that involves separation and re-attachment, with intermittent transition. Depending on the pressure profile, flow Reynolds number, and turbulence intensity, the sequence of events in time and their location in space can vary.

While higher free-stream turbulence levels lead to early transition and re-attachment, the longer resulting turbulent flow region may offset the loss recovery. As with the effect of passing wakes on overall component loss, this depends upon the flow Reynolds number (Volino, 2002). As a result, a "controlled diffusion blading" design has been suggested (Hourmouziadis, 1989), where the airfoil is designed to permit a small separation bubble in preference to a long turbulent zone.

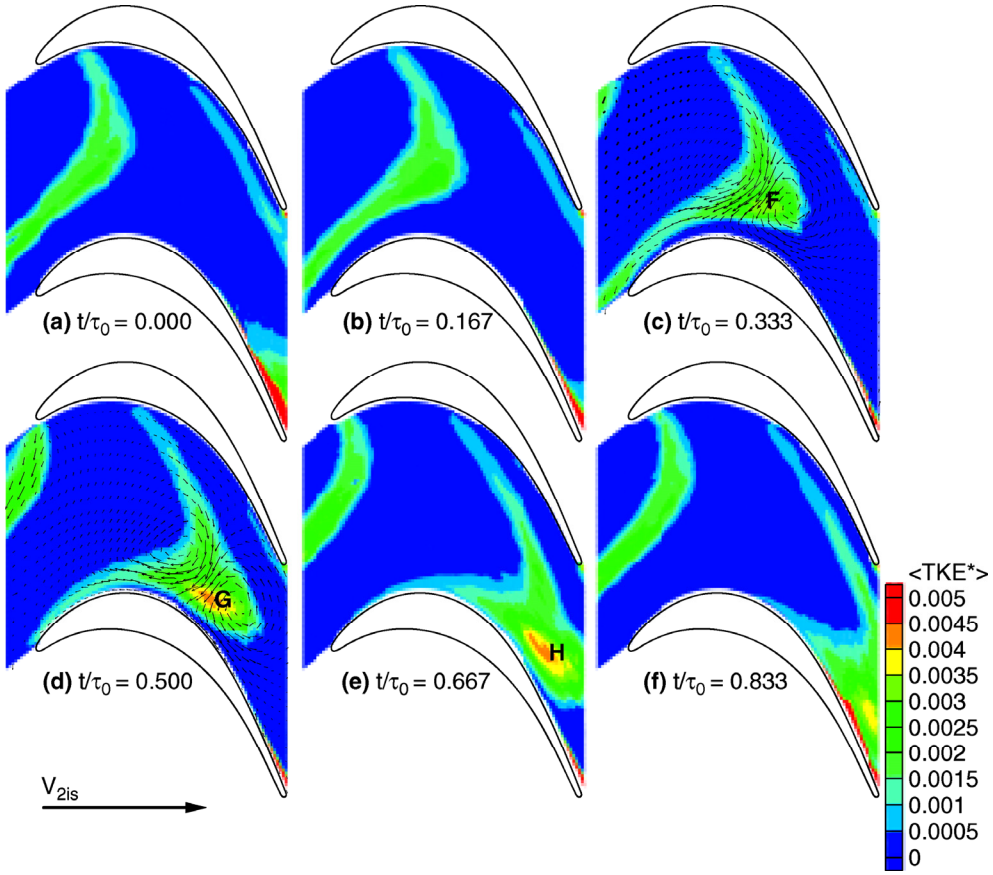

Figure 1-12 Passage of wakes, showing distortion of the turbulent kinetic energy field. Velocity vectors illustrate a "negative jet" effect (Stieger and Hodson, 2004)

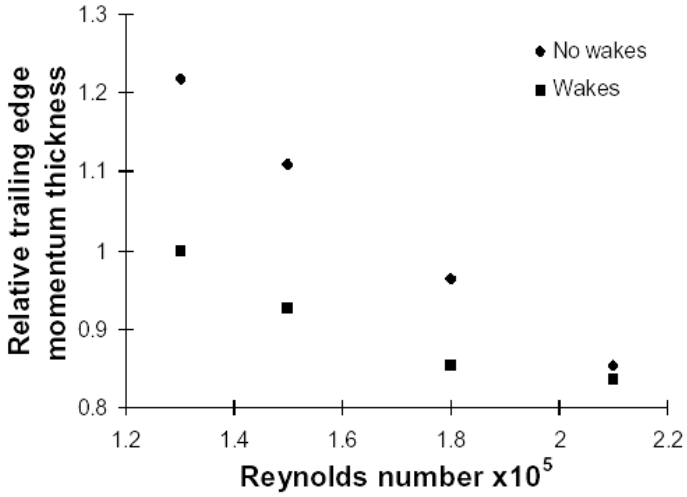

Figure 1-13 Suction surface boundary layer loss vs. Reynolds number (Howell et al., 2000)

Solomon (2000) studied wake-induced transition on several blade and turbulence level configurations in a rotating turbine rig. Kaszeta et al. (2001) studied the effects of passing wakes on transition and separation on a low pressure turbine airfoil suction surface. Wakes were found to affect the flow due to their differences relative to the free-stream turbulence levels, scales, and velocity (deficit), which produced changes in angle of attack and temporal pressure gradients. It was proposed that the passing wakes imposed pressure fluctuations on the near-wall viscous layer of the airfoil suction surface. Yaras (2001) measured the effects of changes in pressure gradient on separated flow transition at low free-stream turbulence. Schobeiri et al. (2003) used a rotating cascade of rods to produce an unsteady flow field over a concave-curvature plate, and studied the effects of mixing and impinging of the passing wakes using conventional and wavelet-based methods.

The recent Large Eddy Simulation study of Rao et al. (2013) showed that the small-scale turbulence in wakes intensify the stream-wise streaks that are formed due to high levels of free-stream turbulence. These strong streaks induce large span-wise variations in the span-wise KH vortices of a separated shear layer, inducing much earlier transition than the high FST alone. The streaks are found to originate at the leading edge.

The results of Rao at al. (2013) show many features of the experimental study of Coull and Hodson (2011). The latter clarified that the initial generation of the coherent span-wise vortices in the separated shear layer by the passing wake was due to the interaction of the wake disturbances in the free-stream with the inherent KH instabilities of the flow. This KH inception process was not affected by the wake-amplified patches of streaks in the upstream boundary layer, which lagged behind the wake disturbance in the free-stream. The subsequent process of breakdown to turbulence was strongly driven by the arrival of the wake-amplified streaks, producing short-span KH structures. The authors mentioned that it was unclear whether the wake-induced generation of the KH structures was due to their associated large-scale velocity fluctuations, or small-scale turbulence.

They graphically summarized the transition scenario in the unsteady separation flow field with high free-stream turbulence and passing wakes with the space-time diagram of Figure 1-14.

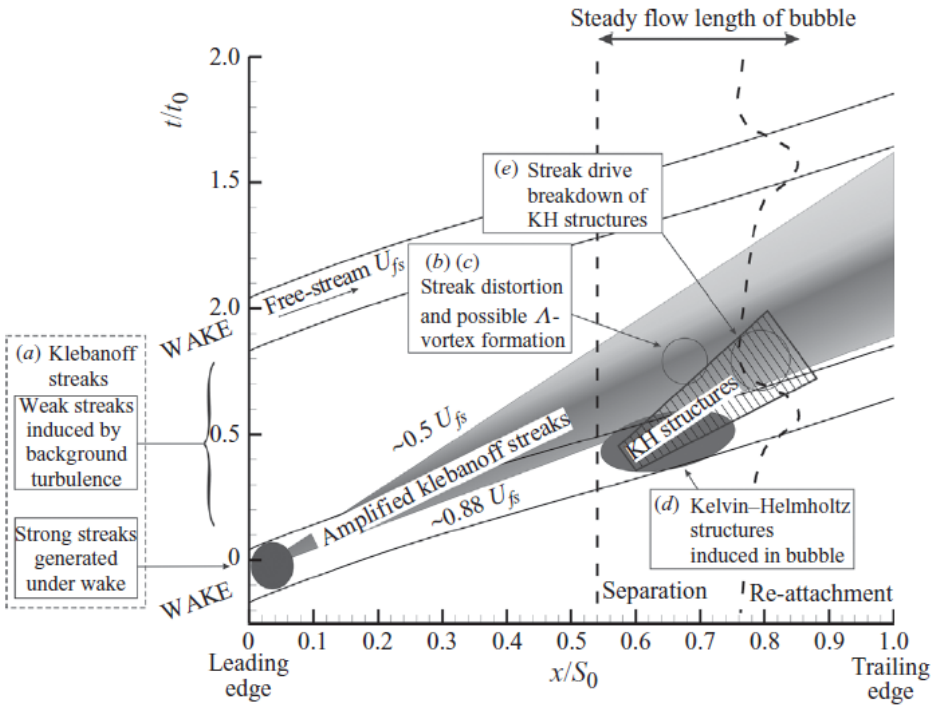

Figure 1-14 Space-time diagram of unsteady separation and wake-induced transition in a high free-stream turbulence (Coull and Hodson, 2011).

Wakes are immediately followed by so-called "calmed regions," which are zones that resemble thin, laminar boundary layers. They have also been observed to follow turbulent spots in transitional boundary layers (Gostelow et al., 1997). They show full velocity profiles and laminar-like wall shear stress values, and exhibit high levels of resistance to separation well after the turbulence associated with the wake has passed. In a case of unsteady separation and separated-flow re-attachment, they are the intermediate relaxation stage between the transitioned, re-attached flow, and the growing laminar boundary layer that becomes unstable and separates again.

Separation control

Separation control strategies in LPTs can be considered to be passive or active. Passive control devices, such as dimples (Bearman and Harvey, 1993) and fixed turbulators (Lin et al., 1994), have been a traditional approach to re-energizing the flow by triggering transition and inducing re-attachment, but create parasitic drag at take-off and high Reynolds number conditions, when they are not required. Active control devices are those that can be employed only when needed.

Passive flow control

Design of passive flow control devices involves a trade-off between effectiveness in triggering transition and drag. Volino (2003) found that the height and location of the backward-facing step aft of the passive element were important geometric characteristics, with stream-wise extent and leading edge location being relatively unimportant. Based on this, a small bar was selected as the shape of the passive device. It was concluded that passive devices that perturb the flow sufficiently for the disturbance to grow in space over a finite downstream distance to transition the flow to turbulence are more efficient than devices that cause immediate transition. The bar size for immediate transition was found to be in agreement with the correlation $Re_d = U_d d/\nu > 600$ (Gibbings, 1959), where d is the bar thickness, and U_d is the velocity of the untripped boundary layer at a wall-normal distance equal to d. The more efficient bar was smaller than this, depending on the Reynolds number and free-stream turbulence intensity. Experimental evidence from multiple researchers (e.g., Zhang and Hodson, 2004; Bohl and Volino, 2006) suggests that three-dimensionality in passive devices for controlling separation will not necessarily produce any benefits over the two-dimensional form.

Active flow control

In the context of active flow control, vortex generating jets (VGJs) and plasma actuators are prominent subjects of recent research. Active control mechanisms may lend themselves to separation control by one of two modes: a) adding near-wall momentum

and stabilizing the flow as it encounters the adverse pressure gradient, thereby delaying or preventing separation, or b) introducing disturbances that exploit natural instabilities of the flow, and undergo rapid growth.

Vortex Generating Jets (VGJs)

VGJs involve the injection of fluid through holes in the wall. The geometry of the holes is characterized by a skew angle with the free-stream flow direction, and a pitch angle with the wall (Figure 1-15). VGJs that are effective for flow control typically have shallow pitch angles (30° - 45°) and large skew angles (45° - 90°) (Volino et al., 2011).

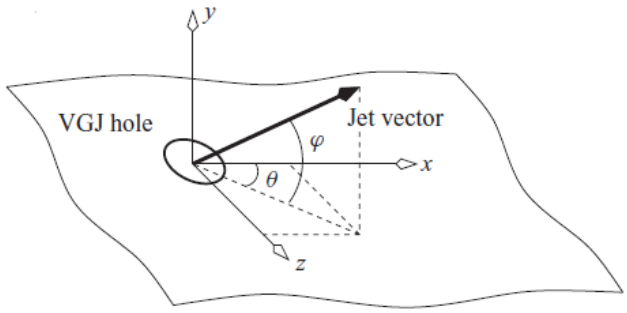

Figure 1-15 Schematic of VGJ injection geometry. θ is the skew angle relative to the direction of the free-stream flow; φ is the pitch angle relative to the plane of the wall. (Postl et al., 2011)

In steady (i.e., non-pulsed) operation of VGJs, separation control involves injection of jets from the wall into the flow to embed stream-wise vortices into the shear layer. Stream-wise vorticity is known to be very effective for triggering transition (Johnson, 2004). Using dye visualization in a water channel flow, Zhang and Zhong (2010) studied the interaction of a span-wise array of circular synthetic jets with a separating boundary layer to characterize these stream-wise vortical structures. Depending on the jet-to-free-stream velocity ratio, these vortical structures resembled hairpin vortices or tilted vortex rings. The legs of these structures were found to induce streaks of high stream-wise velocity that effectively transported momentum across the shear layer (Figure 1-16). The vortical structures generated were found to have convection velocities varying between

50% and 96% of the free-stream velocity. The authors conjectured that a major requirement for effective flow control is the introduction or generation of coherent structures into the boundary layer that enhances transport of high-momentum fluid from near the free-stream. They observed that since the physics of flow control is not well understood, the operating conditions for most flow control experiments are set by trial-and-error. They concluded that optimal conditions of velocity ratio and pulsing frequency may depend on the interaction between vortical structures generated by adjacent jets.

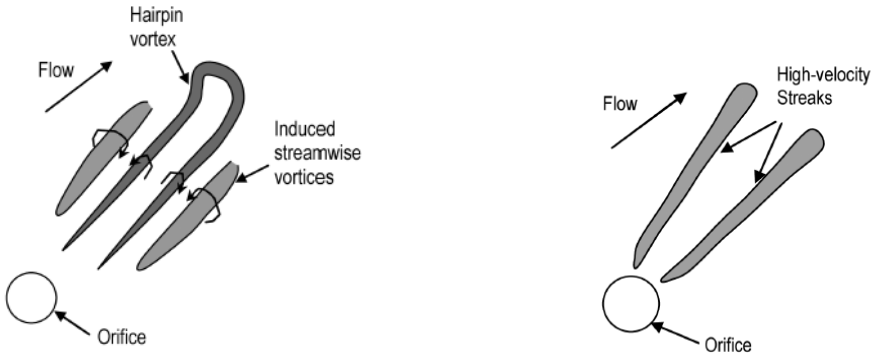

Figure 1-16 Hairpin vortex and the induced stream-wise vortices from a single synthetic jet (left); high speed stream-wise streaks produced by the downwash of the vortices (right). (Zhang and Zhong, 2010)

Plasma Actuators

The application of a dielectric barrier discharge (DBD) plasma for flow control was demonstrated by Roth et al. (1998), and has been developed over the last decade via computational, experimental, and theoretical research approaches spanning from fundamental studies of the discharge to a wide range of applications (e.g., Hultgren and Ashpis, 2003; Enloe et al., 2004; Opaits et al., 2005; Corke et al., 2007; Little et al., 2010). Several novel configurations and applications for plasma actuators have been developed (see, for example, the review paper of Wang et al., 2013). The actuator configuration relevant to this study is the conventional span-wise oriented DBD plasma actuator.

Plasma actuators: construction and plasma discharge

A Dielectric Barrier Discharge (DBD) actuator comprises an arrangement of two electrodes separated by a dielectric (insulator) that encapsulates one of them, with the other electrode exposed to the surrounding air. When a large, high frequency (~kV, ~kHz) time-varying voltage is applied between the electrodes, the surrounding fluid is weakly ionized, producing a plasma discharge. The discharge produces a faint bluish-purple emission, which is visible in a dark room or in long-exposure photographs. Figure 1-17 illustrates the configuration, and shows the visible appearance of the discharge.

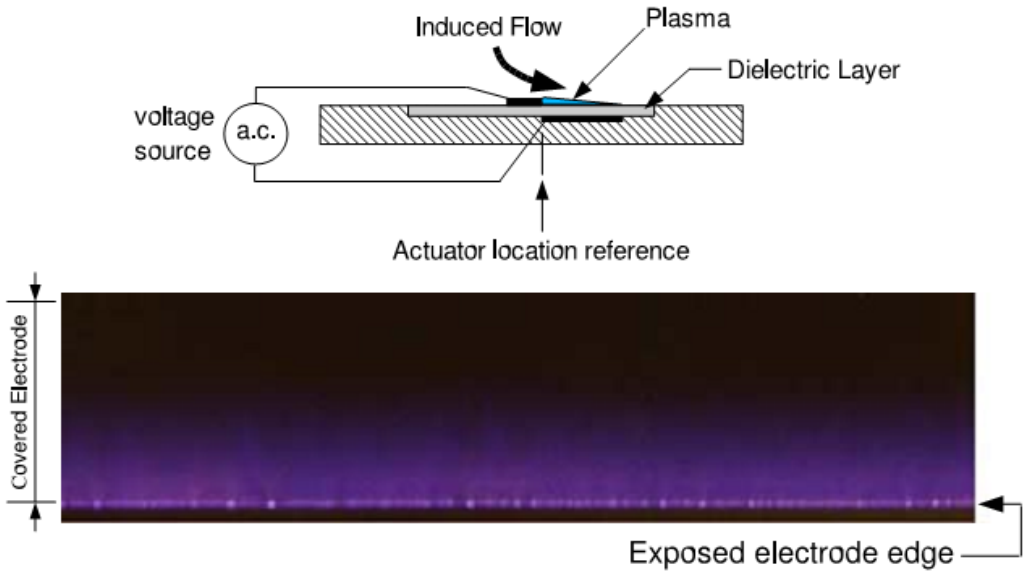

Figure 1-17 Schematic of Dielectric Barrier Discharge (DBD) plasma actuator (top); a top-view photograph of the plasma operating at 1 atmospheric pressure (Corke et al., 2009)

By carefully controlling the actuator material, geometry and the driving voltage characteristics, an active flow control methodology thus exists which draws relatively little power (on the order of W/m to tens of W/m of electrode or discharge length (Poon, 2011)), and does not suffer the usual drawbacks of added weight, mechanical vibration, complexity, poor dynamic response and parasitic drag loss associated with passive control solutions. When operated in quiescent air, such an actuator generates a wall-jet with a peak velocity of a few m/s, a few millimeters away from the wall (Figure 1-18).

This effect of the plasma on a surrounding fluid is a result of collisional momentum transfer from ions and electrons on the neutral fluid molecules, and is not a thermal effect for typical kV/kHz-range AC DBD discharges (Orlov, 2006; Iqbal et al., 2007).

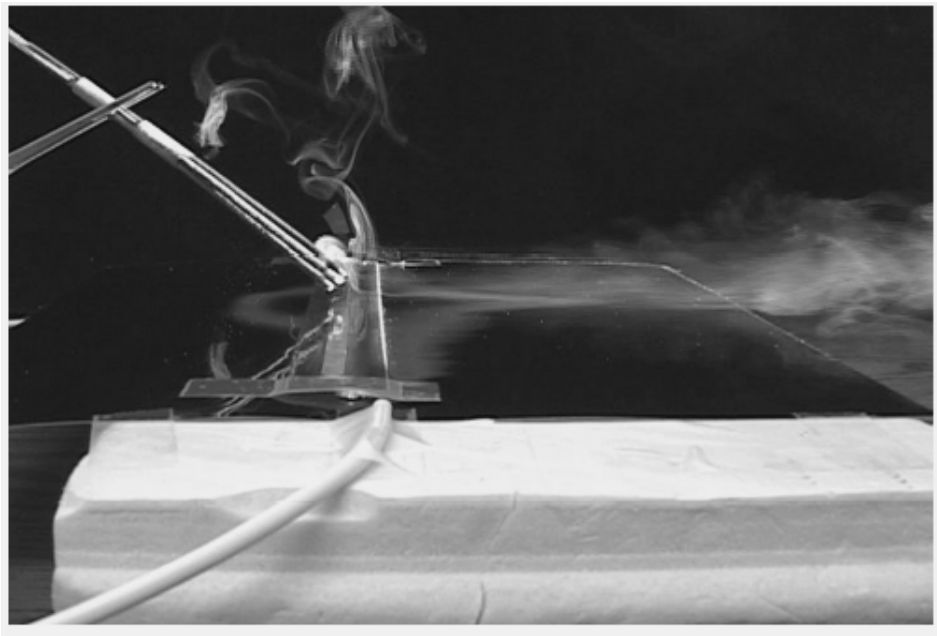

Figure 1-18 Operation of actuator in quiescent air, showing coupling of momentum and a resultant near-wall jet by smoke visualization (Enloe et al., 2004)

The plasma is stable at normal atmospheric conditions and has a self-limiting nature, i.e. it quenches itself at any constant applied voltage and requires a time-varying voltage to sustain a discharge. Although this DBD plasma appears to be glowing as a uniform and diffuse plasma, it has considerable temporal and spatial structure. It is characterized by fine micro-filaments attributed to electron avalanches. The diameters of these micro-filaments are on the order of tens to hundreds of nanometers (Roth and Dai, 2006). As the applied signal amplitude is increased, a "saturation" condition (Thomas et al., 2009) is eventually reached, which is characterized by the formation of coarse, bright streamers. These streamers are typically visible to the naked eye, with diameters on the order of tenths of millimeters. (Confusingly, the terms "filaments" and "streamers" are often used interchangeably in the literature.)

Increasing the amplitude of the applied signal beyond saturation leads to rising dissipation of electrical power without significant increase in flow control authority.

The net positive (stream-wise) force generated by a plasma actuator is considered to be a result of the asymmetry of the discharge in the positive and negative half-cycles of excitation, but no clear consensus exists on the physical mechanism. Various experimental and numerical studies have arrived at contradictory conclusions on whether the force vectors produced in the two half-cycles of excitation are aligned ("PUSH-push") or opposed ("PUSH-pull") in orientation.

A computational study with air chemistry (Font et al., 2007) indicated that the force generated in the backward discharge, i.e., when the exposed electrode is at positive electrical potential, is at least an order of magnitude higher than that produced during the forward discharge, and that the forces are oppositely directed. It also predicted higher plasma density on the backward discharge.

Several experimental studies also indicate a difference between the force generated during the two discharge half-cycles. One study (Baird et al., 2005) suggested that the forces are oriented in the same direction, but a later one (Porter et al., 2006), using Fast Fourier Transform (FFT) analyses of temporal measurements of actuator force acquired by an accelerometer, supported the conclusion that the forces are oppositely directed, and differ by about an order of magnitude. Another study (Enloe et al., 2008) indicated that the asymmetry is even stronger than previously believed. Using an actuator as a part of a pendulum system, the authors concluded that the stronger discharge accounts for nearly all (~97%) of the momentum coupling. In contrast to the previous results from computations, though, the forward discharge, i.e., when the exposed electrode is negative, is considered to be the source of this dominant thrust. Another paper (Kim et al., 2007) is in qualitative agreement with this latter conclusion. A review paper by Corke et al. (2010)

concluded that “it seems well established that both half-cycles of the discharge add momentum to the flow in the same direction.” However, subsequent papers such as Debien et al. (2012) and Neumann et al. (2013) continue to find evidence for the PUSH-pull configuration. It would appear that the matter is still undecided.

The force production and asymmetry characteristics are known to be dependent on the chemistry of the surrounding fluid, showing strong sensitivity to oxygen content in the air (Kim et al., 2007). The force production has been shown to decrease with decreasing pressure (Gregory et al., 2007). It has also been suggested that lower humidity levels can produce larger current density and thrust (Leger et al., 2002).

Short nano-second pulses at high repetition rates are also a notable subject of research. Thermal effects have been shown to be the primary mode of effectiveness for these nano-second pulsed plasma actuators. Roupassov et al., (2009) used a plasma actuator excited by periodic nano-second pulses for separation control, and found that thermal effects of actuator operation were significant for these short, high-frequency pulsed actuators. The gas temperature of the plasma layer reached 400 K for a 50 ns pulse duration case. Little et al. (2010) performed a similar study of airfoil leading edge separation control using nano-second pulses, and also concluded that most of the efficacy of the device was due to thermal compression waves, rather than collisional momentum coupling between charged and neutral species.

Flow features of plasma actuator operation

In continuous operation, a conventional span-wise oriented DBD plasma actuator generates a wall-jet-like shear layer. This wall jet is nominally similar to a Glauert profile (Glauert, 1956); at high voltage amplitudes, it begins to deviate from that profile (Murphy et al., 2013). At the instant of initial activation, the impulsively started shear layer entrains surrounding fluid and rolls up, producing a starting vortex. In pulsed operation, a train of such starting vortices may be generated under suitable conditions. As

has been noted, pulsed operation is generally found to be more effective than steady operation, and has been used in the present study. A review of the recent literature on the starting vortex is relevant here as it will be significant in developing a physical picture of the flow field in Chapter 7 for different conditions of pulsing parameters.

Entrainment of surrounding fluid at the initiation of the wall-jet-like flow induced by the plasma actuator produces a starting vortex. Images from a smoke-visualization study by Whalley and Choi (2010) shows the formation of this starting vortex as it rolls up and grows along its path in the stream-wise direction (Figure 1-19).

Noting similarities of the starting vortex to a junction vortex (which is formed when an impulsively started moving wall slides under a fixed wall), Whalley and Choi (2012) continued their study of a non-pulsed DBD actuator in quiescent air to investigate scaling parameters. They used PIV measurements and smoke-visualization to study three combinations of plasma excitation (amplitude and frequency) parameters, and found that once a steady-state of the actuator induced flow velocity was reached, the starting vortex became self-similar. An important feature noted is the generation of secondary vorticity due to the presence of the wall. This secondary vorticity is ingested into the vortex, and contributes to the motion of the vortex away from the wall.

A PIV-based study of starting vortex characteristics by Sattari et al. (2012) was conducted near the sharpened trailing edge of a plate, so that the starting vortex was not bound by the presence of the wall after formation, thereby lacking a source of secondary vorticity. In contrast to Whalley and Choi (2012), they found that both induced circulation and the length scale of the vortex to evolve as $t^{1/2}$ (Whalley and Choi: $t^{1/3}$ and $t^{2/3}$, respectively). The stream-wise convection velocity of the vortex was found to be approximately 12% of the maximum velocity of the plasma-induced wall jet.

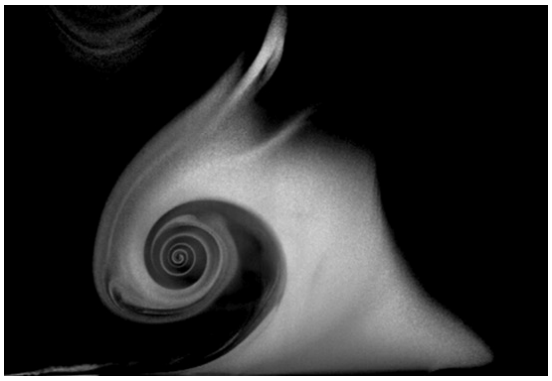

Figure 1-19 Flow visualization showing starting vortex 120 ms after plasma initiation (Whalley and Choi, 2010)

Growth limit for the starting vortex

A formation number characterizing the limit of growth of a starting vortex is usually related to a relevant geometric length scale, such as cylinder or nozzle diameter, or airfoil chord length. Sattari et al. (2012) conjectured that the relevant length scale for the plasma-induced starting vortex (not bounded by a downstream wall, in their case) is the distance S between the vortex core and the edge of the plasma-induced shear layer that feeds the vortex. They obtained a critical dimensionless number marking the limit of growth of the starting vortex for their experiment: $\Gamma^* \approx 1.5$, where $\Gamma^* = \Gamma/(u_{max}.S)$, Γ is the circulation of the vortex, and u_{max} is the maximum velocity of the plasma-induced shear layer. The plasma-induced shear layer flow has an inertial tendency to continue stream-wise, as well as a competing velocity component that is induced by the vortex (according to the Biot-Savart law) that diverts it from the stream-wise direction. In the present configuration, Sattari et al. (2012) noted that as the vortex evolves, the distance S between the shear layer and the vortex core grows at a greater rate than the circulation Γ. As a result, the shear layer eventually flattens, and the starting vortex separates from it. This is the limit of growth for the starting vortex.

The critical number $\Gamma^* \approx 1.5$, however, is not universal to all starting vortices, and depends strongly on the global flow field. Additionally, if the starting vortex flow is turbulent (Re > 1500, based on shear layer velocity and mean vortex diameter (Sattari et

al., 2012)), the shear-layer instabilities are amplified, and early separation of the starting vortex from the feeding shear layer is likely. Whalley and Choi (2010) observed that when the plasma forcing was strongly increased, Kelvin-Helmholtz instability waves appeared in the shear layer of the plasma induced shear layer, which were wrapped into the starting vortex.

It can be expected that the pulsed actuator of the present study that operates in the non-quiescent flow field in an airfoil geometry may show qualitatively similar physical characteristics, with an unknown critical value for growth limit.

Time scales for starting vortex initiation and growth

Sattari et al. (2012) noted that "(the) start-up phase of the plasma actuator is one order of magnitude faster (less than 3 ms) than the time scale associated with the growth of the vortex (~20 ms to reach maximum growth)."

In this case, "maximum growth" relates to their empirical observation that both vortex radius and vortex circulation asymptotically plateau about 20 ms after plasma activation, in a process that is described in the preceding section. The meaning of the term "start-up phase" is not clarified by the authors. Similar observations from other studies suggest that "start-up phase" may imply the first appearance of a discernible vortex core after starting the plasma actuator.

Kotsonis and Ghaemi (2012) conducted experiments and computations of a plasma actuator induced flow in quiescent air, with and without pulsing. The body force distribution used by the flow solver for their computation was derived from the corresponding experimental results. As Figure 1-20 shows, the induced horizontal velocity rapidly (within ~2 ms of starting) ramps up to a near constant value in the near vicinity of the actuator. (Since the starting vortex continues to convect downstream,

attaining a constant velocity at a fixed location near the actuator does not imply that the starting vortex stopped growing after 2 ms of actuator activation.)

Based on this figure, the high velocity front associated with the vortex appears to convect horizontally at about 1 m/s, which is one-half of the maximum velocity.

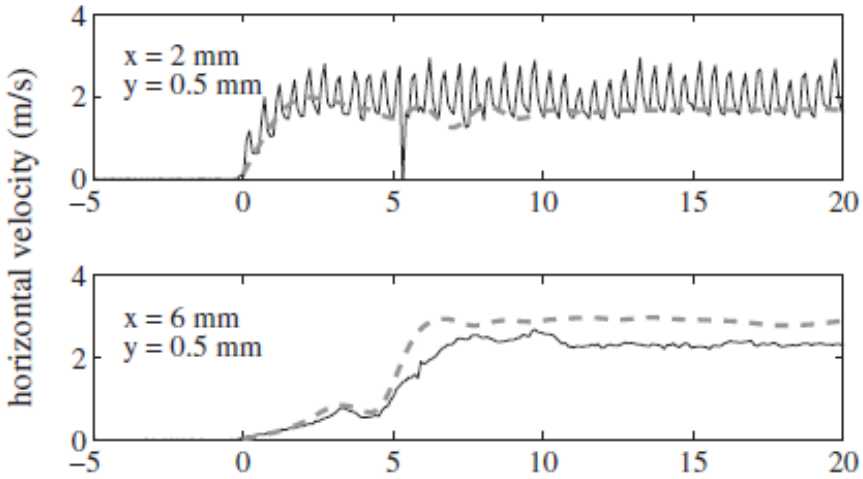

Figure 1-20 Evolution of horizontal velocity at two spatial locations near the actuator after starting the actuator. The downstream edge of the exposed electrode is at the origin. Experiment: solid line. Computation: dashed line. (Kotsonis and Ghaemi, 2012)

In their study of the starting vortex produced by a non-pulsed plasma actuator in quiescent air, Whalley and Choi (2012) found a similar transient of maximum induced velocity before it reached a steady-state. They characterized the velocity scale of the starting vortex by U_0, which is the maximum steady-state velocity induced by the plasma actuator. Figure 1-21 shows two experimental cases, with $U_{0,(a)}$ = 0.45 m/s, and $U_{0,(b)}$ = 1.19 m/s. The transient at the beginning is clearly visible. A small over-shoot was observed for cases with lower values of U_0, such as case (a). Non-dimensional time $t^* = t.U_0^2/\nu$. The decay of velocity at the end occurs when the actuator is switched off (600 ms run-time for case (a); 300 ms for case (b)). Using the given definition of t*, it can be estimated from the figures that cases (a) and (b) reach steady state in dimensional time t of about 60 ms (case b) to 80 ms (case a), depending on how the overshoot is interpreted.

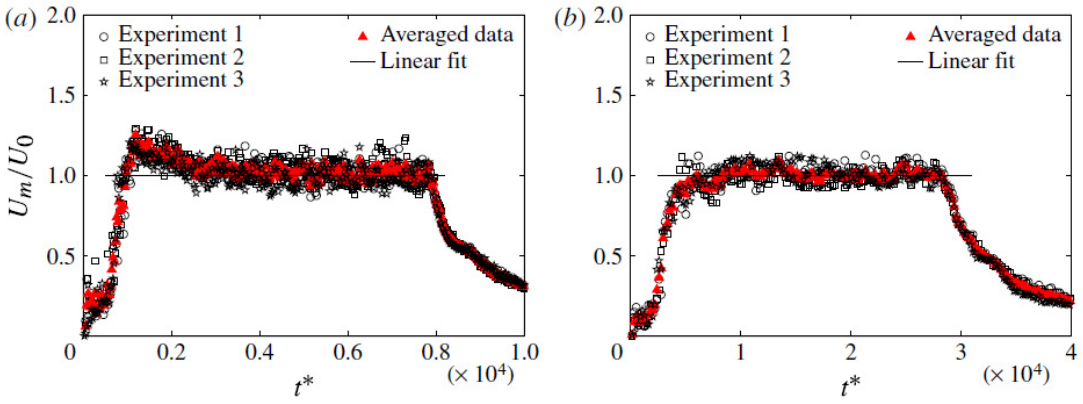

Figure 1-21 Maximum velocity induced by the actuator (U_m) versus time, for two experimental cases. U_0 is the steady-state value of U_m for each case, and $t^* = t.U_0^2/v$. (Whalley and Choi, 2012).

Benard and Moreau (2011) also found a timescale of about 30 ms for the formation and growth of a starting vortex.

Citing the literature of plasma discharge in nitrogen gas and atmospheric air, Whalley and Choi (2012) noted that the time required for the transient current density of the plasma actuator to reach a steady state increases with smaller applied voltages to the actuator. The plasma excitation voltages used in the Whalley and Choi (2012) experiments are indeed noticeably lower than those of Sattari et al., 2012, although this does not necessarily indicate a causal relationship.

Table 1-1 summarizes the condition of applied voltage and excitation frequency from the literature, along with the relevant time-scales for initiation and growth of the starting vortex in quiescent air.

Table 1-1 Conditions of applied voltage and excitation frequency from the literature, with corresponding timescales for initiation and maximum growth of a starting vortex in quiescent air

	Applied voltage	Excitation frequency
Sattari et al., 2012 (start-up: ~ 3 ms; max. growth of starting vortex: ~ 20 ms)		
Case A	12.27 kV	11 kHz
Case D	16.24 kV	11 kHz
Kotsonis and Ghaemi, 2012 (start-up: ~ 2 ms; starting vortex not tracked)		
Case discussed	12 kV	2 kHz
Benard and Moreau, 2011 (start-up: a few ms; max. growth of starting vortex: ~ 30 ms)		
Case discussed	18 kV	1 kHz
Whalley and Choi, 2012 (time for max. velocity: 60 ms (case b) to 80 ms (case a))		
Case a	5.5 kV	20 kHz
Case b	7.2 kV	20 kHz

Apart from the measurements taken with the plasma actuator continuously on, as discussed above, Kotsonis and Ghaemi (2012) also took PIV measurements with the actuator in pulsed operation. At a fixed applied voltage of 10 kV_{p-p} and fixed excitation frequency of 2 kHz, three pulse frequencies (50, 200, 300 Hz) were tested at a fixed duty cycle of 50%. Additionally, they also fixed the pulse frequency at 50 Hz, and tested three duty cycles (25%, 50%, 75%). For the 50 Hz pulsing, a train of discrete starting vortices corresponding to the number of pulses was observed. However, for the higher pulse frequencies of 200 and 300 Hz, the time scale of pulsing was too high for the first starting vortex to depart the vicinity of the actuator and restore the initial conditions. As a result, the rapidly pulsing actuator fed momentum into the first and only starting vortex formed, resulting in a flow field that qualitatively resembled the continuously-on case.

From the results of Kotsonis and Ghaemi (2012), the following estimations may be made: nominal starting vortex diameter ~ 2 mm, and maximum induced velocity speed ~ 2 m/s. Sattari et al. (2012) calculated that the core of the starting vortex in quiescent air convects at about 12% of the maximum induced shear layer velocity. For the Kotsonis

and Ghaemi (2012) study, this corresponds to a vortex convection speed of ~ 0.2 m/s. This implies a critical minimum off time during pulsing of ~10 ms for non-overlapping vortices. This agrees well with their observations of no discrete vortices at pulsing frequencies higher than the 50 Hz (at 50% duty cycle) case (which corresponds to an off-time of 10 ms).

Relevant conclusions about starting vortices

Based on the state of the art, it can be concluded that for continuous actuator operation in quiescent air, starting vortex formation occurs within a few (2-3) ms of starting the plasma actuator. If the actuator continues to operate and feed it, the starting vortex continues to grow for another order of magnitude in time, as it convects downstream. When the starting vortex has grown so that its core is critically far from the feeding shear layer, the vortex separates from the layer.

When the actuator is operated in pulsed mode, a critical "rest" or "off" pulsing timescale exists that permits the formation of a train of discrete starting vortices. For operation in quiescent air, this critical pulsing timescale appears to be comparable to, or somewhat greater than, the timescale of maximum growth of an individual starting vortex (about 20 to 30 ms in the majority of cases discussed). However, for actuator operation in the boundary layer of an externally-imposed flow, the convection speed of starting vortices would scale with the free-stream velocity, leading to a reduced critical pulsing timescale. Sattari et al. (2012) indicate that the maximum growth timescale is also likely to strongly vary with a changing global flow field.

Flow control studies using Vortex Generating Jets (VGJs) and plasma actuators in pulsed mode

Several researchers (Volino et al., 2009 and 2011; Olson et al., 2005; Bons et al., 2005; Sondergaard et al., 2002) have studied the use of VGJs for separation control in low pressure turbines, with varying blowing ratios and free-stream turbulence intensities.

It was found that a minimum blowing ratio (blowing ratio = $(\rho u)_{jet}/(\rho u)_{local}$) exists, which is a function of the location of jet injection. Low blowing ratios provided better control than higher ones, owing to penetration of the higher blowing ratio jets into the free-stream, with subsequent rapid dissipation. A decrease in effectiveness of the VGJs was also found at high free-stream turbulence levels. This was also attributed (Olson et al., 2005) to dissipation of the generated vortices in the turbulent boundary layer that resulted from rapid transition.

Volino (2003) studied the use of pulsed VGJs for separation control in a low Reynolds number, low free-stream turbulence intensity flow over a low pressure turbine airfoil. He found that each pulse from the jet had leading- and trailing-edge velocities (relative to the free-stream) similar to those found in a turbulent spot. The presence of a calmed region was noted. Volino et al. (2009, 2011) found pulsed VGJs more effective than steady ones. Lower pulsing frequencies were found to require higher jet velocities for effective control, while higher frequencies produced effective control even with low velocities and duty cycles.

Huang et al. (2003) used static pressure measurements to observe the extent of separation in a low pressure turbine geometry, and the control provided by a plasma actuator. It was noted in this paper that it is possible to use a single plasma actuator in "unsteady mode", i.e., switch it on and off with a small duty cycle and a switching frequency low enough for the fluid to respond to it. This would cut down the power consumption whilst amplifying the re-attachment effect.

Post and Corke (2003) realized the potential of plasma actuators in leading-edge separation control for high angle-of-attack applications by installing an actuator at the leading edge ($x/c = 0$). An additional actuator was added at $x/c = 0.5$, with the induced velocities directed as illustrated by Figure 1-22. The actuators were tested at angle-of-attack $\alpha = 16°$, which is 4° past the natural stall angle of the airfoil, at Reynolds numbers

70,000 and 158,000. In both cases, the flow was found to be fully attached with the actuators on. Figure 1-22 also shows smoke visualization of the resulting flow fields.

Some researchers (Corke and Matlis, 2000; Hultgren and Ashpis, 2003) have used phased arrays of actuators to produce a spatial traveling-wave effect, and studied the effectiveness of this device for flow control. When compared to operation without the traveling-wave effect, the latter paper concluded that most of the control authority of the array was due to the most downstream actuator in the array alone.

Several researchers (Sosa et al., 2007; Patel et al., 2008; Greenblatt et al., 2008; Little et al., 2009) have by experimental verification found that tuning the forcing frequency to match the natural shedding frequency of the shear layer in question is optimal. Others (Asada et al., 2009) find higher non-dimensional forcing frequencies to improve stall control on a NACA-0015 airfoil, with smaller duty cycles out-performing higher ones. Little et al. (2009) used a pair of DBD actuators on either side of a high-lift airfoil flap's shoulder to study control of separation from the deflected flap at two Reynolds numbers. They found that the actuator was most effective when it was operated in an unsteady manner at the natural oscillation frequency of shedding for the trailing edge flow, enhancing this mechanism. The relative phase of operation of the two actuators was found to be important, being a function of the distance between them and the excitation frequency.

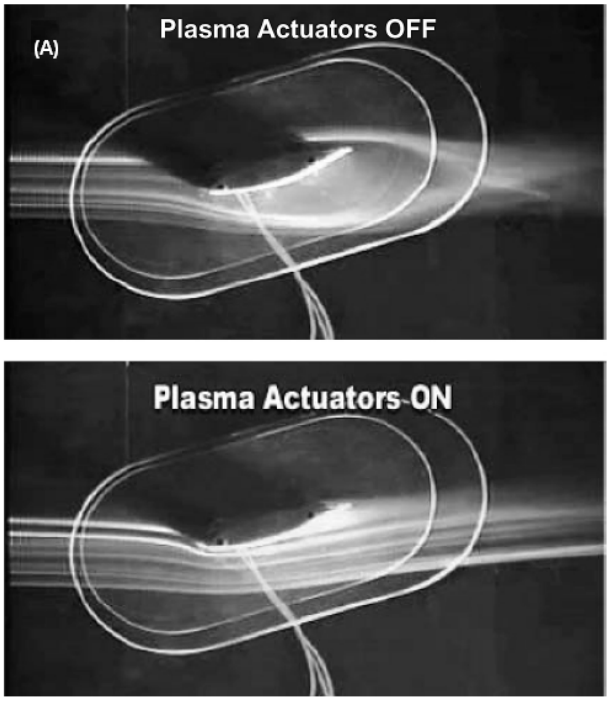

Photographs of visualized flow around the airfoil with plasma actuator off (top) and on (bottom) for $\alpha = 16$ deg and $Re_c = 158 \times 10^5$.

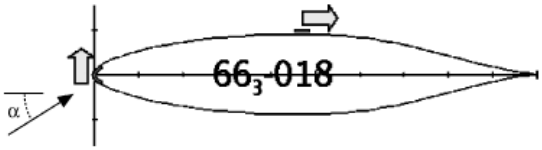

Schematic drawing showing the locations and orientations of plasma actuators used for separation control.

Figure 1-22 Effective leading-edge separation control at high angle-of-attack demonstrated using smoke visualization (above); the location and orientation of the two plasma actuators used for this study (below) (Post and Corke, 2003)

Corke et al. (2004) introduced results from the pulsed-mode operation that was mentioned as a possibility in Huang et al. (2003), as noted before. In this case, a 10% duty-cycle was found to be sufficient for effective operation, exceeding the performance of the steady (or "always-on") actuator over a larger range of angles-of-attack, while consuming a fraction of the power (2 W compared to 20 W for this experiment). Figure 1-23 shows a schematic timing diagram. The relatively high frequency AC carrier is responsible for permitting the DBD to operate. The unsteady period allows the possibility of a much lower pulsing frequency.

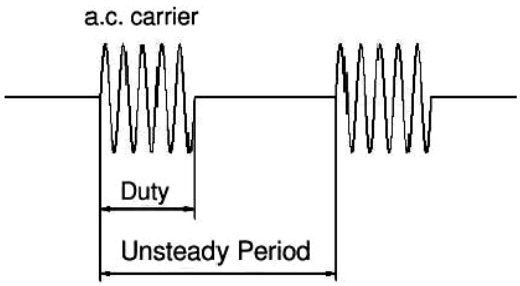

Figure 1-23 A schematic showing a signal timing diagram. (Corke et al., 2004)

Postl et al. (2003) mentioned that while pulsed VGJs promote re-attachment of the separation bubble at least partly due to bypass transition in the shear layer, they conjecture that the separated flow may also be linearly unstable to two-dimensional disturbances, which would permit forcing with specifically selected frequencies. Postl et al. (2011) conducted a DNS study of the effect of a span-wise array of pulsed VGJs on flow separation. Like Zhang and Zhong (2010), they observed hairpin vortices immediately downstream of the VGJ orifices. For the low free-stream turbulence conditions of their study, they observed that the strength of these stream-wise vortical structures decay as they convect downstream. Like Bons et al. (2005), they suggested that the stream-wise structures generated by the pulsed VGJs may not be primarily or directly responsible for effective control of separation, unlike the case of steady jet injection. Instead, they focused on the significance of the formation and growth of *span-wise* coherent vortices ("rollers") further downstream. Despite the three-dimensionality inherent to localized VGJ injection holes, they found that the downstream growth of the two-dimensional (i.e., span-wise averaged) disturbance component from the jets was exponential in nature, and in excellent agreement with the predictions of linear stability theory. In addition, vertical jets (flow emerging normal to the wall and stream-wise aligned) and angled jets (flow emerging at a shallow pitch angle of 30° to the wall and high skew angle of 90°, i.e., span-wise directed) were nearly indistinguishable in this regard. They concluded that the separation control effectiveness of pulsed VGJs was owing to a link to the KH instability inherent to the separated shear layer.

Postl et al. (2011) also studied the effect of forcing frequency on separation control. Measuring the displacement thickness of the shear layer downstream of the VGJs as a measure of separation control effectiveness, they varied the pulsing frequency of the VGJ. They found that a set of "low frequency" cases, involving VGJ pulsing frequencies that were equal to or lower than the natural frequency of instability, were effective for separation control, with the effectiveness comparable between cases. In contrast, "high frequency" cases involving VGJ frequencies higher than the natural frequency of instability showed dramatically lower effectiveness. They concluded that enough higher harmonics were produced from the VGJ pulsed flow that the base flow could select the most dangerous mode from the broad spectrum of disturbances. They suggested that this might explain why a single optimal frequency is not often observed in separation control experiments. However, since lower harmonics are not generated by the flow, control effectiveness dropped off for pulsing frequencies that exceeded the most unstable value.

Gross and Fasel (2010) numerically studied the relative effectiveness of several different configurations of VGJs. Like Postl et al. (2011), they found that pulsed VGJs excite span-wise coherent shedding vortices. They found that two-dimensional span-wise coherent vortices were more efficient for separation control than transition to turbulence, and the resulting three-dimensionality downstream. They observed that the two-dimensional component of the disturbance from the VGJs increased as the span-wise spacing of the injection holes was decreased; this suppressed distortions of the span-wise vortices, leading to more effective control. The best separation control was obtained by harmonic blowing through the highly two-dimensional case of a span-wise slot, using less momentum than the combined momentum of injection through the discrete VGJ holes. This slot configuration was noted to replicate the flow field of a plasma actuator.

Jolibois et al. (2008) studied the chord-wise location of placement of a DBD plasma actuator on a NACA 0015 airfoil with changing angle-of-attack, and concluded that the actuator is most effective when located close to the natural separation point of the flow, which is in agreement with this author's findings.

1.3. Scope

A majority of the research in flow separation control involves flows with low free-stream turbulence intensity. Such flows are amenable to linear stability analyses, and maximum efficiency of flow control is often experimentally determined to occur at frequencies of natural instability. Relatively few researchers have studied flow control in cases of high free-stream turbulence (exhibiting "bypass transition), and fewer still have used plasma actuators for doing so. In addition, to the best of the author's knowledge, plasma actuators have not been used for flow control with passing wakes.

The scope of the present work is to experimentally demonstrate the use of plasma actuators for flow separation control over the suction surface of an LPT airfoil, with and without passing wakes.

This work is part of a project funded by the National Aeronautics and Space Administration (NASA) to investigate the feasibility of using a plasma actuator for flow control in aviation gas turbine engines. Collaborating researchers at the University of Minnesota involved in this project worked on several aspects of the plasma actuator: numerical modeling of the dielectric barrier discharge plasma; thrust and power measurements obtained from the plasma actuator by varying materials, geometry, and input electrical excitation parameters; thrust enhancement strategies using nano-second pulses.

2. Experimental test facility

The present work demonstrates flow control using a plasma actuator with and without wakes, at the Reynolds number Re_{Lss} = 50,000 and inlet free-stream turbulence intensity of 2.5%. These conditions are representative of flight at cruising altitudes, especially in smaller engines at higher altitudes.

This flow was produced in a low-speed wind tunnel equipped with a low pressure turbine airfoil passage with a Pratt & Whitney Pack-B profile, and a wake generator. A plasma actuator was designed in collaboration with other researchers at the University of Minnesota. Specifications of the experimental facility are described in this chapter.

2.1. Low-speed wind tunnel

A low-speed, blow-down, open-circuit wind tunnel was used for this study. The facility is equipped with a blower, a filter box, a flow redistribution section, a heat exchanger section for fine spatial and temporal control of flow temperature, a flow conditioning and settling chamber, a contraction nozzle, and a jet-grid turbulence generator. This wind tunnel was designed and built by Wang (1984), and modified by Kim (1990).

Figure 2-1 shows a schematic of the wind tunnel and the airfoil passage. A New York Model 244 centrifugal blower drives the flow in the wind tunnel. The blower has flow rate capacity of 5500 scfm. It is powered by a 3-phase, 230 V, 10 HP Westinghouse Model 680B103G37 electric motor. A 10 HP Louis-Allis Lancer Model 92245 variable-frequency motor controller was used to control the motor and blower. A large filter box constructed around the air intake for the wind tunnel is used for removing particles larger than 5 μm, to prevent damage to hot-wire sensors from dust and debris drawn in by the blower.

A series of grids and honeycomb matrices are used for swirl removal, and to improve flow uniformity. A heat exchanger section located farther downstream is capable of providing spatial uniformity of temperature to within 0.1 ºC. A flow conditioning and settling chamber, equipped with a 24-mesh screen pack, is used to re-orient the flow after the 90º bend in the tunnel, and to reduce free-stream turbulence.

The flow then passes through a contraction nozzle with a contraction ratio of 10.7:1, increasing the flow velocity and further reducing the turbulence intensity. The nozzle has an inlet area of 0.914 m × 0.914 m, and an outlet area of 0.685 m × 0.114 m. The high outlet nozzle aspect ratio (height/width) of 6 minimizes the end-wall effects on the flow.

The wind tunnel can be equipped with a passive rod grid turbulence generator downstream of the nozzle, shown in Figure 2-2. The grid is constructed from 11 steel rods of 0.95 cm diameter. Nine of these are horizontally-oriented; 2 are vertical. If this grid is not installed in the facility, the exit flow has a free-stream turbulence intensity (FSTI) of approximately 0.5%. With the rod grid in place, the FSTI of the exit flow is approximately 2.5%.

If higher levels of FSTI are desired, the rod grid can be used in “blown” mode, rather than passively. A pressurized header can be used to blow air through holes in the hollow rods of the grid. Each rod has 5 pairs of 0.8 mm diameter holes. Each pair of holes is oriented ±60º to the downstream direction of the flow.

The entire study in this document was carried out with the rod grid installed and not blown, i.e., in passive mode, producing an exit flow FSTI of 2.5%.

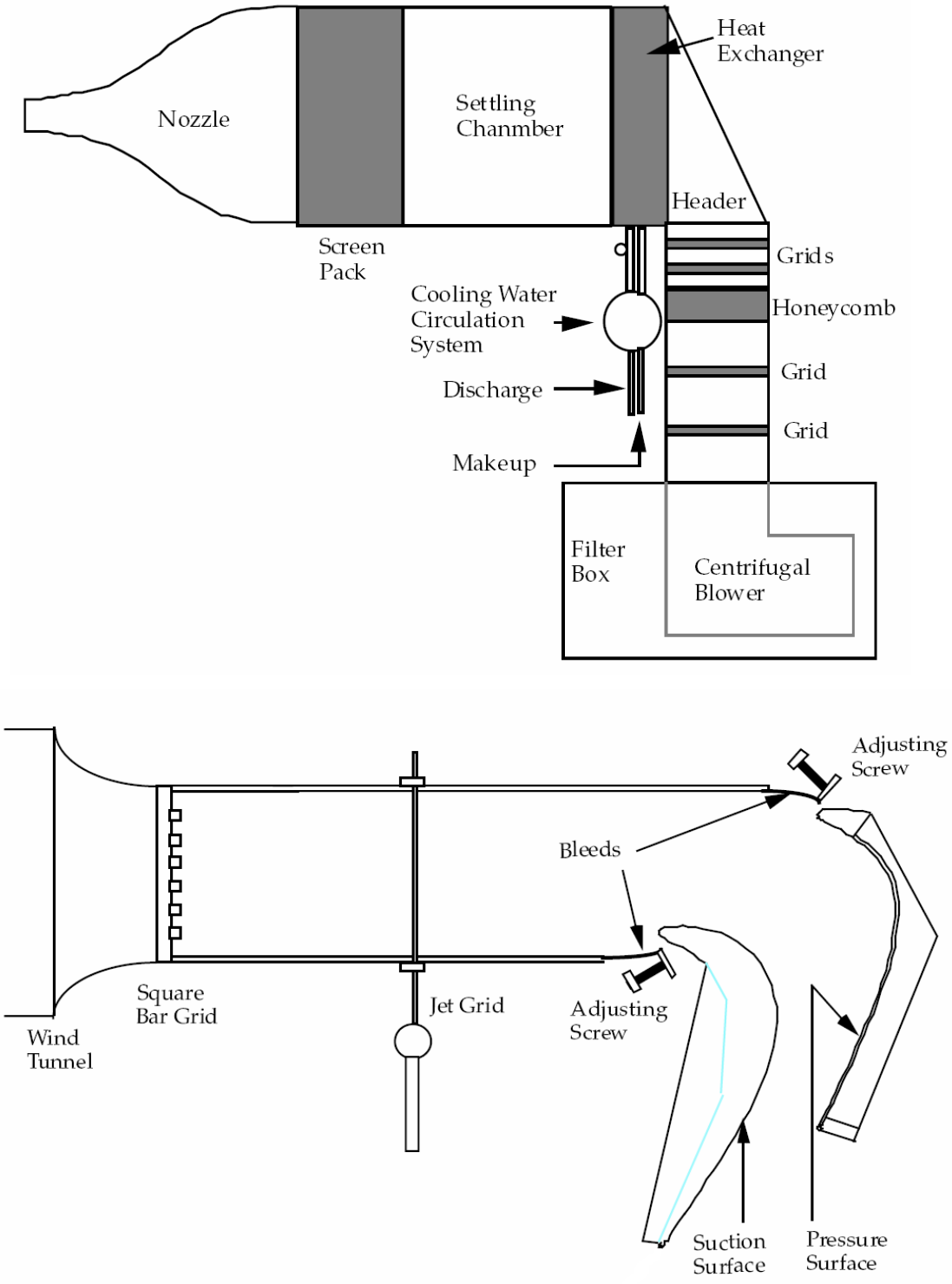

Figure 2-1 Schematic showing the low-speed wind tunnel (top), and the development section and Pack-B passage, as attached to the end of the nozzle (bottom) (Simon et al., 2000).

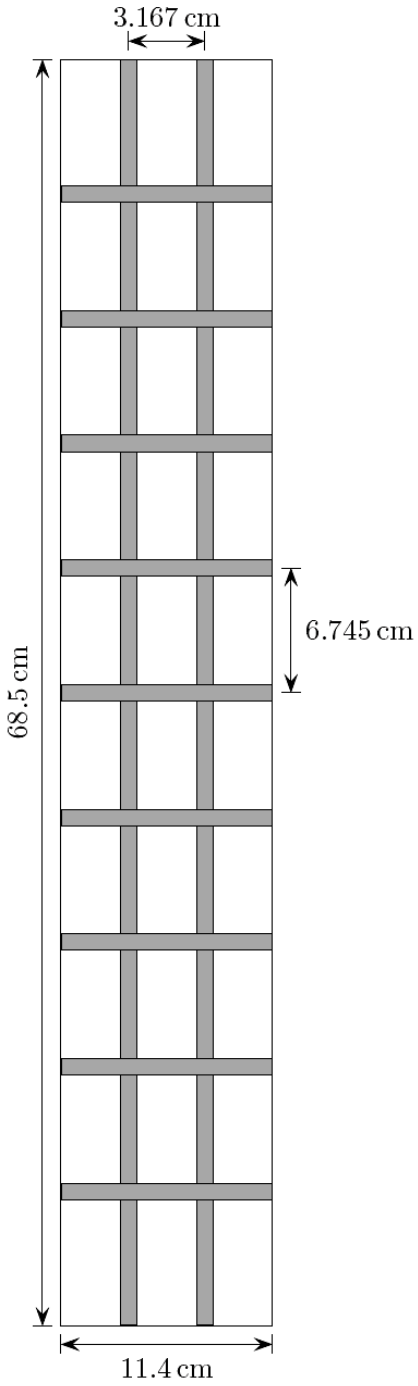

Figure 2-2 Rod grid generator used for FSTI = 2.5%. The rods are 0.95 cm in diameter. (Kaszeta et al., 2003)

2.2. Low pressure turbine airfoil passage

The airfoil geometry selected for this study of separation control is the Pratt & Whitney Pack-B (sometimes spelled in the literature as Pak-B) low pressure turbine profile. One suction surface half-blade and one pressure surface half-blade form the single passage test section. A schematic of the two half-blades is shown in Figure 2-3.

The pressure surface is made of a thin sheet of Lexan, supported by ribs. An access slot can be opened on this surface to permit probe access to the fore section of the suction surface of the airfoil.

The suction surface is fabricated from a phenolic laminate to permit a 1.3 mm thick glass dielectric to be flush-mounted on the suction surface in a recess. This phenolic material allowed excellent machinability, which was important not only for generating the profile, but also to accurately machine the recess to accommodate the thickness of the dielectric for the plasma actuator.

Adjustable pressure bleed slots are located in the passage approach duct. Tufts were used for confirming stagnation on the leading edge of each blade. Static pressure measurements from taps located on the suction surface were used to confirm agreement with the high Reynolds number Pack-B pressure profile. Tailboards were originally attached to the section, but were later found unnecessary by Qiu (1996), and removed. Further details on the test section may be found in Simon et al. (2000).

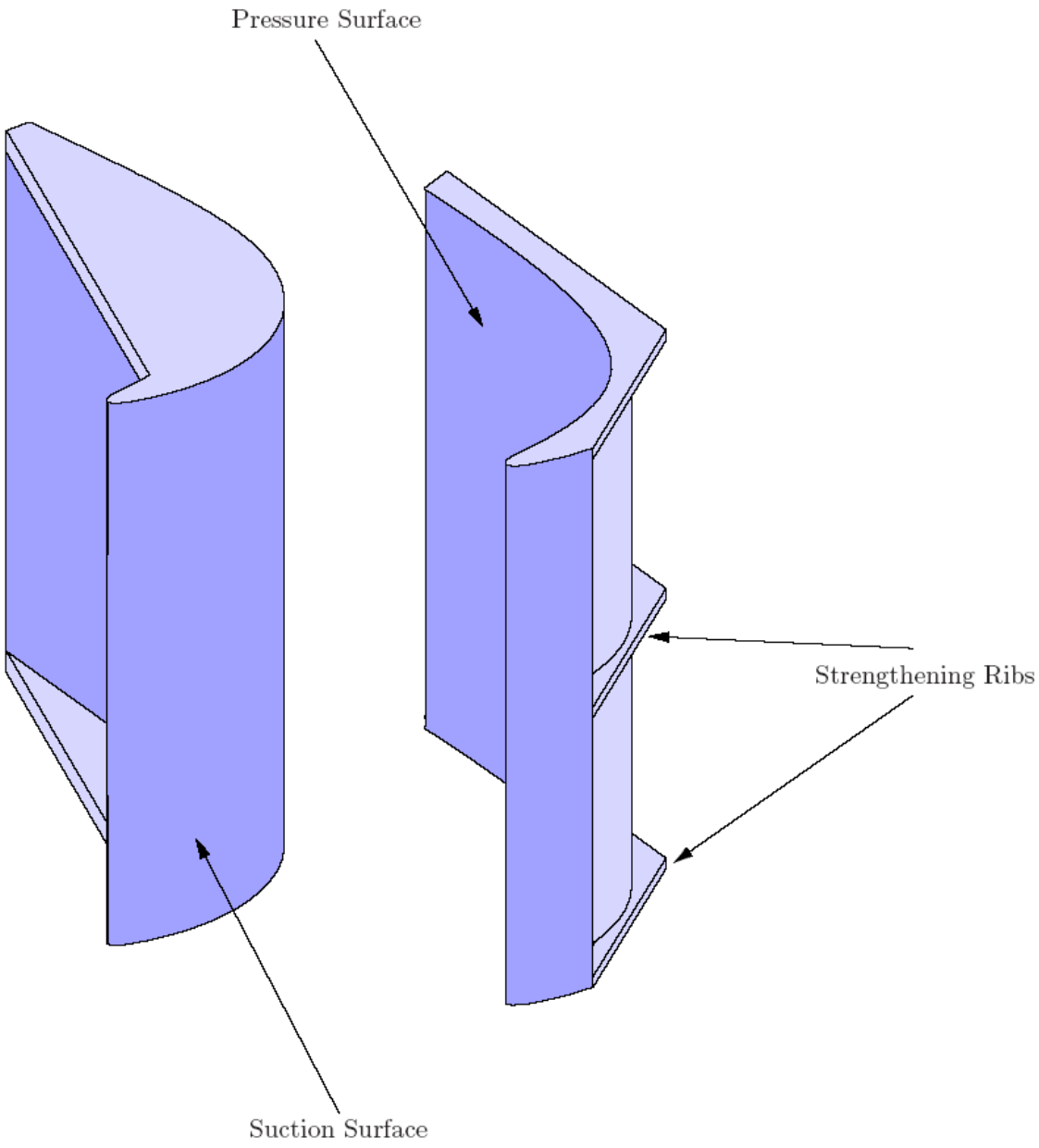

Figure 2-3 The cascade simulation test section (Kaszeta et al., 2003)

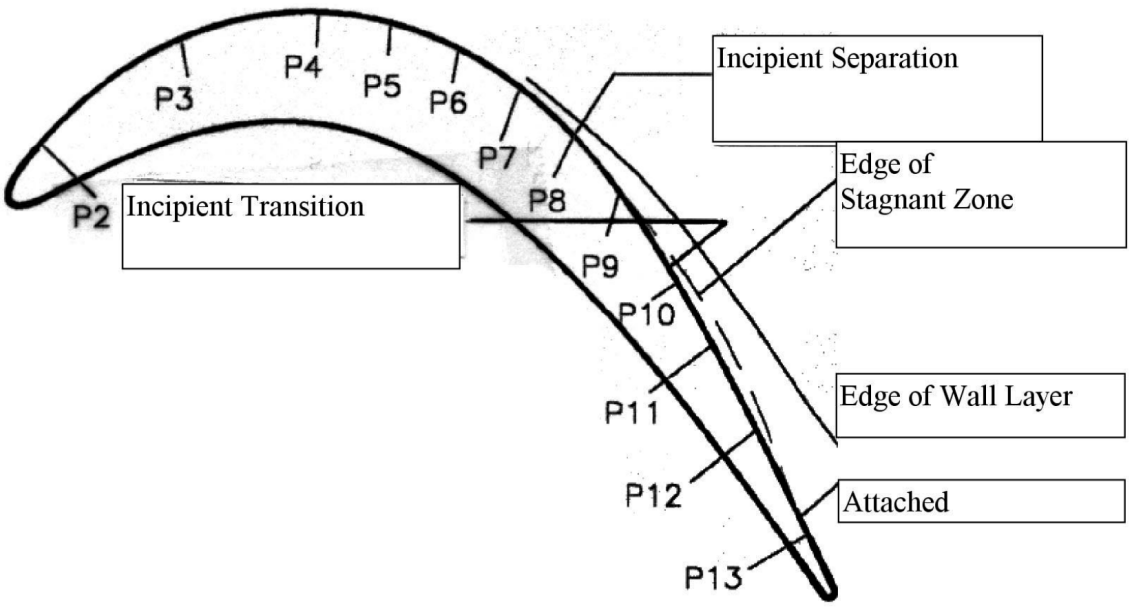

Figure 2-4 Sketch of Pack-B airfoil under steady flow, with Re_{Lss} = 50,000 and FSTI = 2.5%, showing approximate locations of separation and transition (Simon et al., 2000)

2.3. Wake Generator

The facility is equipped with a wake generator, which comprises a moving sled that holds wake-generating rods, along with its associated driving mechanism. The wake generator was originally designed by Yuan (1999), followed by several major modifications by Kaszeta (2000). As a part of the present work, an air-bearing system for the push bar mechanism was developed to enhance the existing wake generator assembly, reducing friction, vibration, and wear on the assembly.

The sled slides on an H-beam rail. A push bar that is connected to the sled with a pulley-rope system is used to set it in motion. The push bar itself is driven by a speed-controlled motor assembly, through the action of forward and reverse friction wheels. A 120 V AC solenoid valve switching between two states acts upon a pneumatic cylinder, and is used to alternately switch the drive between the two friction wheels. This allows the sled to move back and forth on its rail. The pneumatic cylinder is pressurized using

the air supply line in the building. The solenoid valve is controlled with a solid state relay, which is, in turn, powered by a GPIB/IEEE-488 enabled power supply. By controlling the state of the power supply that is interfaced with a computer, the motion of the wake generator can be controlled by an appropriately written program.

Table 2-1 provides details of the components that comprise the wake generator drive.

Table 2-1 Components of the wake generator driving mechanism

Pneumatic cylinder	Bimba Model H-095-DUZ 0.75 inch diameter, 8 inch stroke
Solid state relay	Crydom D1210
Programmable power supply	HP 59501B

A photo-gate detector system is used with a picket-fence linear encoder attached to the sled to track the position of the sled during its motion. This system is also used to trigger data acquisition when the sled is set in motion. The detector is powered by a BK Precision 1686A DC regulated power supply.

The wake generator is vibrationally isolated from the remaining test section. Additionally, plastic flaps are present that permit the wake generating rods to pass through the flow passage with minimal leakage of the main flow.

Table 2-2 summarizes the geometric and wake-passing parameters for the turbine passage. A schematic indicating these parameters is shown in Figure 2-5.

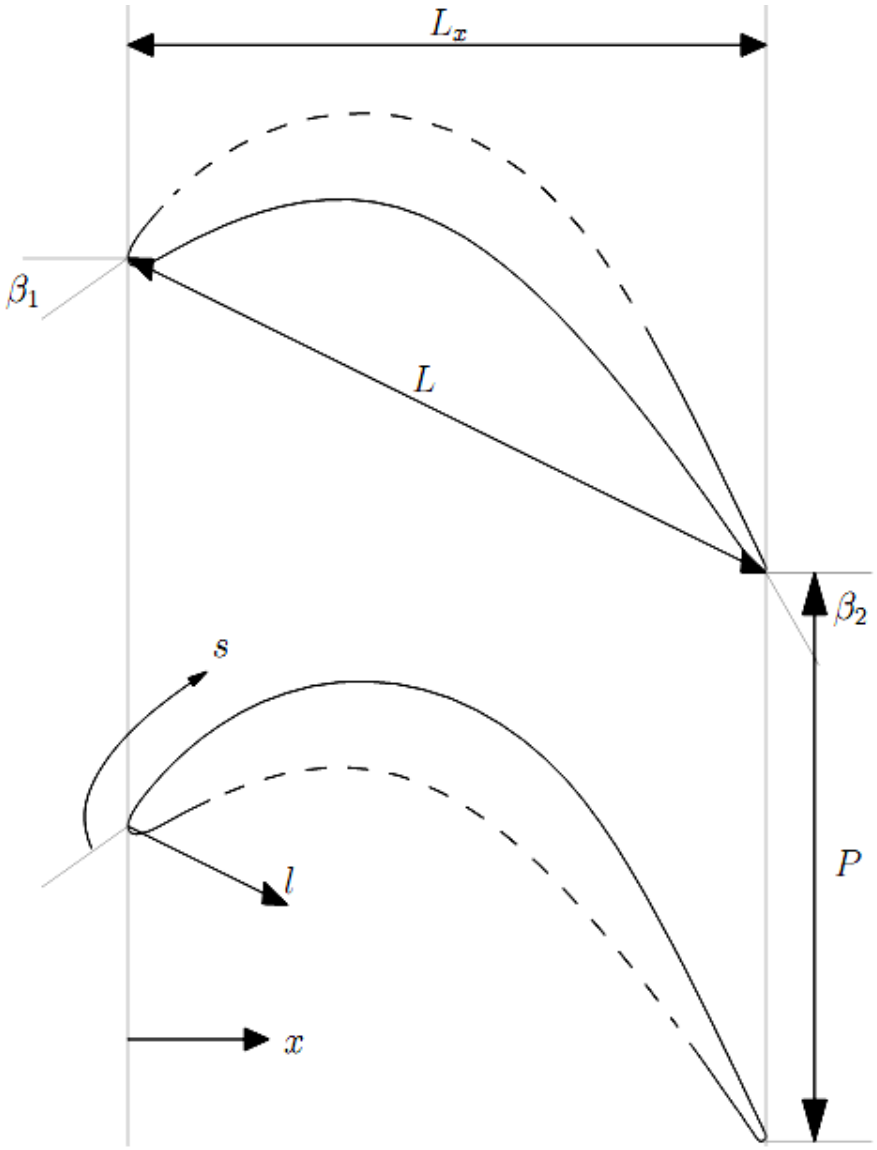

Figure 2-5 Schematic showing Pack-B turbine passage dimensions (Kaszeta et al., 2003).

Table 2-2 Pack-B turbine passage parameters (Kaszeta et al., 2003).

Chord length, L	114.3 mm
Axial chord length, L_x	103.57 mm
Suction surface length, L_{ss}	152.76 mm
Axial chord to chord ratio, L_x/L	0.906
Pitch to chord ratio, P/L	0.8
Aspect ratio (span/chord), L_z/L	6.0
Blade inlet angle, β_1	35º
Blade outlet angle, β_2	-60º
Velocity ratio of rod to axial flow, u_r/u_x	~ 0.70
Rod spacing to airfoil pitch ratio, L_r/P	1.0

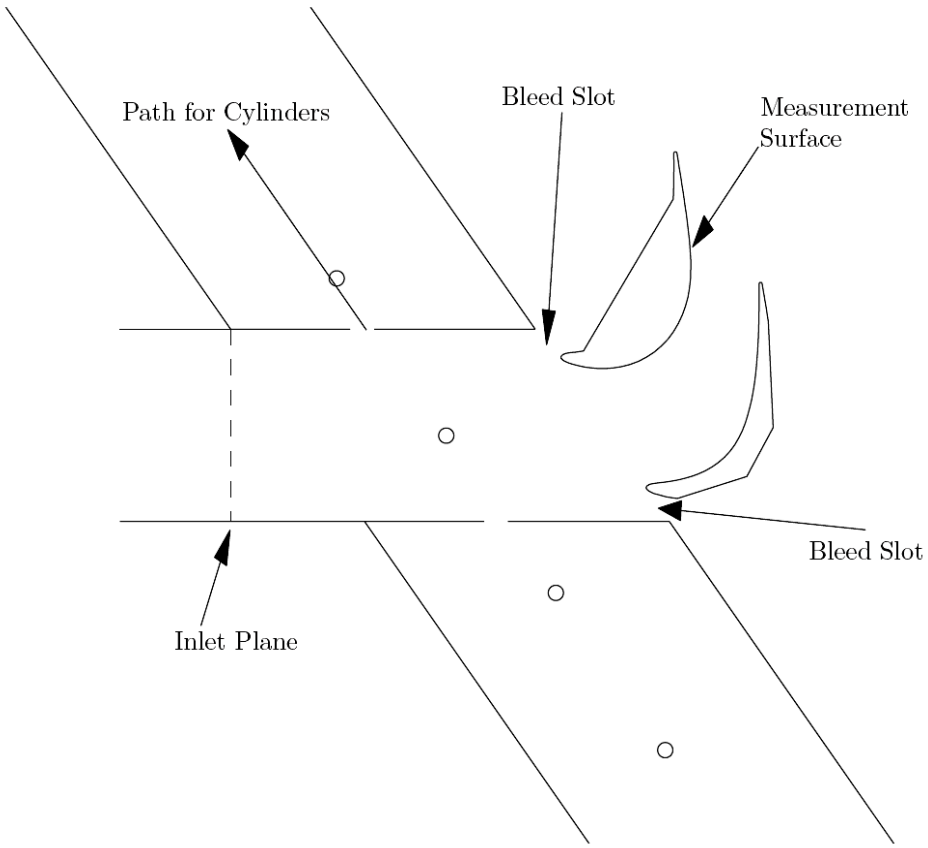

Figure 2-6 Cross-sectional view of the wake generator (Kaszeta et al., 2003).

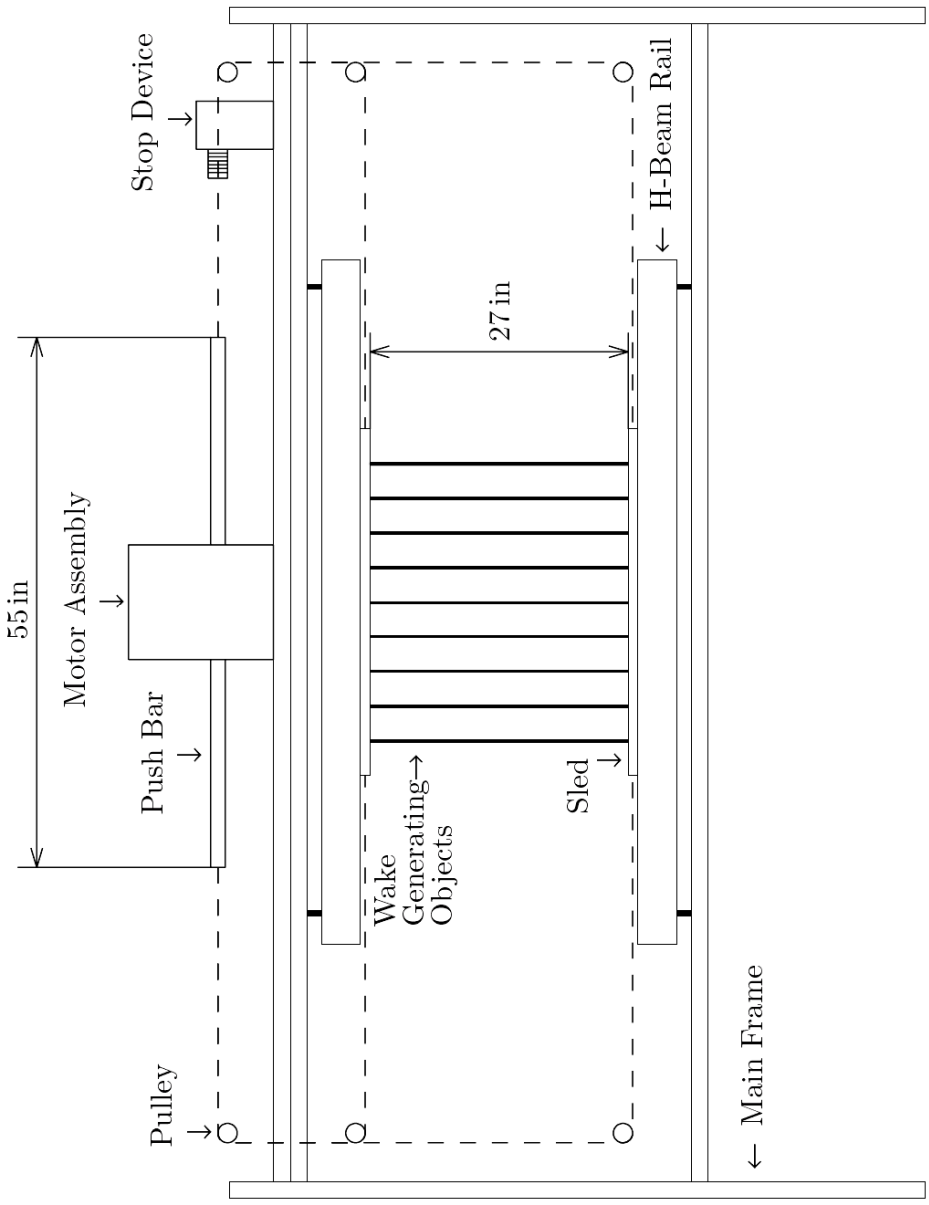

Figure 2-7 A schematic of the wake generator (Yuan, 1999)

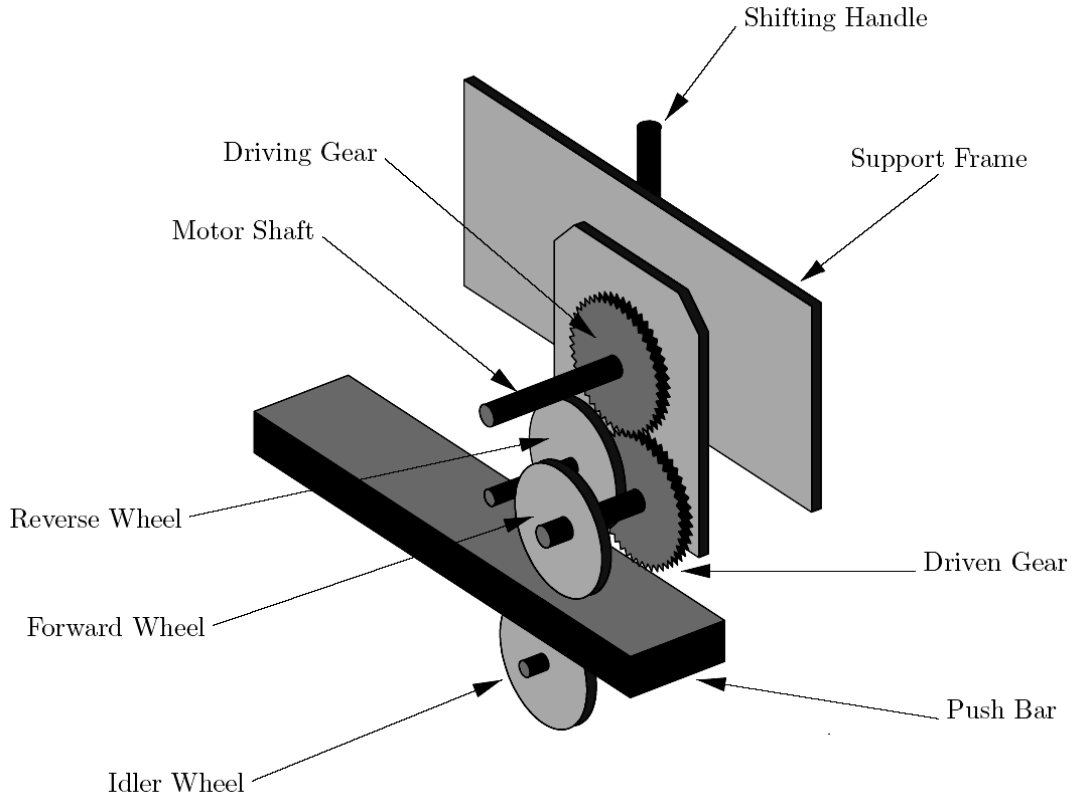

Figure 2-8 A schematic showing the transmission of motion from motor to the push bar in the wake generator (Yuan, 1999). This design was later modified to add return gears (Kaszeta et al., 2003), and an air-bearing mechanism (present author).

2.4. Plasma Actuator

The results in this study were obtained using an actuator constructor using a 1.3 mm glass dielectric, except where noted. A discussion of the process for the selection and fabrication of this dielectric can be found in the Appendix – Dielectric selection for the plasma actuator.

The plasma actuator is constructed by attaching electrodes to both sides of the glass dielectric. A schematic is shown in Figure 2-9. The single electrode on the non-flow side of the dielectric is encapsulated with insulating film, so that no plasma discharge is

formed on that side. In our case, this electrode is the grounded electrode, and is also referred to as the second electrode. The powered electrode on the flow side of the dielectric immediately upstream of the grounded electrode is referred to as the first electrode. In this study, a third electrode is also present. It is on the flow side of the dielectric, and downstream of both the first and second electrodes. The third electrode is connected to the first electrode through a diode.

Each electrode is a strip of copper tape that is 0.08 mm thick (wall-normal direction) and 6.4 mm wide (stream-wise direction). The trailing edge of the first electrode is aligned with the leading edge of the second electrode, and is 10 mm upstream of the leading edge of the third electrode.

When only the first and second electrodes are activated, it is referred to as a two-electrode configuration, which is the standard configuration for most plasma actuator flow controllers. When all three electrodes are active, it is a three-electrode configuration. In the present work, both two- and three-electrode configurations were used for the cases with no passing wakes. The wake-passing study was made with the two-electrode configuration only.

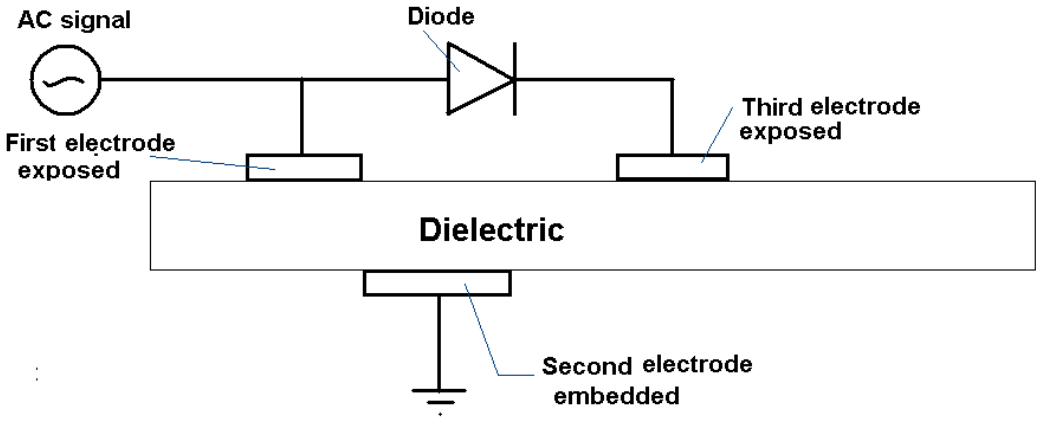

Figure 2-9 Schematic showing the actuator arrangement for the three-electrode geometry. Flow is from left to right.

The input waveforms for the actuator in this study were produced using a dual-channel Tektronix AFG 3022B arbitrary function generator. A Tektronix P6015A 1000X high-voltage probe was used to measure the actuator voltage, while a Pearson 6585 current transformer was used to measure current flow in the actuator circuit. A Tektronix TDS 220 two-channel digital oscilloscope was used to monitor a range of input and output signals.

The continuous or intermittent waveform produced by the function generator was amplified by a high voltage amplifier. Preliminary studies were conducted using a Trek 20/20C model amplifier. Later results were obtained using the Trek PD05034 model amplifier, which offered significantly improved performance for fast-changing signals with the possibility of high peak current demands due to streamer formation.

Table 2-3 summarizes the key specifications of the high voltage amplifiers used to drive the actuator in this study.

Table 2-3 Specification of the high voltage amplifiers used in this study

	Trek 20/20C	**Trek PD05034**
Output voltage	0 to ±20 kV	0 to ±7.5 kV
Output current	0 to ±20 mA	0 to ±50 mA
Peak current	not specified	±160 mA for 60 μs
Slew rate	> 450 V/μs	> 1000 V/μs
Large signal bandwidth	> 3.75 kHz	> 15 kHz

2.5. Data Acquisition equipment

For measurements that were taken with the glass pressure tube, the traverse system comprised of a National Aperture MM-4M-EX-140 MicroMini stage, driven by a 13 mm MTR-13-16E DC servo motor, and controlled by a National Aperture MC-CQ-B controller. The accuracy of the traverse is specified at 1 μm per 25 mm of travel.

A serial-to-USB converter was used to interface the controller with a computer. All measurements of pressure were manually taken using a Dwyer Model 1430 Microtector manometer. Details of these measurements can be found in Section 3.2.

For hot-wire measurements in the flow with passing wakes, a single-channel TSI Model 1750 constant temperature hot-wire anemometer bridge was used. TSI Model 1218-T1.5 single-sensor boundary-layer probes were used in this study.

In order to filter noise from the 9 kHz sinusoidal AC signal driving the actuator, a Stanford Research Systems Model SR650 pass filter was used to low-pass filter the output signal of the anemometer at 5 kHz. The filter has a specified attenuation of 115 dB/octave.

The low-pass filtered hot-wire signal was then sampled using an IOTech ADC 488/8SA analog to digital converter at 100 kHz, with 70,000 samples taken per pass of the wake generator. A separate IOTech ADC 488/8SA was used to sample the output voltage of the photo-gate linear encoder system. Both IOTech converters were activated by an external trigger signal from the photo-gate linear encoder.

A detailed description of the probe, and further discussion of the hot-wire measurements can be found in Section 3.3.

The traverse system for the hot-wire measurements comprised of a Velmex UniSlide stage driven by a Superior Slo-Syn stepping motor, and controlled by a Velmex VXM

controller. The resolution of the stepping motor is specified as 5 μm. An IOTech Serial 488A Bus Convertor was used to connect the controller to a GPIB/IEEE-488 bus.

The GPIB/IEEE-488 bus carrying signals to and from the IOTech ADC devices and the traverse controller was connected to the USB port of a computer using a National Instruments GPIB-USB-HS converter. C programs were used on this Linux-based computer to control the acquisition of data.

2.6. Ozone-related safety equipment

For monitoring the levels of ozone generated by the DBD discharge, an Eco Sensors A-21ZX ozone sensor (Figure 2-10) was used at all times during the actuator study in the LPT facility. The monitor is capable of detecting ozone levels from 0 to 10 ppm in 0.01 ppm increments.

Figure 2-10 Eco Sensors A-21ZX ozone monitor used for monitoring ozone levels in the test environment

For the flow experiments conducted in a large, open lab area, the monitor indicated a steady 0.02 ppm after running the actuator for about 15 minutes, when located approximately 0.5 m below the actuator. The odor threshold concentration for ozone is considered to be 0.01 – 0.02 ppm. The OSHA Permissible Exposure Limit (PEL) is 0.1 ppm.

In the author's experience, the human olfactory and respiratory systems are noticeably more sensitive to the generated ozone than the aforementioned monitoring device. Ozone odors in the near vicinity of the actuator were evident within seconds of discharge initiation. Symptoms including respiratory dryness and irritation, mild nausea, and headaches were observed for longer periods of exposure involving being present in the same room as the discharge. Subsequently, a 3M 7502 half-face mask was used for protection during testing. This mask is equipped with a 3M #2097 PR P100 filter rated for operation at ozone concentrations of ten times the OSHA Personal Exposure Limit (PEL), i.e., up to 1.0 ppm.

No obvious ozone-related adverse health effects were observed when the mask was used.

3. Instrumentation, experimental procedures, and data processing

3.1. Background

Taking reliable flow measurements in the vicinity of plasma actuators is challenging due to the possibility of interaction of the electrical noise and electric field generated by the plasma discharge with components of the measurement system. This chapter describes the instruments and experimental methods used in this study.

It is relatively uncommon for studies involving flow measurements near plasma actuators to consider or mention possible interference effects due to the plasma discharge. A few studies that have commented on this topic are mentioned here.

Magnier et al. (2007) used a glass tube with an inner diameter of 0.8 mm to measure flow in the vicinity of a DC discharge. They mention the danger of electrical discharge with a conventional metal probe. They also took flow measurements using Particle Image Velocimetry (PIV). They observed that the plasma discharge was modified due to the presence of tracer particles produced by an oil drop generator. A higher discharge current was noted, as well as a difference in the appearance of the discharge. The researchers did not notice this difference with smoke from an incense stick, and conducted the PIV measurements using this smoke. No mention was made of the possibility of the discharge influencing the motion of the smoke particles.

Jukes et al. (2008) acknowledged the possibility of electrical interference from the actuator, and chose to ignore all hot-wire anemometry data taken during the active pulsing time of their actuator.

Jukes and Choi (2012) studied the use of DBD discharge actuators as vortex generators. They acknowledged the possibility that seeding particles used for their PIV measurements may be influenced by the electric field of the discharge. They expressed concern about the validity of these measurements in the vicinity of the discharge. They were confident about measurements that extended beyond 40 mm downstream of the actuator.

In the present study, measurements were taken to demonstrate and characterize the effect of a DBD plasma actuator as flow separation control device. The flow field was located in a Pack-B LPT airfoil passage, with Re_{Lss} = 50,000, and inlet free-stream turbulence intensity of 2.5%.

One set of measurements, referred to as steady flow measurements, were taken in the airfoil passage without operation of the wake generator for upstream wakes. These were measurements of total pressure taken using a glass tube and a micro manometer. The second set of measurements was taken in the same flow, but with upstream wakes passing, resulting in a highly unsteady flow. The temporal response of a total pressure tube is inadequate for characterizing this flow. Hot-wire anemometry was used to take time-varying measurements of velocity that were ensemble-averaged.

The experimental methods used will be discussed in this chapter, along with sources of error, and corrections applied.

3.2. Total pressure measurements

Total pressure or stagnation pressure is the pressure obtained by isentropically decelerating the flow to rest. It is the sum of the dynamic and static pressure at a location.

The quality of total pressure measurements depends on the characteristics of the flow, as well as the construction of the probe being used, and its orientation to the flow. Major

parameters influencing the measurement are: angle of incidence of the probe to the flow, probe geometry, Reynolds number, Mach number, presence of velocity gradients and turbulence, and proximity to walls.

Total pressure measurements are most commonly performed using small diameter metal tubes in order to obtain measurements with good spatial resolution. While such metal total pressure tubes with smaller diameters are readily available, arcing has been observed in the vicinity of the charged dielectric when metal probes are employed. An arc-like discharge can affect the local velocity field, thus affecting the measured total pressure. To overcome these limitations, a glass tube was used in this study. One of the tradeoffs of using a glass tube is the loss of resolution in the wall-normal direction because it is challenging to fabricate small diameter glass tubes. In the present study, a glass tube with an outer diameter of 1.2 mm and an inner diameter of 0.6 mm was used. All total pressure measurements were relative to the passage exit static pressure, which is open to atmospheric pressure. A picture of one such tube is shown in Figure 3-1.

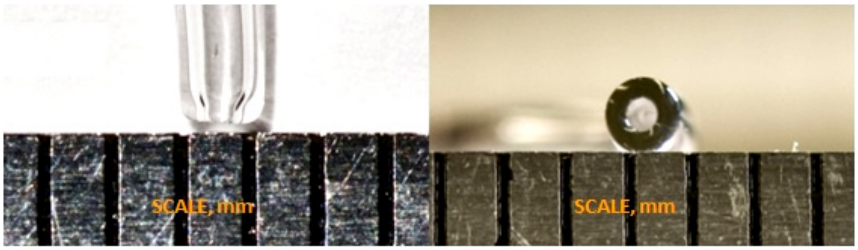

Figure 3-1 Glass total pressure tube used for total pressure measurements. The relevant scale is adjacent to each view of the tube, in millimeters.

The pressure measurements were taken using a Dwyer Model 1430 Microtector manometer. This device has a pressure range of 0 to 51 mm (0 to 2 inches) of water column, and is specified to be precise to $\pm 13 \times 10^{-3}$ mm (±0.00025 inches) of water column.

The manometric fluid is distilled water mixed with a small quantity of fluorescent green dye. The resulting solution is electrically conductive. A needle-tip micrometer gauge completes an electrical circuit when it makes contact with the meniscus of the fluid column, which registers as a high-current state.

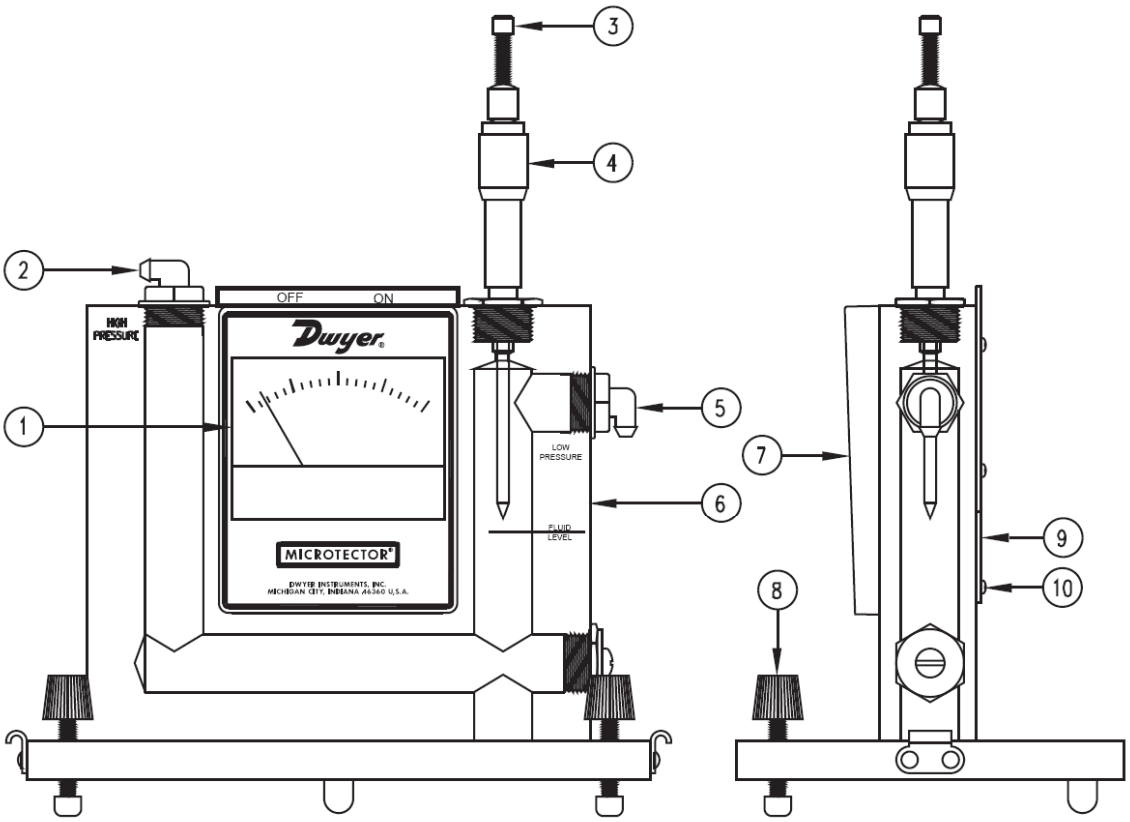

Figure 3-2 Schematic showing Dwyer® Microtector® 1430 manometer (from Dwyer)

Corrections and uncertainty for pressure measurements

The uncertainty estimated at 95% confidence interval based on the standard deviation of pressure measurements is less than 5%. However, other sources of error in the measurements exist, including streamline displacement due to blockage, viscous effects due to low Reynolds number (based on probe-diameter), and errors due to unsteadiness in the separated shear layer. These effects are discussed below, along with corresponding corrections made to the pressure measurements.

Near the wall, the blockage effect of a pressure tube causes streamline displacement, which produces a lower velocity measurement than is accurate. Additionally, when a pressure tube is placed in a shear flow with a positive velocity gradient, as in a boundary layer, the tube registers a higher velocity than is accurate. Figure 3-3 shows a schematic of these effects. Well-known corrections exist for these effects, which oppose each other in a typical attached wall-bounded flow.

A simple and popular formulation is due to (MacMillan, 1954). In a shear flow, the correction applied to the wall-normal distance y of the probe is constant, given by

$$\frac{\Delta y}{d} = 0.15 \qquad (1)$$

Near the wall, for y/d < 2, the correction is applied to velocity instead of wall-normal distance, given by

$$\frac{\Delta u}{u} = 0.015 \exp\left[-3.5\left(\frac{y}{d} - 0.5 \right) \right] \qquad (2)$$

Equations 1 and 2 are meant to be applied near the wall additively.

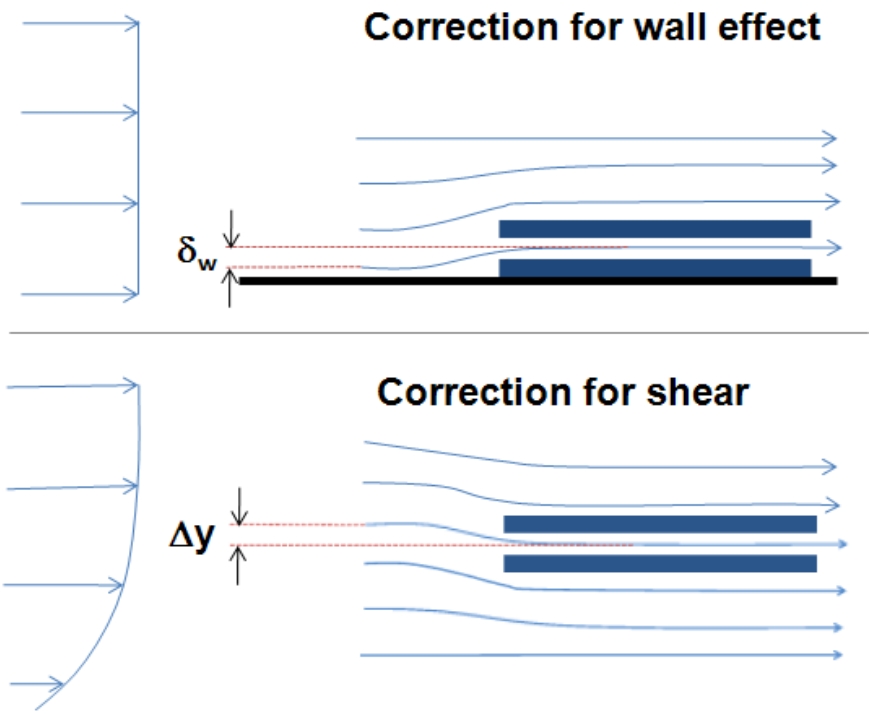

Figure 3-3 Schematic showing streamline displacement due to the presence of the wall, and due to shear.

McKeon et al. (2003) also suggest a formulation for pitot-tube displacement and wall correction, which was also evaluated for the present study. Their displacement correction for shear is given by

$$\frac{\Delta y}{d} = 0.15\tanh(4\sqrt{a}) \qquad (3)$$

where

$$a = \frac{d}{2u_{truecenterline}}\left.\frac{du}{dy}\right|_{centerline} \qquad (4)$$

is a measure of the local velocity gradient.

Their proposed wall correction is based on a correction to y, rather than to u, unlike the MacMillan wall correction. If the correct pressure is read at

$$y = 0.5d\left(1+\frac{\delta_w}{d}\right), \qquad (5)$$

δ_w being the wall displacement correction, then δ_w/d equals 0.15 for $d^+ < 8$, 0.12 for $8 < d^+ < 110$, and 0.085 for $110 < d^+ < 1600$, with $d^+ = du_\tau/\nu$, and $u_\tau = \sqrt{\tau_w/\rho}$.

Viscous corrections (due to low probe-diameter Reynolds number) were evaluated but not applied, since the correction was found to be negligible relative to the uncertainty in measurement.

Validation of pressure measurements

Shear-stress visualizations and hot-wire data from previous studies (Simon et al., 2000) show that when the pressure tube resides within the separation bubble in a zone of possible reversed flow, the velocities are low enough (≈ 0) for the effect of this back flow to be negligible. Unsteadiness levels are high relative to the local velocity within the separation bubble, but the absolute velocities have been measured to be near zero and, thus, the velocity fluctuations are also small in an absolute sense. As expected, unsteadiness corrections were found to be negligible in this case.

Hot-wire velocity data from Simon et al. (2000) that were taken under identical conditions, but without the actuator present, were used for comparison and validation of the total pressure measurements of the present study.

Figure 3-4 shows the comparison of these hot-wire data with total pressure measurements from the present study converted to velocity, both taken at stream-wise location $s/L_{ss} = 0.55$, which is in the vicinity of incipient separation. The hot-wire profile shown in the figure indicates that the flow is still attached. The wall static pressure used for computing the velocity was found by extrapolating the total pressure profile to the wall. There is significant stream-line curvature due to the airfoil passage geometry, causing the static pressure to increase away from the wall. The wall-normal gradient of static pressure was found from the free-stream wall-normal velocity gradient of the hot-wire data.

The displacement and wall corrections (McKeon et al., 2003) were applied to the data shown in Figure 3-4. Evaluating the corresponding corrections (MacMillan, 1954) produced results that are very similar to those seen in Figure 3-4. In both cases, good agreement is seen.

Stream-wise locations downstream of separation have wall-normal gradients of static pressure that vary according to the radius of the local streamline curvature. In particular, after the separated shear layer has undergone transition to turbulence and re-attachment is imminent, the static pressure in the shear layer increases toward the wall, which is opposite to the sense of the static pressure gradient farther upstream. Figure 3-5 shows a sketch of this phenomenon.

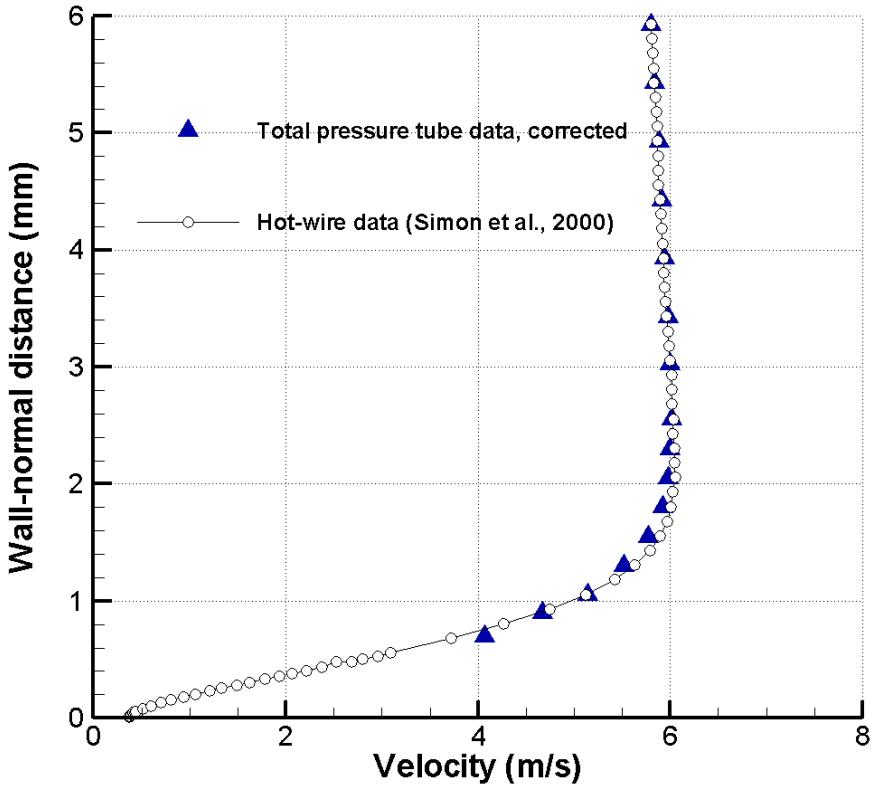

Figure 3-4 Comparison of the corrected total pressure tube measurements with hot-wire data (Simon et al., 2000). This stream-wise location of s/L_{ss} = 0.55 corresponds to incipient separation.

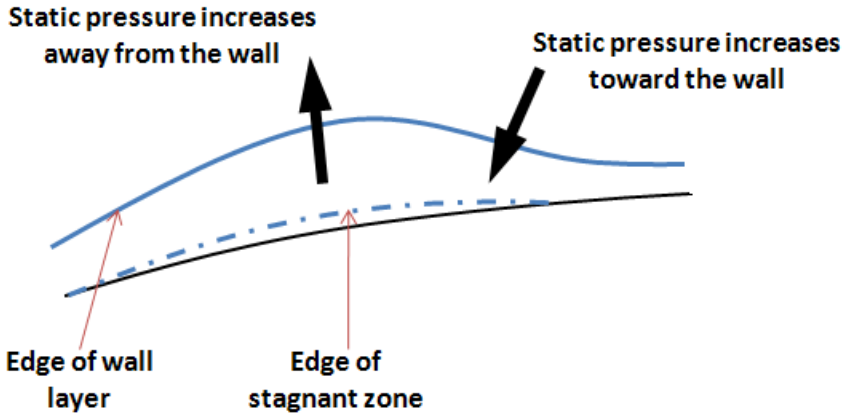

Figure 3-5 Schematic showing the change in sense of the static pressure gradient when the flow begins to turn toward the wall before re-attachment.

For illustration, a typical total pressure profile taken in separated flow (s/L_{ss} = 0.76, well downstream of separation) and converted to velocity is shown in Figure 3-6. The maximum velocity from the corresponding hot-wire measurement of Simon et al. (2000) was compared to the constant total pressure in the free-stream from the present study to compute the static pressure at the interface of the shear layer and free-stream. In this case, this corresponds to a wall-normal distance y ≈ 5.3 mm. The static pressure increases for y > 5.3 mm due to stream-line curvature in the free-stream, which is found from the slope of the hot-wire velocity profile in that zone and applied to the velocities calculated from total pressure, as shown in the plot. The static pressure also increases for y < 5.3 mm, because the flow begins to turn toward the wall before re-attaching farther downstream. This situation corresponds to the downstream arrow of Figure 3-5. For Figure 3-6, the velocities calculated from total pressure for y < 5.3 mm used the constant static pressure at y ≈ 5.3 mm, producing the disparity shown. Calculation using an estimated radius of curvature for the re-attaching streamline indicates that the magnitude of the disparity at the wall seen in Figure 3-6 is reasonable. It is simple to evaluate this static pressure gradient if the hot-wire data are used in conjunction with the total pressure measurements.

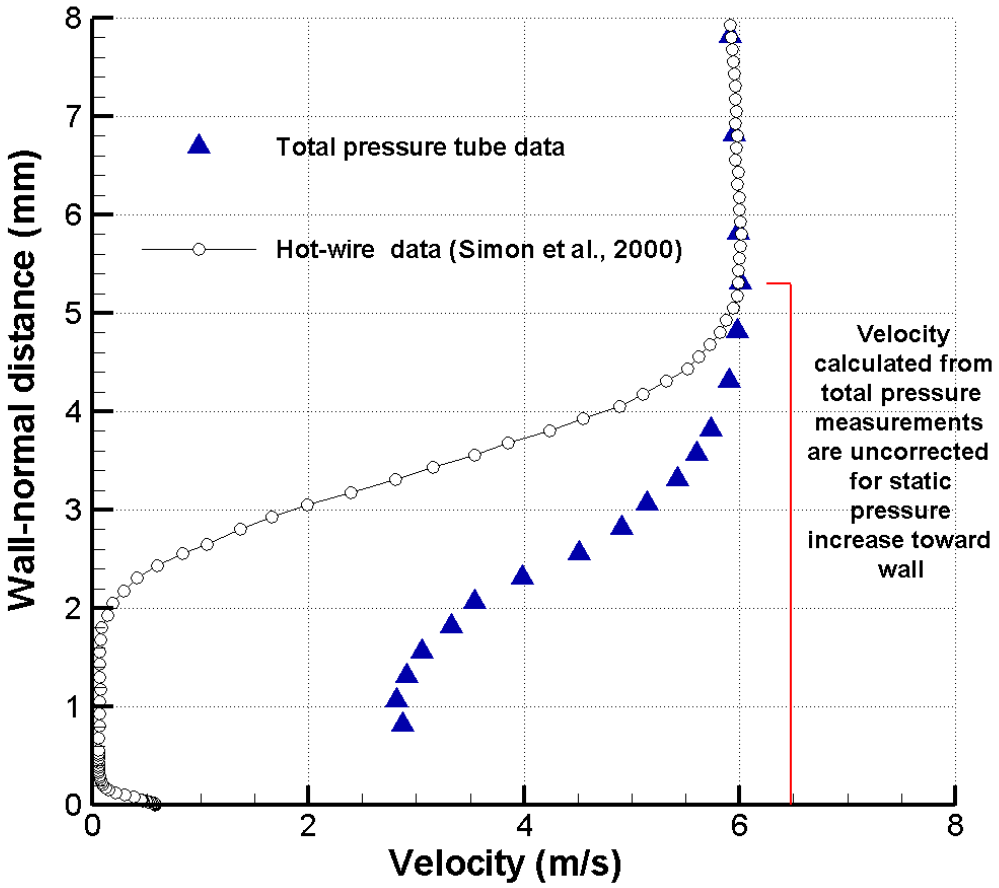

Figure 3-6 Comparison of the corrected total pressure tube measurements with hot-wire data (Simon et al., 2000). The flow is separated at this s/L_{ss} = 0.76 station, and static pressure increases toward the wall from the edge of the shear layer near the free-stream (not corrected for).

While all total pressure measurements from the present study could be converted to velocity with the use of the hot-wire data of Simon et al. (2000) to compute static pressure gradients, the above was primarily an exercise in validation of the present measurements. Total pressure, itself, is a reasonable parameter for evaluating separation control. For this study, the total pressure measurements are therefore not converted to velocity, but presented after correction for displacement due to shear and wall effects, as applicable. A wall-normal gradient of the total pressure is also computed, and is found to be a useful quantity for visualizing the zones of viscous losses in the flow (i.e. shear and boundary layers).

3.3. Hot-wire anemometry

While the glass pressure tube was found to be a satisfactory instrument for deducing the time-integrated state of the flow field in the airfoil passage without wakes, it is not a suitable instrument with the wake generator in use. The time scale of the interval between successive wakes is on the order of 0.1 s, which is too rapid for the glass tube system to resolve.

Constant temperature hot-wire anemometry was used for the study of flow control with passing wakes. Hot-wire anemometry has notable benefits of fast response, high spatial resolution, and high dynamic range.

In constant temperature hot-wire anemometry, a fine electrically-conductive wire element that forms one leg of a Wheatstone bridge is to measure flow velocity. When the wire element is exposed to a fluid flow of interest, convective heat loss proportional to the mass flux of flow of fluid past the sensor occurs. At thermal equilibrium, this convective heat loss to the flow is balanced by the I^2R_{wire} power due to the current supplied to the wire element by the bridge.

A feedback circuit is used to maintain the wire at constant resistance. Neglecting any change in resistivity, this is equivalent to keeping the temperature of the wire element constant. As the flow around the wire element changes, the convective heat transfer rate from the constant temperature wire also changes. The current supplied by the bridge to keep wire resistance R_{wire} (and wire temperature) constant therefore follows the flow.

A TSI Model 1750 constant temperature anemometer bridge was used with a TSI Model 1218-T1.5 single-sensor boundary-layer probe to take velocity measurements in the flow with passing wakes. The probe was maintained at a constant temperature of 250 °C during experiments. It has a platinum-coated tungsten sensing element that is 1.27 mm

long, and 3.8 μm in diameter. The overall dimensions of the probe are shown in Figure 3-7.

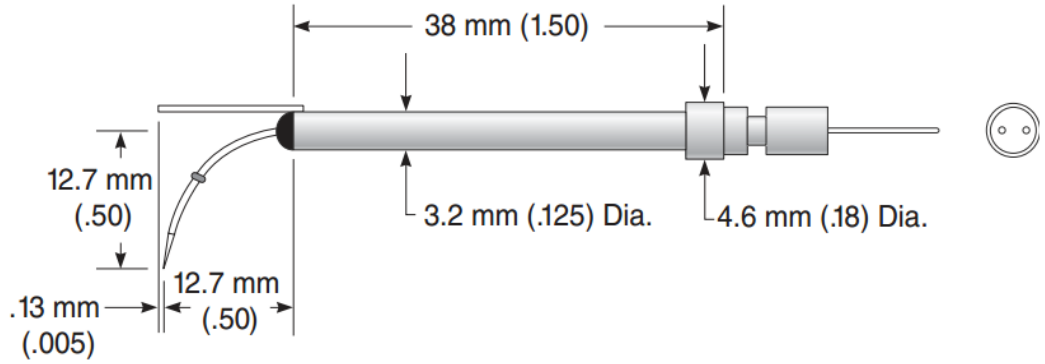

Figure 3-7 Schematic of a TSI Model 1218-T1.5 hot-wire probe (TSI Inc., 2006)

For a hot-wire sensor of known resistance held at constant temperature in a flow, the bridge output voltage E can be related to the velocity U of the flow by the well-known King's law:

$$U^n = A.E^2 + B \qquad (6)$$

A and *B* are constants that are obtained by a least-squares fit of the calibration data. A value 0.45 for the index n was determined to satisfactorily fit the calibration data for this study.

The hot-wire sensor was calibrated in the air calibration jet shown in Figure 3-8. Depending on the range of expected flow velocities, the sensor can be located within the inner chamber in the apparatus, or at the exit of the metering nozzle. A regulator was used to vary the air flow rate and velocity. For this study, the sensor was exposed to flow velocities between 0.3 m/s and 7 m/s. A Dwyer Microtector manometer was used to measure the static pressure just upstream of the nozzle. The pressure was converted to velocity using Bernoulli's equation, area ratios, and correction coefficients from the work of Wilson (1970), which documents the use of this apparatus for hot-wire calibration.

A typical calibration curve obtained for this study using this apparatus is shown in Figure 3-9.

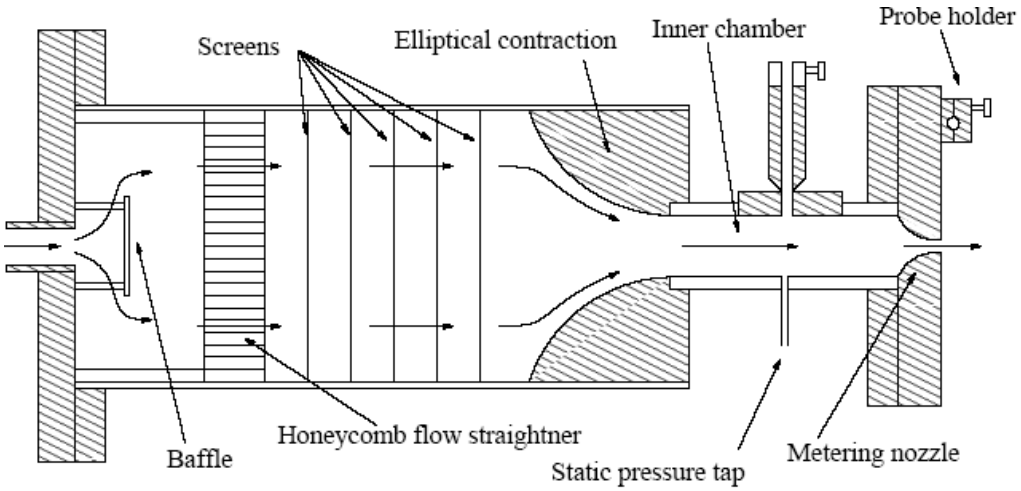

Figure 3-8 Hot-wire calibration apparatus (adapted from Adolfson, 2003)

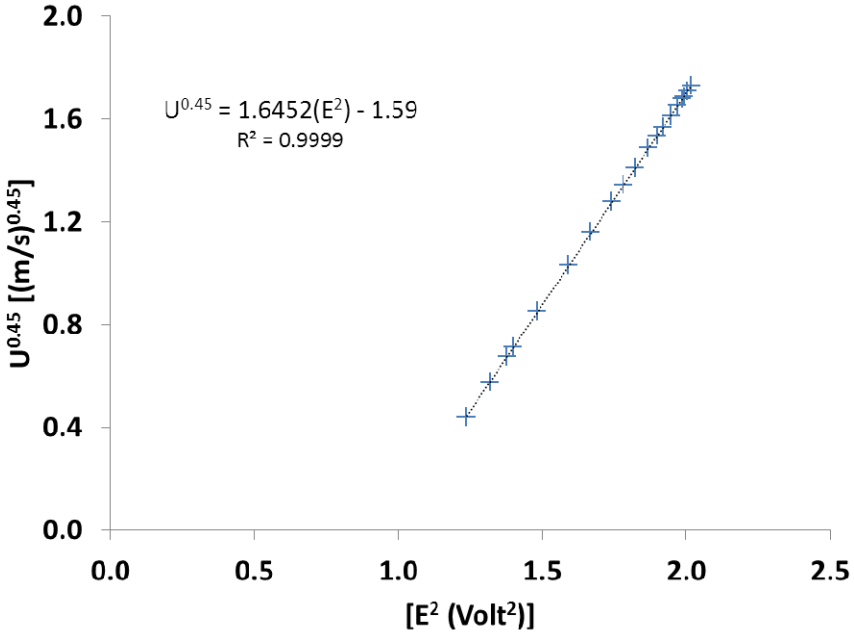

Figure 3-9 Hot-wire calibration curve obtained using the apparatus shown in Figure 3-8,

Corrections and uncertainty for hot-wire measurements

Based on standard error estimation techniques for thermal anemometry, the level of uncertainty in a single-point measurement of velocity is estimated to be less than 5%, with a 95% confidence interval. This agrees well with Volino and Simon (1995): 3% to 5%, and Kaszeta and Simon (2002): 4.7%.

This does not include measurements in reversed flows, or flows with high turbulence intensity. Hot-wire measurements in these situations can have high uncertainty, and are best considered to be good indicators of flow characteristics, rather than accurate velocity measurements.

Errors may be introduced in the near-wall region, and by temperature variations. Errors may also be introduced by two sources specific to this flow: possible local heating of the air by the plasma discharge, which may introduce temperature variations locally, as well as effects of the electric field of the plasma discharge introducing a current flow through the hot-wire. Estimates of the effect based on the literature are provided. However, the hot-wire data are processed using an algorithm to discard data segments acquired during the 60% fraction of pulse time that the plasma discharge is active.

The major conclusions drawn in this study about the separation control performance of the actuator are insensitive to the application of these corrections. For characterization flow separation and its control, the wall-normal gradient of the velocity is also found to be a reasonable parameter. Additionally, these measurements show good qualitative agreement with the total pressure measurements taken in the flow without wakes.

Near-wall corrections

Hot-wire measurements at locations very near the wall are affected by conduction heat transfer between the hot-wire sensor and the wall, introducing errors that produce indicated velocities that are too high.

While many studies (see, for example, (Chew et al., 1995)) are available that document near-wall corrections, the difficulty of accurately estimating wall shear stress and boundary layer thickness in the periodic unsteady wake flow make several of them infeasible.

The empirical near-wall correction scheme of Wills (1962) was developed for laminar flows (equations 7 and 8), with recommendations for use in turbulent flows. Modified forms of this scheme are widely used in the literature. Kim (1990) suggested that 84% of the Wills correction for near-wall correction of hot-wire measurements was suitable for turbulent boundary layers (equation 9). Volino and Simon (1995) used this modified 84% form of the Wills correction for all hot-wire measurements taken for a study on transitional boundary layers.

This modified form of the Wills near-wall correction (equation 9) was applied to hot-wire measurements for flow control with passing wakes in this study.

$$\underline{U}_{Wills} = [\, U_{uncorrected}^{0.45} - k_w.(v/2a)^{0.45} \,]^{1/0.45} \qquad (7)$$

where 'U' is velocity (m/s), 'a' is the radius of the hot-wire sensor, and 'v' is the kinematic viscosity of air at the nominal film temperature between the hot-wire and free-stream temperatures. 'k_w' is given by

$$k_w = 4.53.(y/a)^{-1.0278} \qquad \text{when } y/a < 40$$
$$k_w = 76.524.(y/a)^{-1.7893} \qquad \text{when } y/a \geq 40 \qquad (8)$$

where 'y' is the wall-normal distance in the same units as 'a'. For the present study, the hot-wire sensor radius a = 0.0019 mm, and $(v/2a)^{0.45}$ = 2.38. To reduce the risk of interference of dielectric surface charge with the hot-wire probe, the location nearest to

the wall attempted for the measurements with passing wakes was 0.1 mm away from the wall. At this closest location to the wall, $y/a \approx 53$.

$$U_{corrected} = 0.84.(U_{Wills}) + 0.16.(U_{uncorrected}) \quad (9)$$

The difference between applying the full Wills correction (equation 7) and 84% of the correction (equation 9) can be significant (as a percentage difference) for measurements taken within the "dead zone" of the separation bubble, at the closest reported wall-normal distance used in this study of 0.1 mm. Nevertheless, whether corrected via equation 7 or 9, or entirely uncorrected, these particular measurements can always be unambiguously distinguished as representing very low flow velocities.

In general, hot-wire measurements of very low velocity flows are useful for identifying regions of relatively stagnant fluid; the magnitude (and direction) of flow velocity cannot be measured accurately for these regions.

For all other flow conditions at $y = 0.1$ mm, the difference between using equation 7 or 9 for near-wall correction is found to be negligible, and below the uncertainty of the experiment. This statement also holds for all measurements for $y \geq 0.1$ mm, regardless of flow conditions.

Temperature corrections

The hot-wire output voltage is sensitive to the mass flux around it, and to the ambient temperature of the flow.

A first-order temperature correction scheme (Kaszeta, 1998) was used to correct for small temperature variations by multiplying the anemometer output voltage with the following correction factor.

$$C_f = \sqrt{\left(T_s - T_c\right) \Big/ \left(T_s - T_f\right)} \tag{10}$$

where T_s is the hot-wire sensor temperature (250 °C) in this study, T_c is the temperature of the flow jet used for calibration, and T_f is the local flow temperature during the measurement.

During calibration, an RTD temperature sensor was used to measure the temperature T_c of the calibration flow jet. An Omega HH311 handheld temperature meter was used to monitor the air temperature at a span-wise distance of about 0.5 m from the actuator. This temperature was logged at the start of measurements for each wall-normal location, a process which took about 20 minutes, and used as T_f in equation 10. Despite the thermostat-controlled air-conditioning in the laboratory, this temperature occasionally increased by as much as 0.5 °C between two consecutive measurements of this kind.

Also significant is the use of this temperature in lieu of the true local and time-varying temperature of the flow, which may incur slight heating due to the plasma discharge. AC DBD plasma actuators are generally considered to be non-thermal devices that produce insignificant ohmic heating (Ashpis and Thurman, 2011; Orlov, 2006; Sung et al., 2006; Enloe et al., 2004).

Jukes et al. (2006) provide an estimate of this temperature rise: they measured an air temperature rise of 2 °C at a 1 mm distance from the plasma discharge. In the present work, the most upstream measurement location for the study with wakes was located more than 30 mm away from the exposed electrode edge. Based on this, the local temperature rise due to ohmic heating is expected to be negligible.

Correction of electric field effects

In the present study, hot-wire anemometer signals taken with the actuator on during measurements in the flow with passing wakes show a significantly reduced amplitude.

Since the actuator was used in pulsed mode for this study, this reduction was observed during the active (or 'on') fraction of the pulsing cycle. A hot-wire probe placed in a gradient of electric field may experience an additional component of electric current due to this difference of electric field at the two ends of the wire. This is one possible explanation for this behavior. The extent of amplitude reduction was found to decrease with increasing distance from the wall, but the effect is significant even when the probe is moved out far enough to be outside the airfoil passage flow.

Figure 3-10 shows the trace of a sample velocity signal acquired by the hot-wire probe in the measurement field with passing wakes, with the actuator operating at the 80 Hz / 0.6 duty cycle pulsing conditions used in this study. The arrows mark the 60% time intervals where the electric signal driving the actuator was active. The smaller, unmarked intervals comprise the 40% of each cycle with the electric signal off. The dramatic change, and rate of change, at the beginning and end of the 'on' periods is evident in the figure.

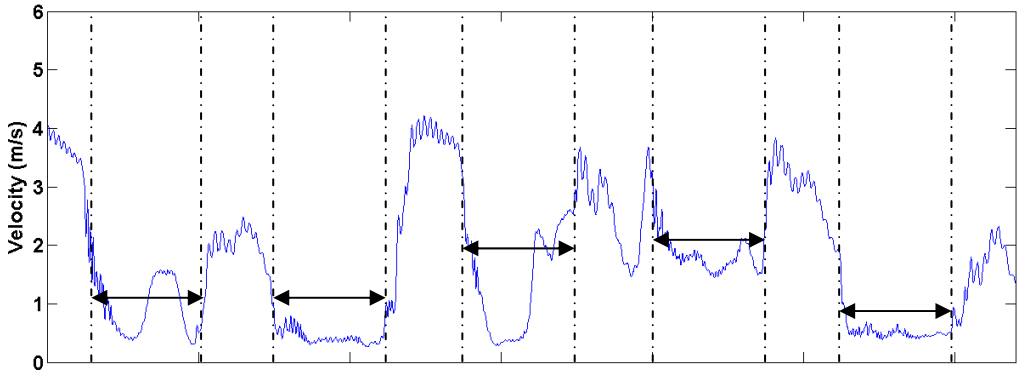

Figure 3-10 Sample trace of acquired velocity data showing the significant drop in signal amplitude during the 'on' 60% of the pulsing cycle (marked with arrows).

Based on data from this study, the anemometer is estimated to take between 0.1 and 0.2 milliseconds to respond to a change of actuator state, which is about 1% of the 80 Hz pulsing interval.

To the best of this author's knowledge, there is no information on corrections to instantaneous velocity due to errors in the electric field generated by the discharge. Similar to the work of Jukes et al. (2008), all hot-wire data in this study that were taken with the actuator on were processed to discard the signal segments taken during 60% of the pulsing cycle that had the plasma discharge active. An algorithm was written to identify and eliminate these signal segments. The algorithm was based on locating a reliable specimen of sudden voltage drop associated with the activation of the plasma discharge in the signal trace. To distinguish this voltage drop from the smaller magnitudes associated with fluctuations of the fluid flow, threshold levels for a criterion function were determined empirically using data from a broad range of wall-normal and stream-wise measurement locations from this study. Once a reliable specimen of a falling-edge voltage was identified in a measurement file, indexing the remaining 'on' and 'off' periods was done by stepping through the appropriate intervals of data points, based on the values of sampling rate and time scales of pulsing.

The correct working of the algorithm was manually verified for a very large number of data sets from measurements at the full range of wall-normal distances and stream-wise locations used in this study.

The above discussion identifies two possible sources of error for the hot-wire measurements in this study:

a) The possibility of rise in local air flow temperature due to ohmic heating by the plasma discharge. As discussed, based on the literature, this is expected to be ~2 °C in the very near (1 mm) vicinity of the discharge. The most upstream measurement location for the study with wakes was located more than 30 mm away from the exposed electrode edge.

b) A strong reduction in the anemometer output voltage during active periods of plasma discharge operation. As discussed, the segments of the hot-wire signal taken during these periods were processed and discarded.

Both errors tend to under-predict velocity, i.e., they lead to conservative results. Additionally, the wall-normal gradient of velocity is used to interpret measurements, which is a reasonable and robust parameter for characterizing flow separation control.

4. Preliminary experimental characterization

In this chapter, several preliminary studies that assess various aspects of the performance of the plasma actuator for flow control are discussed. All flow measurements in this chapter were total pressure measurements, taken with a glass pressure tube. Details of the instruments and experimental methods used can be found in Section 3.2.

The effect on the flow of varying the pulsing frequency and duty cycle of the actuator's input signal is investigated. Flow control is demonstrated with the actuator imparting momentum opposite to the stream-wise flow direction, showing that it is possible to use disturbances alone to destabilize the flow, without momentum addition near the wall. Edge effects and span-wise variation of the actuator discharge are also investigated.

4.1. Effect of varying pulsing frequency and duty cycle

To examine the effect of variation of pulsing frequency and duty cycle on the flow, measurements of total pressure were taken at a fixed point in space, at a location (s/L_{ss} ~ 0.76; 1.5 mm from the wall) where the separated flow responds strongly to disturbances. (These measurements were taken before the glass dielectric was designed - see Appendix – Dielectric selection for the plasma actuator for details). It was necessary to use two layers of PET polyester bonded together as a dielectric. This thicker dielectric allowed longer operation at the high duty cycles and frequencies of interest before burning out due to oxygen attack on the polyester. Close attention was paid to the difference in measured total pressure between the 'off'' case and the lowest duty cycles. In every case, multiple randomized measurements were taken in order to check for repeatability, especially over parameter ranges where strong unsteadiness was observed. Table 4-1 summarizes the experimental parameters for this study.

Table 4-1 Experimental parameters for study on variation of pulsing frequency and duty cycle

Airfoil	Pack-B
Reynolds No. (exit vel. and suction surface length)	50,000
Inlet flow turbulence intensity	2.5%
Location of actuator (downstream edge of exposed electrode, s/L_{ss})	0.49
Total pressure tube O.D.	1 mm
Dielectric material	PET polyester
Dielectric thickness	2 x 0.25 mm
Electrode material	Copper (tape)
Embedded electrode width	20 mm
Exposed electrode width	6.4 mm
Exposed electrode thickness	0.08 mm
Actuator electrical signal type	AC, sine, 600 Hz, 16 kV_{p-p}
Signal pulsing characteristics	0-85 Hz, 0-100% duty cycle

Figure 4-1 shows the effects of varying duty cycle with a sine wave of fixed amplitude and frequency (16 kV_{p-p}, 600 Hz) applied to the actuator, and with the frequency of pulsation held constant at 10 Hz. In Figure 4-1 and Figure 4-2, values that are tending toward the negative y-axis direction indicate higher total pressures, indicating more separation control authority and reduced separation bubble sizes.

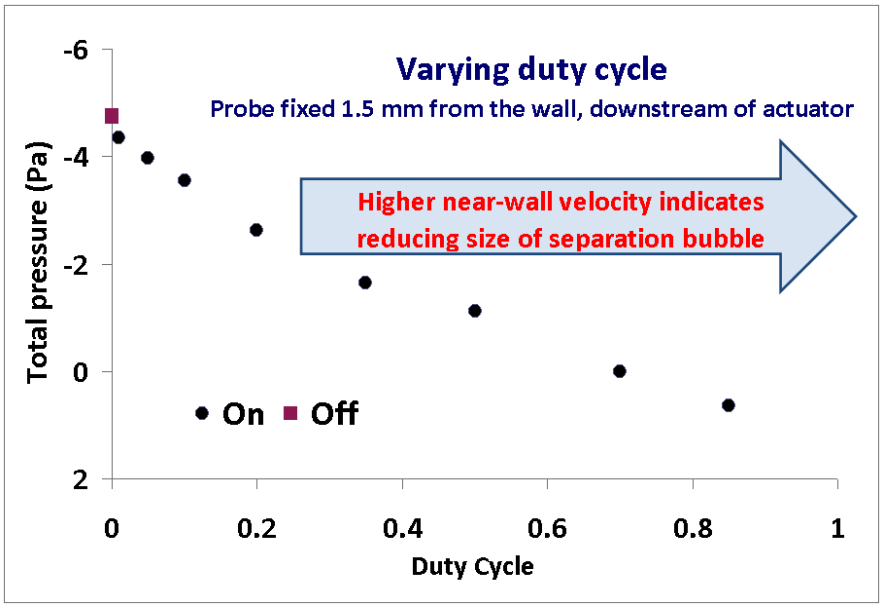

Figure 4-1 Variation of total pressure with duty cycle. Probe is fixed at s/L_{ss} ~ 0.76, at a distance 1.5 mm from the wall.

At low duty cycles, such as less than about 0.3, total pressure level measurements taken with the micro-manometer are steady (indicating steady flow, or flow fluctuations of a higher frequency of variation than can be resolved by the manometer), and highly repeatable. As the duty cycle is increased beyond this, past about 0.5, the total pressure increases. From previous work, it is known that re-attached boundary layers show higher near-wall total pressures than those of separated flows; it is therefore speculated that this trend of increasing total pressure is a tendency toward reduced separation bubble size or toward re-attachment. At these values of duty cycle, distinct unsteadiness is observed, with a characteristic time period of about 1-2 seconds. An incipient re-attaching flow is relatively unsteady compared to a fully separated flow, so this strengthens the speculation that the high total pressures indicate near-reattachment. In taking these measurements, the micro-manometer's screw gauge is set to progressively higher pressures, and time is allowed for the unsteady total pressure to raise the manometer meniscus to this level and deflect an indicator, if the set level is reached. The highest such pressure is recorded. While unsteady, these measurements are highly repeatable when taken in this manner for these intermediate duty cycles (above 0.5) where the unsteadiness is present.

Beyond a duty cycle of 0.8, the measurements are no longer repeatable, especially if the experiment is conducted continuously for extended periods of time. It is possible that this is related to heating, or effects related to the actuator other than flow behavior. Measurements were taken at duty cycles extending to 0.9999, and the general trend observed in Figure 4-1 was continued to this value, though the measurements over the duty cycle range from 0.85 to 0.9999 were of increasingly poor repeatability.

Since the authority being asserted over the separation zone is ostensibly due to perturbing the separated shear layer and inducing early transition and re-attachment, rather than by adding momentum (this aspect will be discussed further in this chapter), it is suggested that increasing the duty cycle (or thrust per pulse) will generally not be beneficial once the separation bubble has fully re-attached. It is difficult to compute the

expected value of total pressure of a fully attached flow at this location, especially considering the complex history of the flow upstream of it. Thus, the fully-attached value of total pressure under these conditions is unknown.

Figure 4-2 shows the effect of varying frequency of pulsation with a fixed amplitude and frequency (16 kV_{p-p}, 600 Hz) sine wave applied to the actuator, and with the duty cycle held constant at 0.2 (i.e., 20%). The measurements and results will be discussed in two parts:

a) *Frequencies of pulsation greater than about 10 Hz*: Comparing this case to Figure 4-1, it can be seen that the curve is very similar in nature to that observed for a varying duty cycle. The nature of the measurements is also similar: steady (or with a frequency much higher than the time resolution of the micro-manometer), highly repeatable (at frequencies between about 10 and 50 Hz), and showing distinct unsteadiness at frequencies higher than that range. The run-to-run repeatability becomes poorer at frequencies beyond about 90 Hz.

b) *Frequencies of pulsation less than about 10 Hz*: These data seem to imply an increasing effect on separation control at very low frequencies of pulsation. However, the micro-manometer is unfortunately not a suitable instrument to measurement changes over the activation and relaxation time periods. Closer examination of the data suggests that at these low frequencies, the micro-manometer used is increasingly able to resolve the 'on' and 'off' portions of each cycle of intermittent pulsation, and at the lowest frequencies, the measurements taken show total pressure varying from a value corresponding to fully 'off' actuator for the inactive portion of the duty cycle, to one corresponding to a fully (or with unity duty cycle) 'on' during the active portion. Only the measurements taken during the 'on' part of the cycle are plotted here (Figure 4-2). The decreasing total pressure trend observed at frequencies of pulsation greater than 10 Hz plateaus as the frequency decreases and the micro-manometer begins to resolve the different, 'on' and

'off,' components of each pulse. The total pressure appears to increase at lower frequencies, but is actually fluctuating between the plotted value, and the 'off' value.

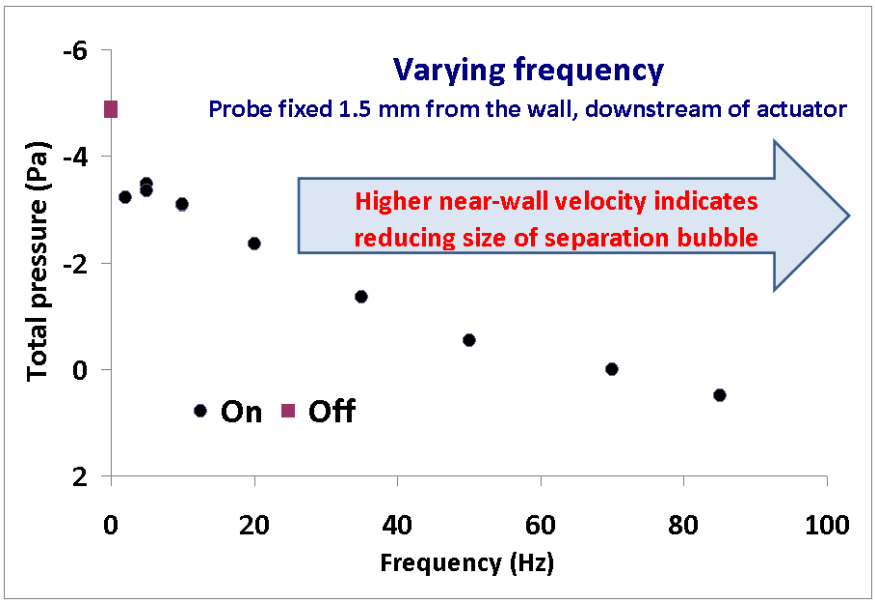

Figure 4-2 Variation of total pressure with pulsing frequency. Probe is fixed at $s/L_{ss} \sim 0.76$, at a distance 1.5 mm from the wall.

These results show that increasing control authority is available at higher pulsing frequencies and duty cycles (presumably until re-attachment occurs), and no specific frequency or frequency band in the tested range excites a resonant response from the separated flow.

All the results that will be discussed subsequently in this chapter are from measurements taken for a fixed pulsing frequency of 10 Hz, duty cycle of 20%, with an excitation AC sine wave at 16 kV_{p-p} and 600 Hz, shown as a schematic in Figure 4-3. These fairly modest values were selected despite knowing that considerably higher authority is available by increasing any of these values, as demonstrated above, because of the tendency of the PET polyester dielectric to burn out rapidly. Consequently, it should be noted that the upcoming results are not approaching the best control that is

available. Actuators made out of more durable dielectrics will be discussed subsequently. Table 4-2 summarizes the experimental parameters for the remaining studies.

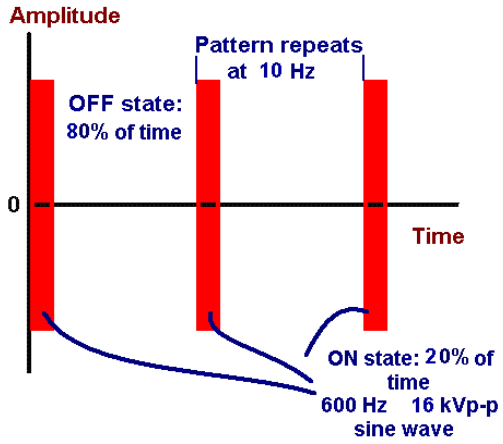

Figure 4-3 Schematic of the intermittent actuation timing for studies on actuator orientation and edge effects, Figure 4-4 to Figure 4-14

Table 4-2 Experimental parameters for studies on actuator orientation and edge effects, Figure 4-4 to Figure 4-14

Airfoil	Pack-B
Reynolds No. (exit vel. and suction surface length)	50,000
Inlet flow turbulence intensity	2.5%
Location of actuator (downstream edge of exposed electrode, s/L_{ss})	0.49
Total pressure tube O.D.	1 mm
Dielectric material	PET polyester
Dielectric thickness	0.25 mm
Electrode material	Copper (tape)
Embedded electrode width	20 mm
Exposed electrode width	6.4 mm
Exposed electrode thickness	0.08 mm
Actuator electrical signal characteristics	AC, sine, 600 Hz, 16 kV_{p-p}
Signal pulsing characteristics	10 Hz, 20% duty cycle

4.2. Effect of aligned and reversed actuator orientation

In order to examine the relative effects on separation control of momentum addition near the wall and on effecting flow disturbances, the actuator was turned around so that it

was oriented in a reversed fashion with the exposed electrode downstream of the embedded electrode. The actuator in this configuration therefore adds momentum in the direction opposite to the mean flow.

Figure 4-4 shows the total pressure profiles taken at two locations downstream of the reversed actuator. The exposed electrode edge was located at $s/L_{ss} \sim 0.49$, where it is fixed for all the airfoil studies in this document. As the plots show, the actuator has a pronounced effect on the flow far downstream of the discharge (bottom plot), while having negligible effect more immediately downstream of it (top plot). This suggests that flow control authority is available predominantly by flow disturbance.

Profiles such as those shown in Figure 4-4 were taken at five stream-wise locations in the trailing part of the airfoil suction surface, with the actuator reversed, as discussed above, and aligned with the flow, in which configuration it imparts momentum in the direction of the mean flow.

Figure 4-5 shows a field of the wall-normal gradient of total pressure on a stream-wise/wall-normal plane at the trailing part of the airfoil. Red zones indicate strong shear; blue zones indicate the lack of shear. The red area in the bottom left corner of each plot is the wall boundary layer, in a state of incipient separation. The red and yellow arc starting at this boundary layer and curving over the trailing part of the flow field represents the separated shear layer. The blue zone above the shear layer is the free-stream, with relatively little change in total pressure in the wall-normal direction. The near-wall blue zone under the shear layer is the “dead” fluid in the separation zone, also with little change in total pressure.

The top two plots in Figure 4-5 are ostensibly the same case, since these measurements were taken with the actuator off. Some variation between these two plots is observed near the trailing edge. Reattachment locations are known to vary in time and

space, and these differences are indicative of case-to-case variations when different actuators are mounted.

Comparing the ‘on’ cases (bottom of each set) to their respective ‘off’ cases (top of each set) shows a much reduced dark-blue zone under the shear layer for the aligned case, and the layer itself is more diffuse as it develops in the stream-wise direction. These light-blue/green/yellow values in the more diffuse regions are likely due to unsteady re-attachment, which is time-averaged by the micro-manometer.

The ‘on’ aligned case (bottom, right) apparently shows a stronger effect for s/L_{ss} ~ 0.75, when compared to the ‘on’ reversed case (bottom, left). The following observations are made:

a) the boundary layer before separation for the reversed ‘on’ case is thicker, relative to the aligned ‘on’ case;

b) the wall-normal distance of the shear layer (the high dP_0/dy layer) at this stream-wise location of s/L_{ss} ~ 0.75 seems to be about the same for the aligned and reversed ‘on’ cases.

Given these observations, the reduction of the near-wall dark blue zone at s/L_{ss} ~ 0.75 for the aligned case appears to be a consequence of stronger entrainment by the more intense shear layer formed from the thinner boundary layer (approaching separation) that is observed in this case. The reversed actuator produces a thicker boundary layer and a downstream shear layer (after separation) that entrains less flow, as expected.

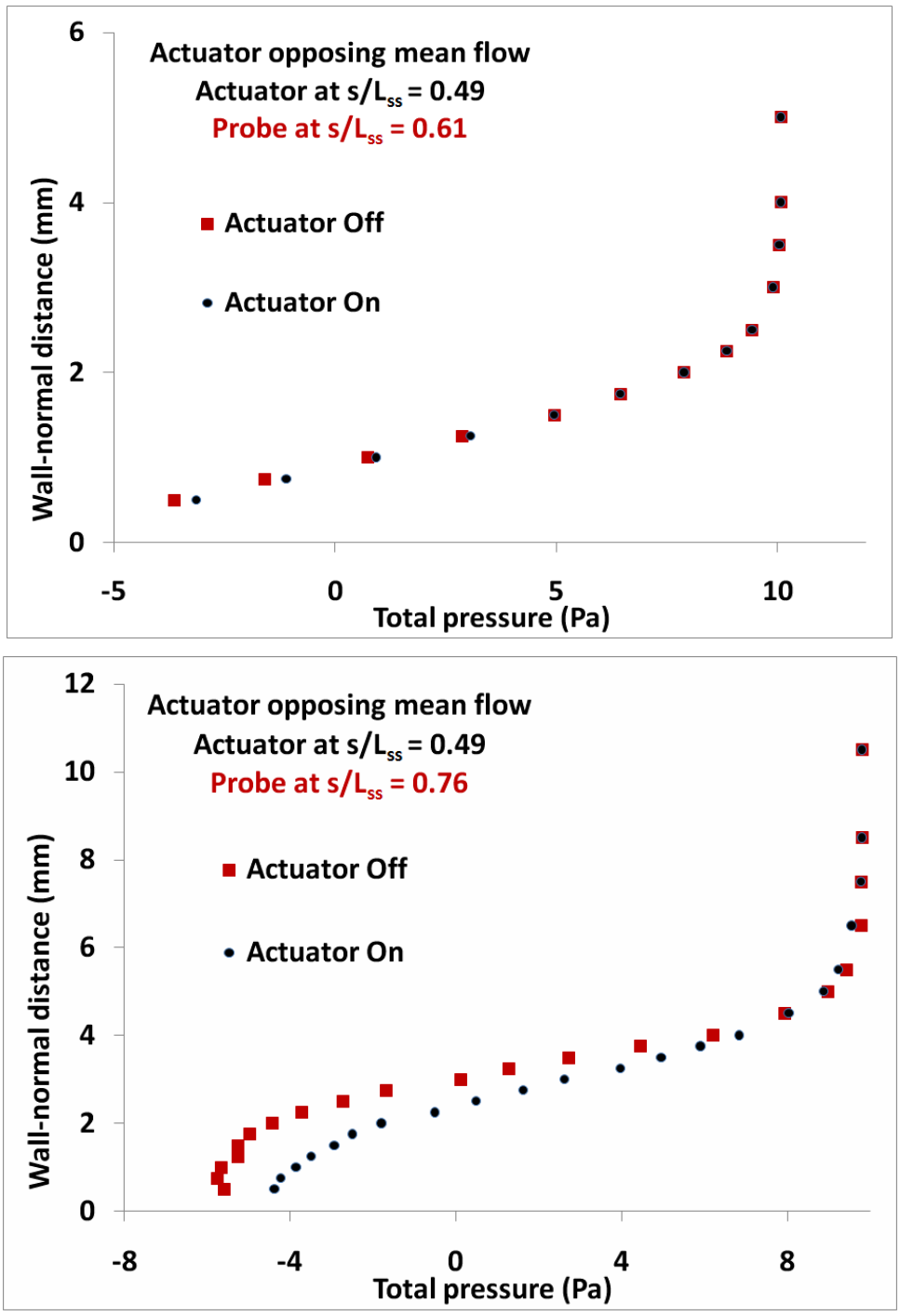

Figure 4-4 With the actuator oriented to add momentum in a direction opposite to the mean flow, more activity due to the actuator is observed far downstream (bottom) than closer to the actuator (top).

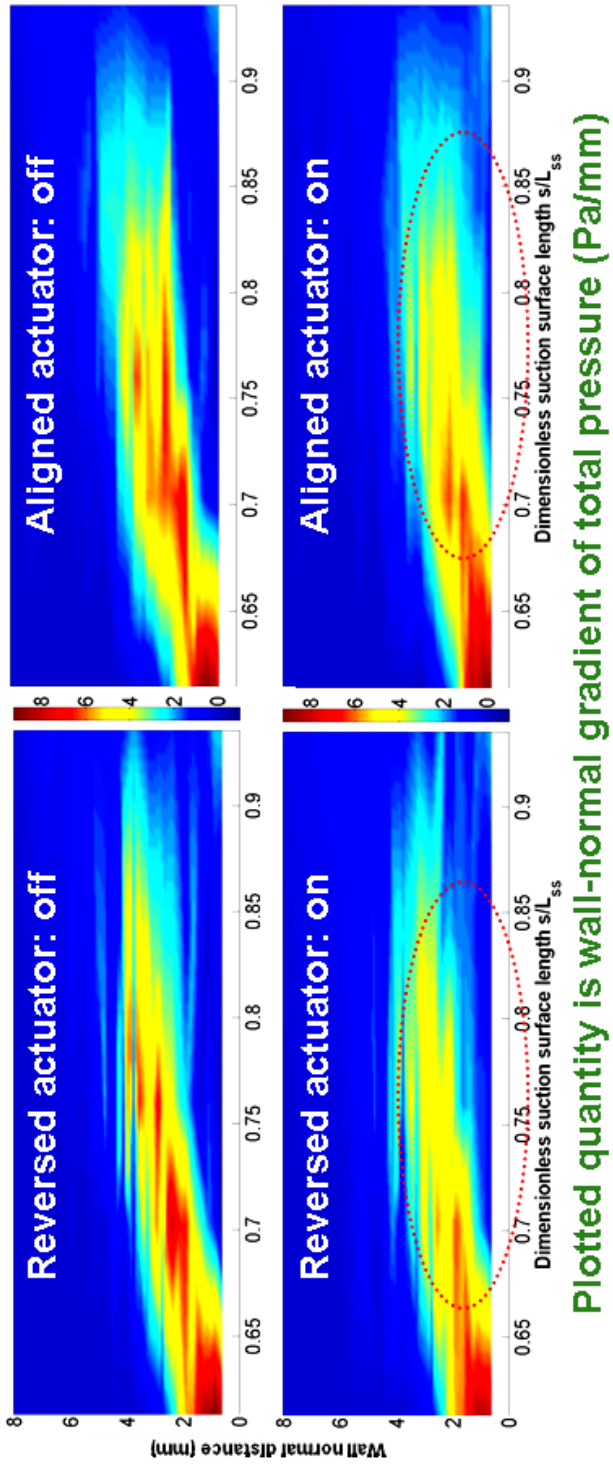

Figure 4-5 Wall-normal gradient of total pressure is used to show the flow field in the trailing part of airfoil passage, with the actuator 'on' and 'off', when oriented in a reversed and aligned manner.

Figure 4-6 shows the effect of the actuator on the total pressure field for the reversed actuator case. The plotted quantity is the local difference in the total pressure between the 'on' and 'off' cases, in Pa. The red spot marks the zone of maximum change induced by the actuator, likely indicating where transition onset occurs in the shear layer. Figure 4-7 is an identical plot, but for the aligned actuator. In the aligned case, transition occurs at a more upstream location, and the effect of the actuator extends to the wall before fading away farther downstream.

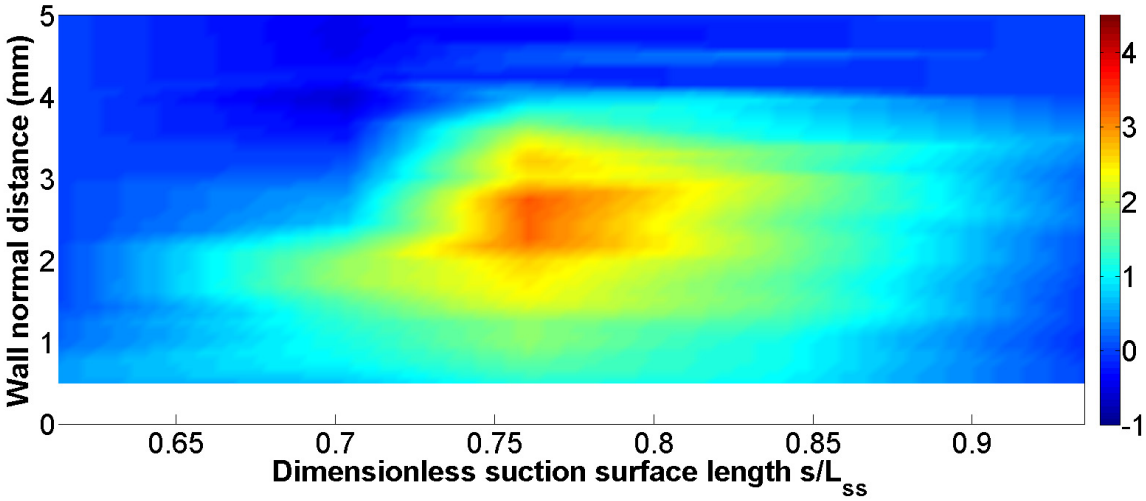

Figure 4-6 The difference of total pressure (Pa) between the 'on' and 'off' cases, for the actuator in the reversed orientation.

It can be speculated that the critical stream-wise location for transition in the separated shear layer is determined by the strength of the shear and the thickness of the shear layer. In the case of the aligned actuator, the boundary layer at incipient separation is seen to be thinner, producing a separated layer with stronger shear. A comparison of Figure 4-6 and Figure 4-7 can be interpreted as follows: the stronger shear for the aligned actuator leads to transition for that case at a location that is upstream of the transition location observed for the reversed case. The reversed actuator case has a thicker separating boundary layer producing a separated shear layer with lower shear strength. This layer continues to thicken in the downstream direction until it becomes unstable, ultimately transitioning to

turbulence. Both cases show a more upstream transition with the actuators ‘on’ relative to the ‘off’ case, indicating the importance of the disturbance introduced by the actuator.

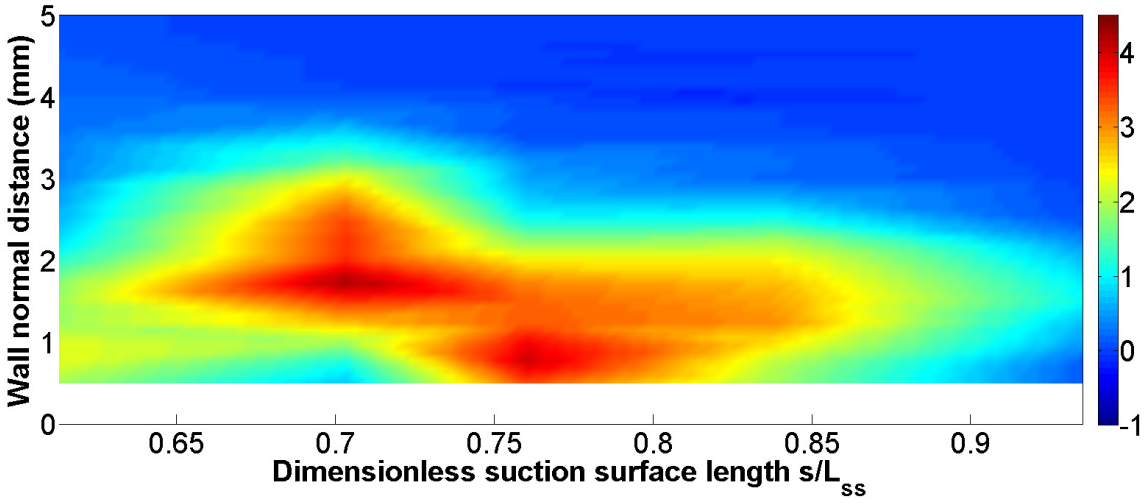

Figure 4-7 The difference of total pressure (Pa) between the ‘on’ and ‘off’ cases, for the actuator in the aligned orientation.

4.3. Span-wise variation and edge effects

The results presented in Sections 4.1 and 4.2 relate to measurements taken at a single span-wise location, which was near the actuator center-span, well away from the edges of the discharge. The study discussed in this section was motivated by an interest in examining if span-wise variations would lead to more upstream transition, and to verify that data obtained previously were free of actuator edge effects. As the results in this section will show, much higher authority is available near the edges

In order to examine if the separated shear layer responds to three-dimensionality in the form of stream-wise and wall-normal vorticity embedded into the attached boundary layer shortly before it separates, a study of span-wise variation of the flow field downstream of the edge of the lower (embedded) electrode of the actuator was conducted. In this region, total pressure measurements were taken on three planes

separated from one-another in the wall-normal direction, at five stream-wise locations and nine span-wise distances.

Figure 4-8 shows a schematic that explains the orientation of the remaining plots in this section. Three planes of constant distance from the wall are plotted, with the zero on the y-axis representing the edge of the actuator, and positive values being the discharge side of the edge. The x-axis is the stream-wise direction. The downstream edge of the exposed electrode of the actuator is at $s/L_{ss} \sim 0.49$, considerably upstream of the plotted range. Measurements are taken at the stream-wise locations that show separation of the boundary layer, and transition.

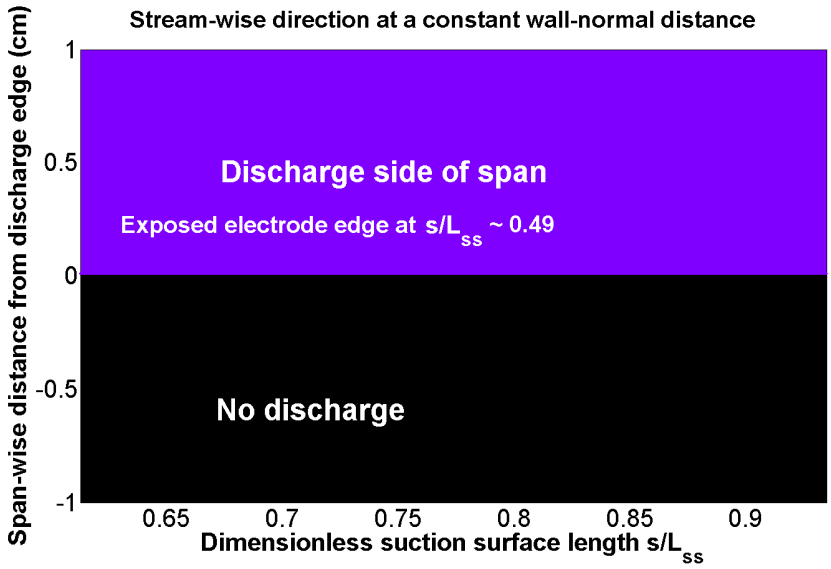

Figure 4-8 Schematic showing the topography of the study of span-wise variation.

Figure 4-9 shows the plane nearest to the wall, at a wall-normal distance of 0.5 mm. The plotted quantity is the difference between total pressures, in Pa, with the actuator 'on' and with the actuator 'off'. Figure 4-10 shows the individual 'on' and 'off' total pressure plots that produced this total pressure difference plot. The 'off' case shows the flow to be quite two-dimensional, with the expected spatial fluctuations in the re-attachment zone near the trailing edge. Both Figure 4-9 and Figure 4-10 make it clear that

the zone of influence of the actuator in this near-wall plane is where the edge intersects $s/L_{ss} \sim 0.75$. Compared to the effects we will see on the other two planes, this influence is rather weak.

Figure 4-11 shows data taken on a plane 1.5 mm away from the wall. Of the planes under consideration, this is the plane that shows the strongest effects of the actuator. It is evident that the presence of the actuator edge makes a sizable difference to the effectiveness of the actuator. The effect of the actuator fades away farther downstream of the red zone (where the edge intersects $s/L_{ss} \sim 0.75$). It is possible that a more effective actuator would extend the zone of the activity farther downstream. Figure 4-12 shows the individual 'on' and 'off' plots for this plane. Again, the 'off' case is quite two-dimensional, while the 'on' case shows a distinctly stronger effect near the edge. It is also interesting to note the dark blue zone in the no-discharge zone near the edge (lower left corner of Figure 4-11), where the total pressure actually drops when the actuator is turned on.

Figure 4-13 shows the plane farthest from the wall, with a wall-normal distance of 2.5 mm. The strong effect of the actuator of the previous plane has reduced somewhat, although is still quite prominent. The individual 'on' and 'off' plots in Figure 4-14 show similar trends to those of the previous plots, with the region aligned with the edge of the electrode again showing noticeably stronger changes due to the actuator. Unexpectedly, the 'off' case seems to show a small non-uniformity near the edge, also. It may be speculated that the presence of a physically protruding edge in the flow may be causing this. However, as has been mentioned before, the edge was that of the embedded electrode and the exposed electrode extends well beyond this location, so there is no surface feature of note at that location.

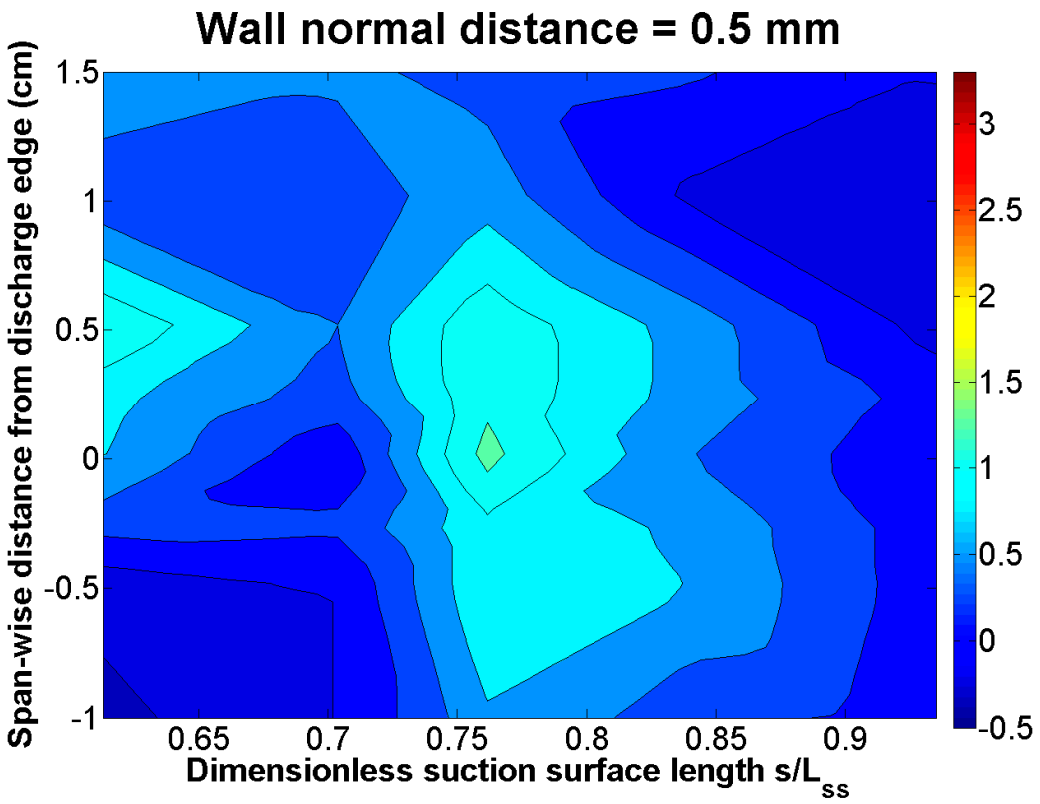

Figure 4-9 Difference of total pressure, in Pa, with the aligned actuator, between the 'on' and 'off' cases, at a wall-normal distance of 0.5 mm.

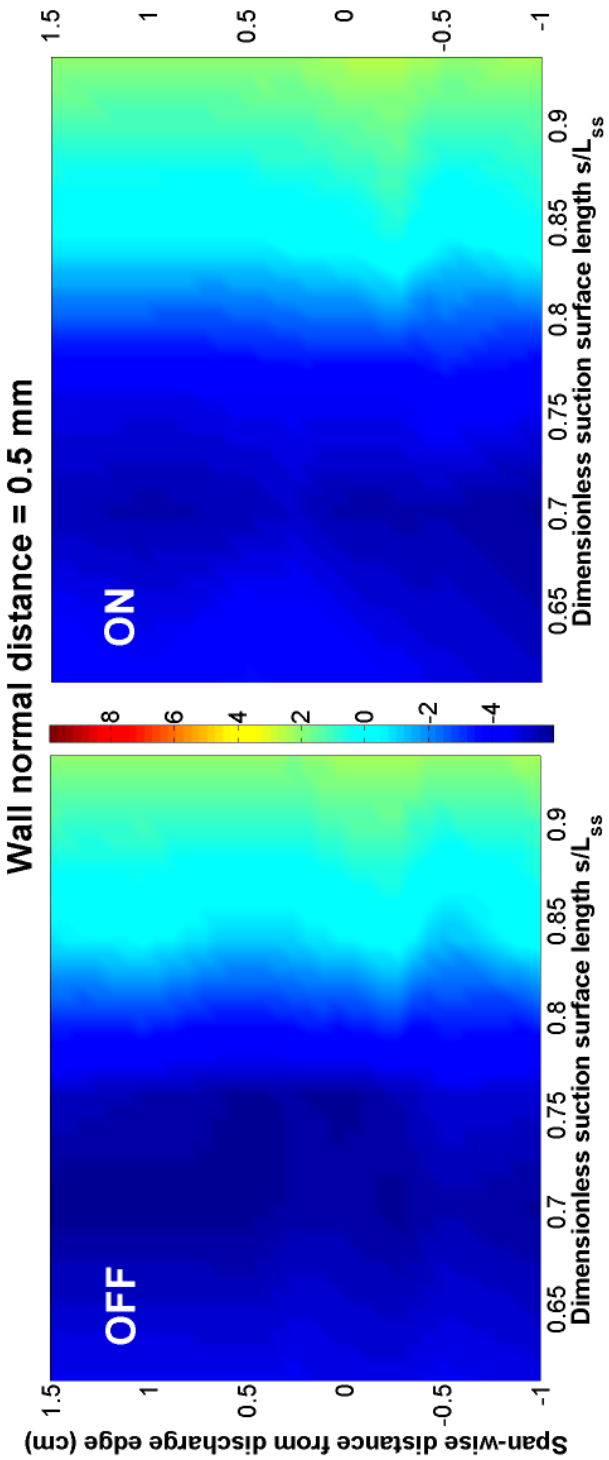

Figure 4-10 Total pressure field (Pa) in trailing part of airfoil passage, with the aligned actuator 'off' and 'on', in a plane at a distance of 0.5 mm from the wall.

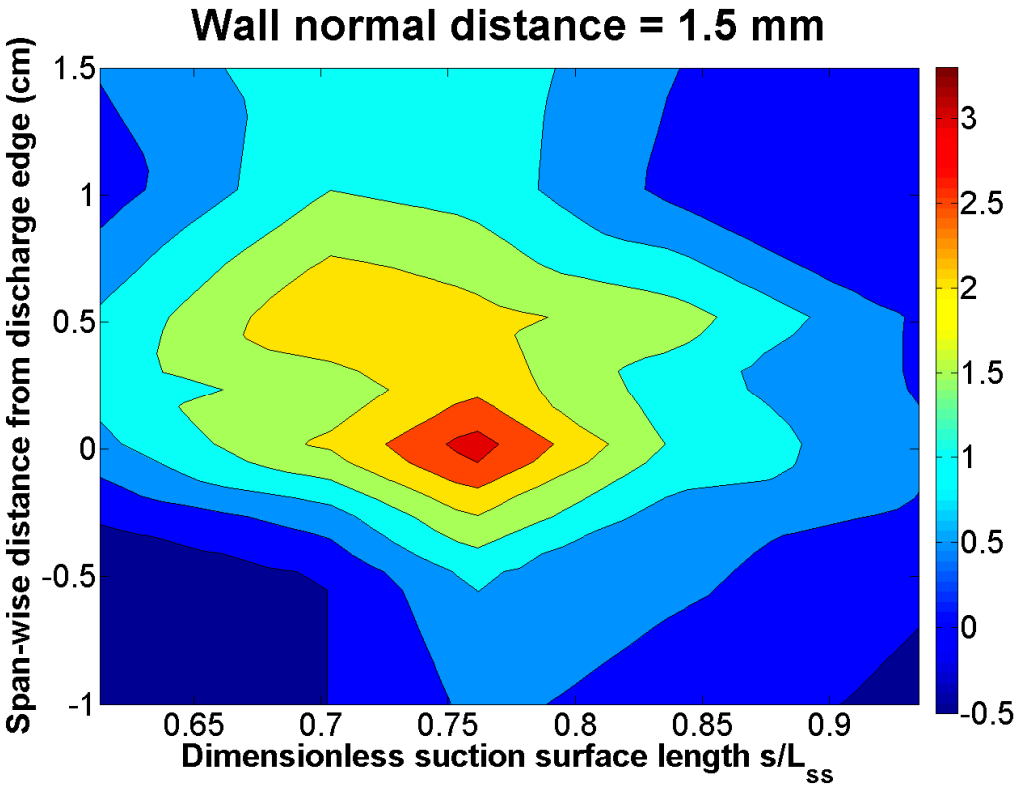

Figure 4-11 Difference of total pressure, in Pa, with the aligned actuator, between the 'on' and 'off' cases, at a wall-normal distance of 1.5 mm.

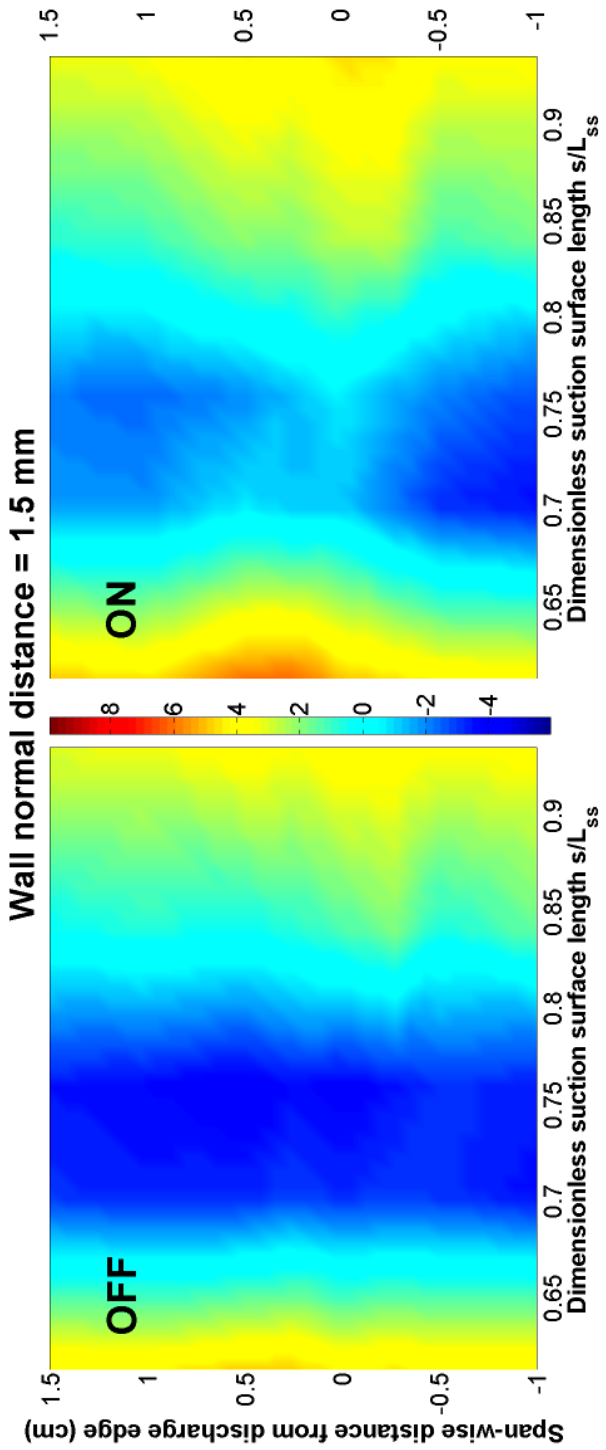

Figure 4-12 Total pressure field (Pa) in trailing part of airfoil passage, with the aligned actuator 'off' and 'on', in a plane at a distance of 1.5 mm from the wall.

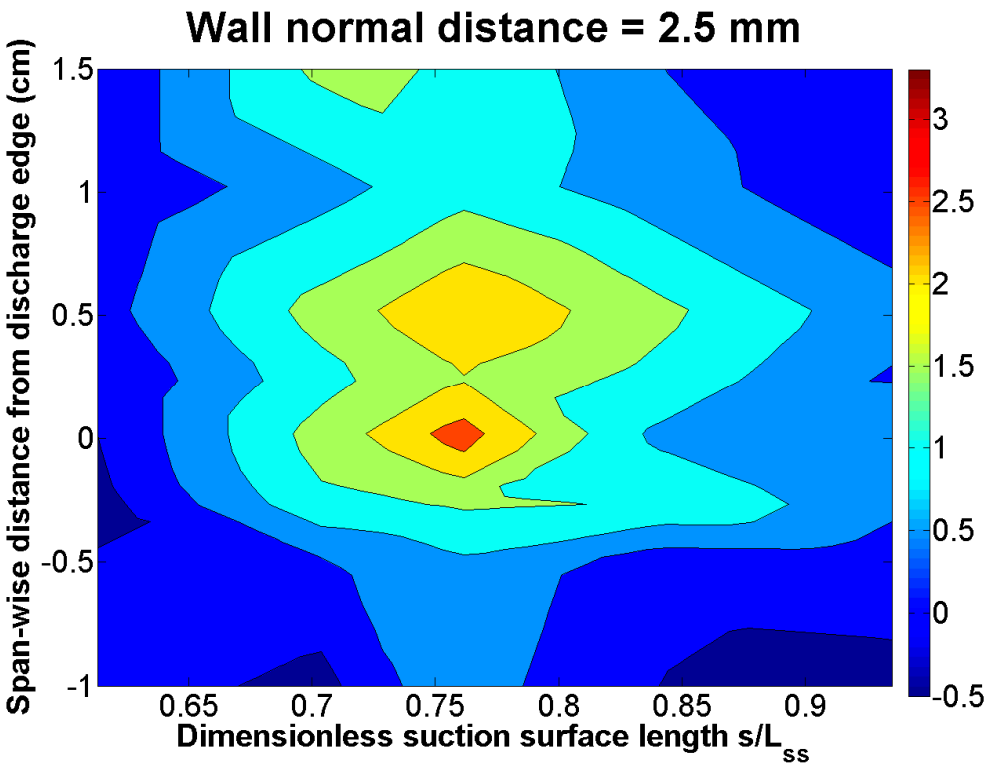

Figure 4-13 Difference of total pressure, in Pa, with the aligned actuator, between the 'on' and 'off' cases, at a wall-normal distance of 2.5 mm.

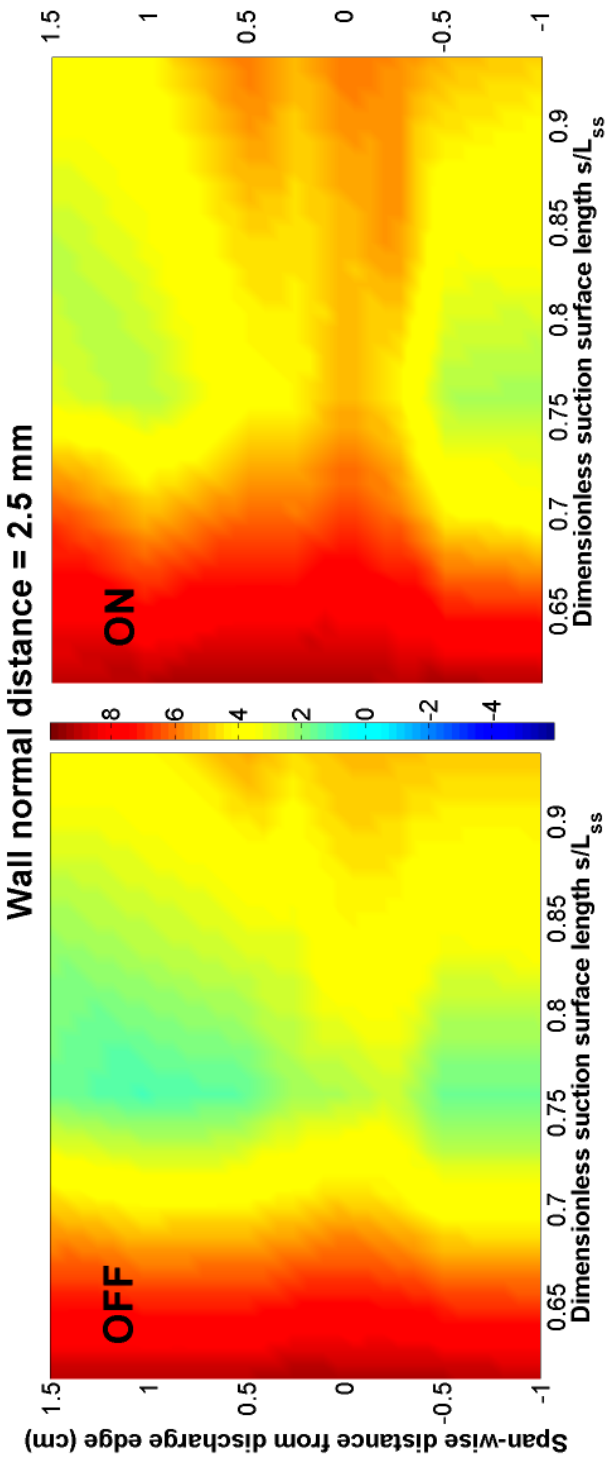

Figure 4-14 Total pressure field (Pa) in trailing part of airfoil passage, with the aligned actuator 'off' and 'on', in a plane at a distance of 2.5 mm from the wall.

Summary

Several preliminary studies on actuator performance for flow control were discussed in this chapter.

Momentum induced in quiescent air was found to scale with increasing excitation frequency and amplitude. For intermittent operation of the actuator in the turbine airfoil facility, the extent of separation control authority monotonically increased with increasing pulsing frequency and duty cycle, with no obvious resonant frequencies or frequency bands observed in the range tested, suggesting a broad band of effective (low) frequencies, as expected for bypass transition.

The actuator was operated in a reversed orientation to successfully demonstrate separation control, suggesting that at least part of the control authority is due to disturbances destabilizing the separated laminar shear layer alone, rather than by near-wall momentum addition. Further comparison of the control due to a reversed actuator with an aligned one shows that the latter is more effective for flow control, possibly due to the higher shear strength in the thinner boundary layer that it produces, relative to the reversed actuator, and that higher shear leads to more upstream transition.

A study of the edge effects of the plasma discharge, undertaken to investigate the role of span-wise flow variation on stream-wise transition location as well as to assess the two-dimensionality of the remaining flow field, demonstrated that considerably higher separation control authority is available near the edges.

5. Steady flow results

In this chapter, characterization of flow separation control by the DBD plasma actuator in the Pack-B airfoil passage without upstream wakes is presented.

All flow measurements discussed in this chapter were total pressure measurements that were taken with a glass pressure tube. Details of the instruments and experimental methods used can be found in Section 3.2. The actuator used for the measurements discussed in this chapter was fabricated using a 1.3 mm thick glass dielectric.

For this study, the actuator was powered using a conventional two-electrode geometry, as well as a more novel three-electrode geometry. The physics of the superior flow control performance of the latter geometry is discussed.

5.1. Actuator construction, configuration, and operating parameters

A 1.3 mm (0.050 inch) thick glass sheet was chosen as the dielectric material for the measurements in this chapter. Relative to previous measurements taken using polymer-based dielectrics, it permitted higher signal parameters to be used without actuator failure due to oxidation attack and burn-through. The glass sheet was slumped over a mandrel in an oven to conform to the shape of the Pack-B suction surface profile, and flush-mounted in a recess machined on the suction surface of the airfoil. Further discussion of the selection and fabrication of the dielectric can be found in Appendix – Dielectric selection for the plasma actuator.

A configuration with three electrodes, shown in Figure 4-16, instead of the conventional two electrode geometry was employed in order to study if the actuator geometry influenced flow control. This configuration was designed by Song Guo, a

researcher in the author's group. The operation and performance of this configuration is discussed alongside the flow results, later in this chapter.

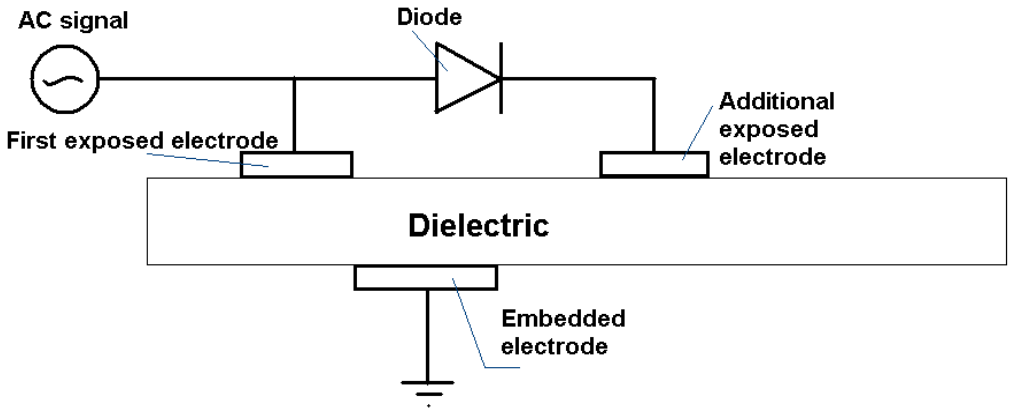

Figure 5-1 Schematic showing the actuator arrangement for the three-electrode geometry.

For the steady flow measurements (this chapter), as well as for the measurements with wakes (Chapter 6), the actuator was driven by a 14.7 kV_{p-p} 9 kHz AC sine wave, pulsed at 80 Hz with a 60% duty cycle. The downstream edge of the first electrode is at a non-dimensional stream-wise distance s/L_{ss} = 0.49. Measurement of total pressure profiles is made at five stream-wise stations, having s/L_{ss} = 0.55, 0.61, 0.70, 0.76, and 0.84. A comparison was made between the case with the actuator not activated, the traditional two-electrode geometry, and the three-electrode geometry.

5.2. Results and discussion

Figure 5-2 shows the plot of total pressure in the trailing part of the suction surface of the Pack-B airfoil. The top figure shows the field with the actuator off, i.e., it is the base case for the chosen Reynolds number and inlet turbulence intensity. The separation of the laminar wall layer is seen at the extreme left of the plot. The separated layer continues to leave the wall until transition to turbulence occurs, after which the enhanced transport of momentum produces growth of the separated shear layer and shrinking of the separation zone. Re-attachment occurs farther downstream than the right edge of the plot, very near the trailing edge of the airfoil.

The middle plot of Figure 5-2 shows the total pressure field when the two-electrode geometry actuator is activated. The third electrode is present in this case, but not electrically connected. The boundary layer continues to thicken, but separation is not evident in the figure. It is possible that a small separation bubble exists below the field of measurement. The high total pressure zone, seen near the left edge of the middle plot in dark red 2 mm away from the wall, is a region of accelerated flow produced when the actuator's zone of influence is encountered by the free-stream as a "virtual bump". Note that this high momentum region is not actually at the wall and is in fact above the shear layer, i.e., it is not directly increasing the wall shear stress by adding momentum to the near-wall flow to delay separation. It is expected that early transition due to the pulsed disturbance added to the shear layer by the actuator is primarily responsible for the absence of separation (or the very thin separation zone).

The three-electrode geometry produces a stronger zone of high momentum than the two-electrode case, with peak velocities higher than those of the free-stream, as shown in the bottom plot of Figure 5-2. It produces a thinner attached boundary layer over the suction surface than that for the two-electrode configuration (or a very thin separation zone).

The mechanism for the greater thrust due to an active third electrode may be explained as follows. The potential due to the third electrode helps to re-distribute the surface charge (that accumulates on the dielectric) toward the downstream direction. The modified electric field lines lead to increased acceleration of charged particles in the stream-wise direction, which transfer this additional momentum to the neutral air molecules by collisions (Guo, 2010).

Based upon an understanding of the first electrode inducing flow along the stream-wise direction, it may appear that the discharge due to the third electrode must induce

flow in the direction opposite to the free-stream flow, at least partially counteracting the effects of the first discharge. In practice, visual observation indicates that if any discharge at the third electrode exists, it is extremely weak, and it is expected that any effect on the flow due to the third electrode's discharge is also very weak. The major effect of the third electrode is the re-distribution of surface charge that accumulates on the dielectric, rather than a direct effect on the flow due to an additional discharge.

In the present study, little or no discharge activity is expected at the third electrode, for two reasons:

a) Distance: the electrode configuration used for this study features a grounded electrode that is not directly beneath the third electrode, but about 3 mm upstream of it. For 3 kV/mm breakdown voltage in air, it would take about 9 kV of voltage difference between the third electrode and the charged dielectric to produce a discharge.

b) Available voltage: the occurrence of $\Delta V \approx 9$ kV would be a much more infrequent event for the third electrode compared to the first electrode, since the applied signal as seen by the third electrode is the rectified positive half of the applied AC sinusoidal signal. For the required voltage difference to be available between the third electrode and the dielectric, we would need to operate at signal amplitudes greater than 18 kV_{pp}, which is higher than the voltage available for this study.

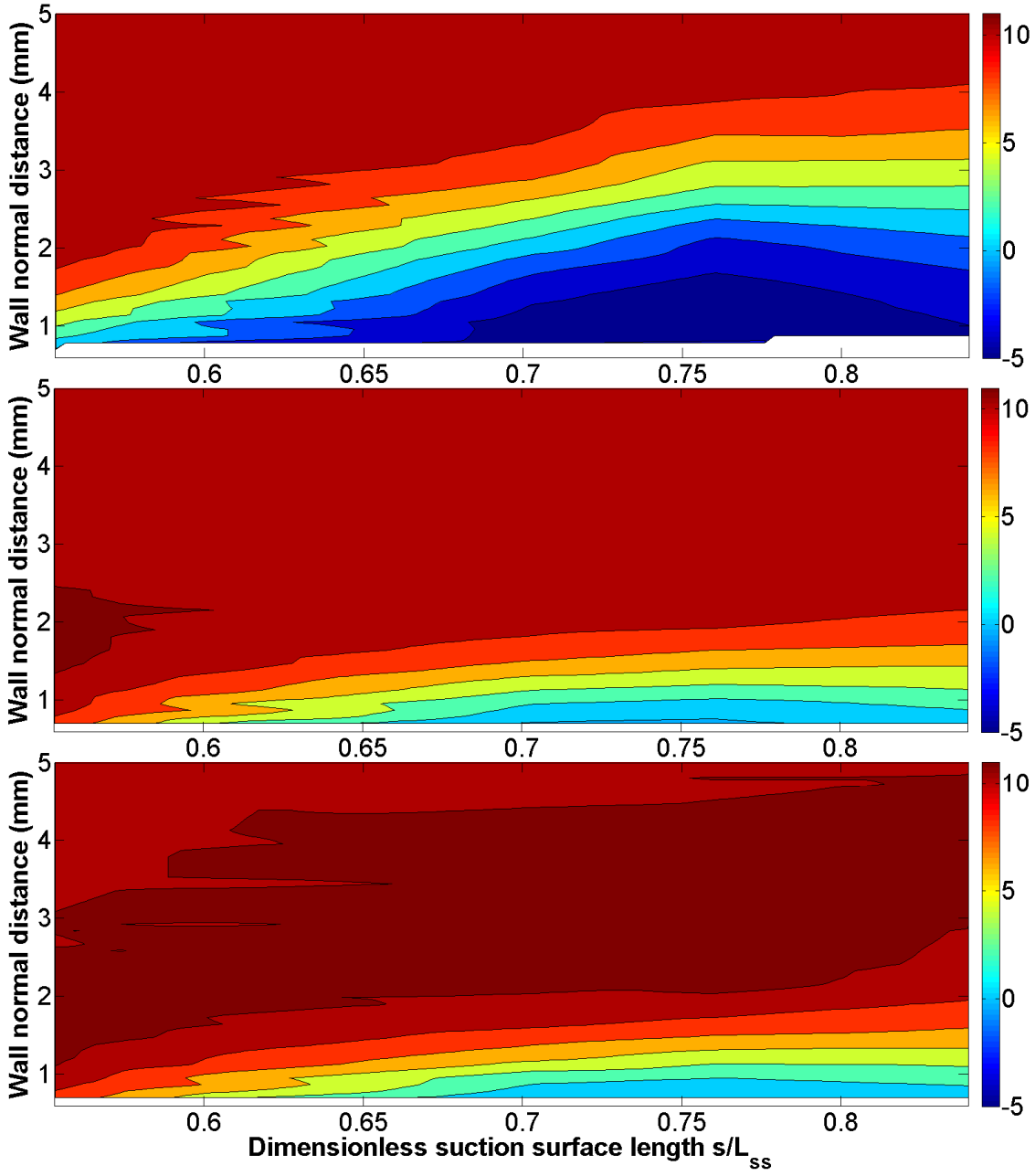

Figure 5-2 Total pressure (Pa) in the trailing part of the low pressure turbine passage, with the actuator off (top), on in the two-electrode configuration (middle), and on in the three-electrode configuration (bottom).

While the third electrode is seen to be the more effective of the two geometries, it can limit the performance of the two-electrode geometry in its present configuration. This is because the signal amplitude that can be used with the third electrode present is limited by initiation of arcing between the two exposed electrodes. A purely two-electrode configuration would have no such limitation. An optimally located third electrode would increase the stream-wise momentum coupled by the discharge into the flow, but would be far enough from the first electrode to prevent arcing.

The wall-normal gradient of the total pressure is plotted in Figure 5-3. Zones of high shear are visible as areas of high positive total-pressure gradient, indicated in red. Separation of the shear layer can be seen in the case with the actuator off (top), while it appears to remain attached in the two- and three-electrode cases (middle and bottom). As mentioned before, it is possible that a thin separation bubble exists very near the wall. Additionally, the high momentum region formed due to the presence of the actuator is visible as a dark blue streak in the two cases with the actuator activated.

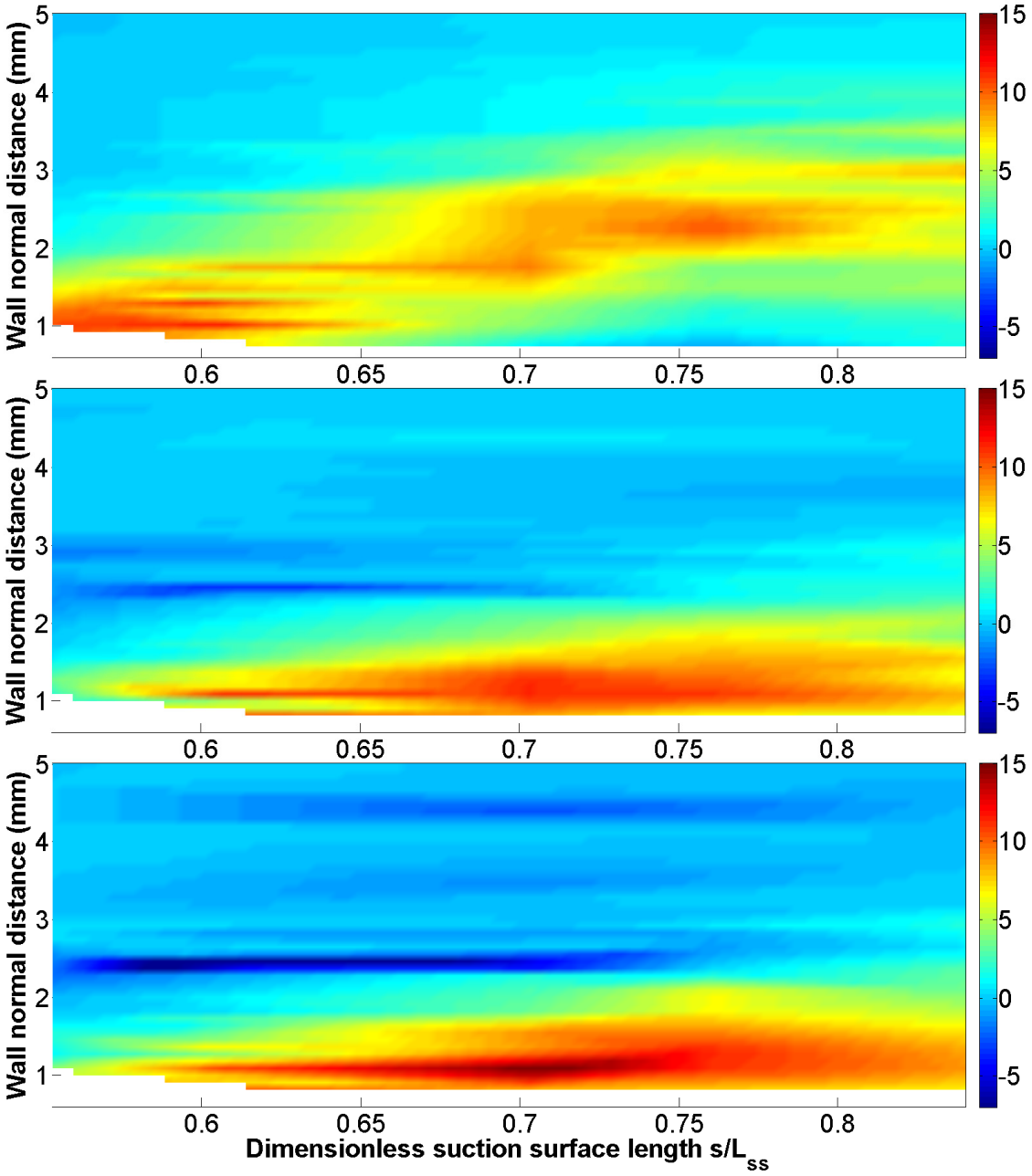

Figure 5-3 Wall-normal gradient of total pressure (Pa/mm) in the trailing part of the low pressure turbine passage, with the actuator off (top), on in the two-electrode configuration (middle), and on in the three-electrode configuration (bottom).

Summary

The region of high momentum flow produced due to the presence of the actuator is found to be above the shear layer, and not at the wall. The near-suction-surface total pressure field in the trailing part of the airfoil passage and its wall-normal gradient are used to demonstrate effective prevention of flow separation using the plasma actuator.

Total pressure measurements were taken with a glass total pressure tube, corrected for streamline displacement due to wall and shear effects, and validated using previous hot-wire data. Results are plotted as fields of total pressure (Pa) and wall-normal gradient of total pressure (Pa/mm) in the near-suction-surface trailing part of the passage.

Both configurations showed fully attached flow (or very thin separation zones) with the actuator activated. The three-electrode configuration was somewhat more effective than the two-electrode configuration. The presence of the third electrode can limit performance by direct arcing, depending upon the applied signal and the distance between the exposed electrodes. Both configurations produced zones of high momentum flow directed away from the wall, which are formed when the free-stream encounters and is diverted by the presence of the "bump" formed by the actuator.

The greater effectiveness of the three-electrode configuration was attributed to surface charge re-distribution due to the third electrode, leading to increased stream-wise acceleration of the charged particles in the plasma, which is imparted to the neutral fluid by collisions.

6. Unsteady flow results

In this chapter, characterization of flow separation control by the DBD plasma actuator in the Pack-B airfoil passage with passing wakes is presented.

6.1. Background

The characteristics of flow in a low-pressure turbine stage were presented in Chapter 1. Some of the discernible features of this flow field with wakes passing are as follows: at the test conditions of Reynolds number Re_{Lss} = 50,000 and the free-stream turbulence level of 2.5%, the flow experiences laminar separation. The passing wake produces transition to turbulence in the separated shear layer, which then re-attaches. The newly re-attached boundary layer resembles a thin laminar boundary layer, and is considered to be "becalmed," i.e., it is quite resistant to separation. This layer continues to grow until it becomes thick and unstable, and eventually separates. With the arrival of the next wake, the "transition – re-attachment – becalmed – growth – separation" cycle repeats.

6.2. Measurement considerations

All flow measurements presented in this chapter were hot-wire measurements. Details of the instruments and experimental methods used can be found in Section 3.3.

Wall-normal velocity profiles were taken with the actuator off, and then on, at three stream-wise locations, s/L_{ss} = 0.703, 0.76, and 0.84. The electrical parameters for the actuator were unchanged from the glass pressure tube study: a 9 kHz, 14.6 kV_{p-p} AC sinusoidal signal, pulsed at 80 Hz with a 60% duty cycle. The airfoil, dielectric, and actuator were also unchanged. The actuator was also unchanged from that study: it was made using a 1.3 mm glass dielectric.

For a given profile, the wall was found by visually observing contact of the boundary-layer hot-wire probe with its reflection on the glass surface of the dielectric on the airfoil.

The probe is then slowly stepped away from the wall in increments of 5 μm. At the first instance of the probe breaking contact with the wall, a distinct drop in anemometer output voltage is observed. For the purpose of measurement, this location is considered to be the wall. To reduce the risk of discharge or interference from any surface charge deposited on the dielectric by the plasma discharge, the probe was moved 0.1 mm away from the wall before initiating measurements or plasma operation.

For each wall-normal location, measurements were taken with the actuator off, followed immediately by measurements with the actuator on, before moving to the next location away from the wall. Measured quantities at each location are ensemble-averages of 175 wakes, produced by cycling the wake generator 35 times, with 5 wakes per pass of the wake generator. 70,000 samples of hot-wire data were taken during each pass of the wake generator. As discussed in Section 3.3, 60% of these samples were affected by the electric field, and discarded. The remaining 40% of the data form the basis of these measurements.

Each profile was taken in steps that were more closely spaced near the wall, and more sparsely spaced farther away from the wall. Originally, a location of 16.5 mm away from the wall was chosen as the farthest location from the wall for each profile. However, regardless of the stream-wise location, each hot-wire sensor used to take a profile beginning at the wall failed around 4 to 4.5 mm away from the wall. This corresponds to about 5 hours of run-time in the test environment, half of which were with the actuator switched off. The failure was observed as a sudden drop in anemometer output voltage, and not a gradual drift. No obvious damage to the sensor wire was observed when viewed with a microscope. The mechanism for the failure of the wire is not well understood. Each profile in this study was therefore taken with a different, newly-calibrated hot-wire probe. The data in this part of the study are restricted to a near-wall region that is 3.5 mm thick.

Apart from the effect of the electric field on the hot-wire measurements discussed in Section 3.3, other interference effects on the experimental apparatus were observed. These are discussed below.

As mentioned in Section 2.3, the wake generator mechanism comprises a moving sled that holds a set of rods. This sled is driven by a motor assembly. It was found that when the actuator was on, the motor driving the wake generator sled would occasionally accelerate to high rotational speeds, causing the sled to translate at velocities sufficient to damage the assembly. A large wire-mesh screen was placed between the actuator and the motor to shield the latter from the electric field. Testing to check for constant velocity from the mechanism showed this to be a success. The problem was likely to be an interference of the actuator electric field with the electronics of the motor speed controller.

The actuator was also found to intermittently interfere with the optical encoder system that was used to track the motion of the wake generator sled in time. Occasionally, when the actuator was on, the system would produce an output waveform that remained fixed in the high 5 V state, instead of producing a series of 0 to 5 V square waves corresponding to the linear encoder pattern. This interference was found to be sensitive to the position of the cable connecting the live terminal of the electrical amplifier to the actuator.

All results with passing wakes that had the actuator operating were taken in the two-electrode configuration. The third electrode was physically present on the airfoil, but not electrically connected. This decision was motivated with the intention of keeping the hot-wire probe as far as possible from the electrically active components of the actuator, to minimize any arcing, or possible electrical interference; the third electrode is noticeably farther downstream than the first and second electrodes. Despite this precaution, when attempts were made to take hot-wire measurements at s/L_{ss}= 0.613, as was done with the

glass pressure tube, arcing occurred between the probe supports and the (electrically disconnected) third electrode. While one or two seconds of this arcing did not appear to damage the hot-wire sensor in any discernible way, other researchers (Jukes et al., 2008) have observed arcing "vaporizing the wire and part of the prongs" when the hotwire approached a distance of within 3 mm of the exposed electrode. The position s/L_{ss} = 0.703 is therefore the most upstream location for the study with passing wakes.

For comparison, in the flow with no passing wakes and the actuator off, the stream-wise location of separation on the airfoil from the study without wakes is seen to be at $s/L_{ss} \approx 0.65$ (Figure 5-3).

The third electrode was not removed from the airfoil to keep all results directly comparable to those of the glass pressure tube study; any hydrodynamic effects of the third electrode's presence on the flow, however small, remained unchanged for the wake-passing study.

6.3. Results and discussion

Actuator off

Figure 6-2 through Figure 6-4 show the near-wall velocity field in the trailing part of the Pack-B airfoil's suction surface, in time increments of $1/9^{th}$ of the periodic wake-passing cycle, with the actuator off. The corresponding plots of velocity gradient in the wall-normal direction are shown in Figure 6-5 through Figure 6-7.

The top plots of Figure 6-14, Figure 6-16, and Figure 6-18 show the time-varying velocity during the periodic wake-passing cycle at dimensionless stream-wise locations s/L_{ss} of 0.703, 0.76, and 0.84, respectively, with the actuator off. The corresponding plots of velocity gradient in the wall-normal direction are shown in Figure 6-15, Figure 6-17, and Figure 6-19.

A large separation bubble exists at the wall between 1°~160° of a 360° cycle. See, for example, frames 1 through 4 (of the 9-frame periodic series) in Figure 6-2, Figure 6-3, Figure 6-5, and Figure 6-6. This darkest blue (lowest velocity) zone appears to extend through about two-thirds of the stream-wise extent of the field, showing an apparent sharp decrease in wall-normal thickness in the most downstream one-third of the bubble in these frames.

While the upstream part of the bubble contains nearly stagnant fluid, relatively strong reversed flow is expected to be present in the far downstream near-wall zone of the bubble (see Figure 6-1). A typical hot-wire anemometer cannot distinguish between reversed and forward flow directions. The apparent thinning of the bubble in this most downstream near-wall zone is likely due to over-prediction of mean velocity due to "folding" of the hot-wire signal in the reversed flow zone.

The stream-wise location with the highest reversed/forward flow intermittency corresponds to the region associated with the onset of shedding of vortical structures from the bubble (Häggmark et al., 2000), producing a three-dimensional unsteady flow farther downstream. When time-averaged, this unsteadiness produces the diffused appearance of the separated shear layer in the downstream section of the measurement field. In frame 1 of Figure 6-5, for instance, the separated shear layer begins 2 mm from the wall at $s/L_{ss} \sim 0.703$ with a relatively sharply-defined high gradient (proportional to the shear intensity). As it arcs over the bubble and leaves the downstream end of the measurement field, the thin zone of high gradient has spread into a broad zone having approximate one-half of its initial magnitude.

The bubble continues to thicken through this stage (frames 1 through 4). Observe, for instance, the progressively diverging orange and red color zones in the first four frames of Figure 6-2 and Figure 6-3.

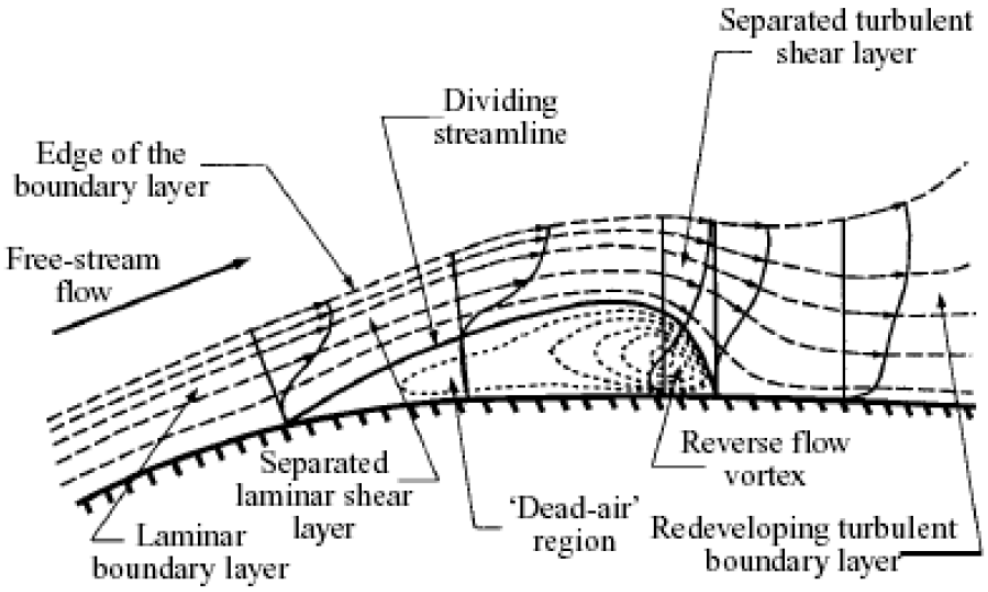

Figure 6-1 Time-averaged structure of a laminar separation bubble (Horton, 1968)

Around frame 5 (161°~200°), the wake has passed. The interaction of the wake with the inflectional, unstable separated shear layer triggers the roll-up of vortices, which rapidly break down to induce transition in the shear layer. The enhanced turbulent mixing of high momentum fluid from the free-stream into the bubble side of the shear layer promotes re-attachment, which follows the wake downstream (Hodson and Howell, 2005). A comparison of frames 4 and 5 in Figure 6-3 shows rapid thinning of the bubble's upstream edge, followed by re-attachment in frame 6 (201°~240°).

A thin, attached boundary layer has formed, which persists through frames 6 and 7 (201°~280°). The attachment point can be seen receding downstream in frame 8 (281°~320°) of Figure 6-7. This is the becalmed zone that follows the wake disturbance in space.

These features can also be seen in the plots of time-varying velocity gradient at each stream-wise location (top, Figure 6-15, Figure 6-17, Figure 6-19). For s/L_{ss} of 0.703, the near-wall region shows attached flow between about 200° and 300°. The calmed zone

appears to grow somewhat in spatial extent as it travels downstream, with the trailing end of the zone persisting till about 320° for s/L_{ss} ~ 0.76, and about 340° for s/L_{ss} ~ 0.84. This feature is in good qualitative agreement with the original findings of Schubauer and Klebanoff (1955), who showed the trailing edge celerity of the calmed zone to be significantly lower than the leading edge celerity; the actual values depend on the local pressure gradient.

By frame 8 (281°~320°) of Figure 6-4 and Figure 6-7, the upstream near-wall zone has started to thicken again. This is also seen in Figure 6-14 and Figure 6-15. The flow about 3 mm away from the wall lags in time and is still thinning. Compare, for instance, the orange 3 m/s zone in frames 4, 7, and 8.

The separation bubble appears to have re-established itself between frame 9 (321°~360°) and frame 1 (1°~40°). The small traces of high shear visible near the wall at the downstream end (s/L_{ss} ~ 0.84) of the bubble in frames 1 through 5 are likely to be indicative of the reversed flow in the separation bubble, as discussed above. This is different in character from the near-wall shear layer that is initiated at the upstream end around frame 5, and persists till about frame 9. From frame 1, the bubble continues its cyclic growth until the arrival of the next wake.

Actuator on

Figure 6-8 through Figure 6-10 show the near-wall velocity field in the trailing part of the Pack-B airfoil's suction surface, in time increments of $1/9^{th}$ of the periodic wake-passing cycle, with the actuator on. Figure 6-11 through Figure 6-13 show the corresponding near-wall velocity gradient in the wall-normal direction.

The bottom plots of Figure 6-14, Figure 6-16, and Figure 6-18 show the time-varying velocity during the periodic wake-passing cycle at dimensionless stream-wise locations s/L_{ss} of 0.703, 0.76, and 0.84, respectively, with the actuator on. The corresponding plots

of velocity gradient in the wall-normal direction are shown in Figure 6-15, Figure 6-17, and Figure 6-19.

Measurements of the flow field with the actuator on show relatively few features with time-dependent variations when compared to those taken of the flow field with the actuator off. Strong similarities to total pressure measurements taken in the steady (i.e., without passing wakes) airfoil passage flow (Figure 5-2 and Figure 5-3) are also evident. Note that the stream-wise extent of measurements in the steady flow is larger in both upstream and downstream directions than this study with passing wakes.

All frames (1°~360°) of the wake-passing cycle show a boundary layer that appears to be attached throughout the periodic wake passing cycle when the actuator is on. This attached layer thins slightly between dimensionless stream-wise locations s/L_{ss} of 0.703 and 0.76. The total pressure measurements taken in the steady flow (Figure 5-2) show a slight thickening between the first two stream-wise locations mentioned above, but otherwise are in close qualitative agreement with this description. Both boundary layers continue to thicken downstream of s/L_{ss} ~0.76, as they navigate the continuing adverse pressure. The nominal thickness of the boundary layer in both sets of measurements is about 1.5 to 2.0 mm.

A band of high velocity flow located above the attached boundary layer is observed in all frames of measurements with the actuator on. This feature was also found in the steady flow measurements. As described previously, this accelerated zone of flow is produced when the free-stream encounters the "virtual bump" of actuator's patch of influence. In these measurements with passing wakes, this high velocity zone (seen as a red band in Figure 6-8 through Figure 6-10) shows a reduced spatial extent between frames 3 and 6 (81°~240°). This corresponds to the arrival and passage of the wake in the free-stream of the passage. The negative jet (i.e., velocity vectors pointed downward and forward) flow associated with the wake reduces the momentum of the upward-directed

flow from the virtual bump during this interaction. By frame 7, the red band of high velocity flow has regained its unperturbed shape, which it retains until the arrival of the next wake in the subsequent cycle.

It is noted that the first signs of the wake arrival in the free-stream were observed in frame 3 (81°~120°), as discussed above, while the first changes to the shear layer flow due to the wake (transition and re-attachment activity, with the actuator off) were observed in frame 5 (201°~240°). This time lag phenomenon between the free-stream flow and the near-wall flow is well known. The wake propagation speed varies between the free-stream and near-wall regions; boundary layers take time to respond to changes in free-stream conditions (Kaszeta and Simon, 2002).

The zone of highest shear (indicated by the largest values of wall-normal gradient of velocity) for all stream-wise locations throughout the wake-passing cycle was found to be approximately 0.6 to 0.7 mm from the wall. The near-wall gradient of velocity exceeded zero in all cases.

The highest values of shear were seen at the intermediate stream-wise location of s/L_{ss} ~ 0.76, followed by s/L_{ss} ~ 0.703. The shear values at the most downstream location were relatively weak. This pattern of shear intensifying at an intermediate stream-wise location, and then weakening closer to the trailing edge qualitatively resembles the steady flow measurements of total pressure gradient (Figure 5-3).

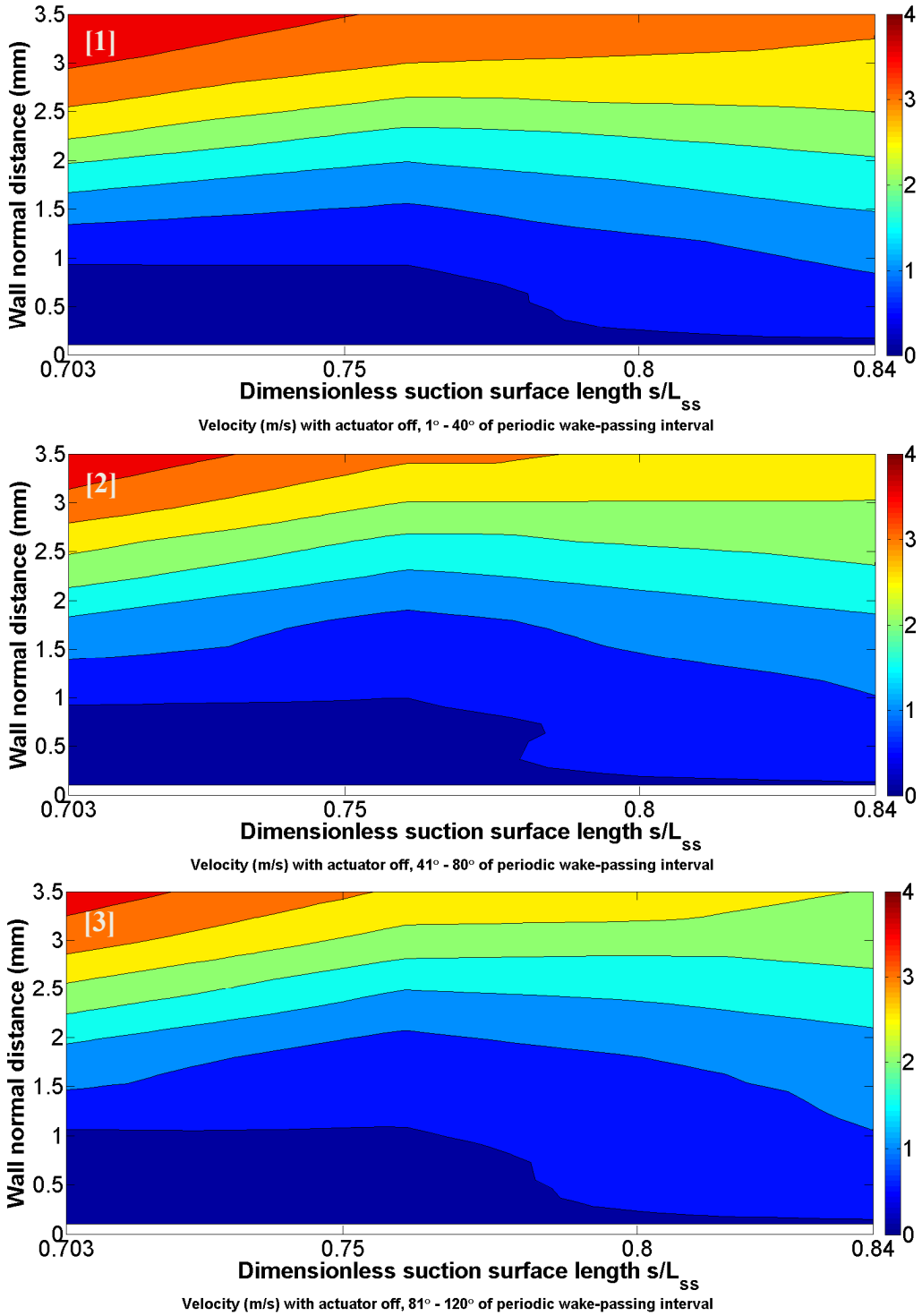

Figure 6-2 Velocity field (m/s) in the first one-third of the periodic wake-passing cycle, with the actuator off

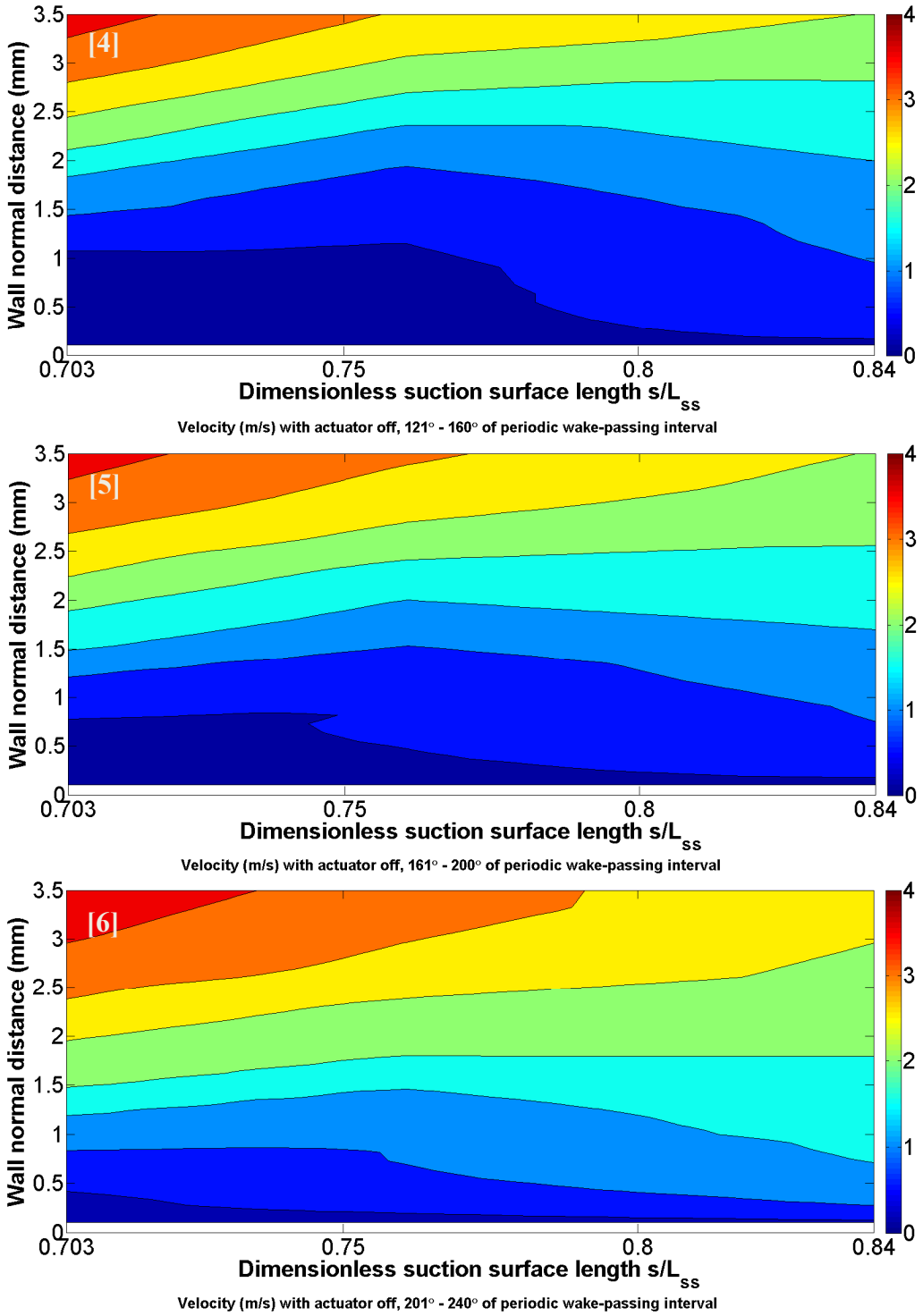

Figure 6-3 Velocity field (m/s) in the middle one-third of the periodic wake-passing cycle, with the actuator off

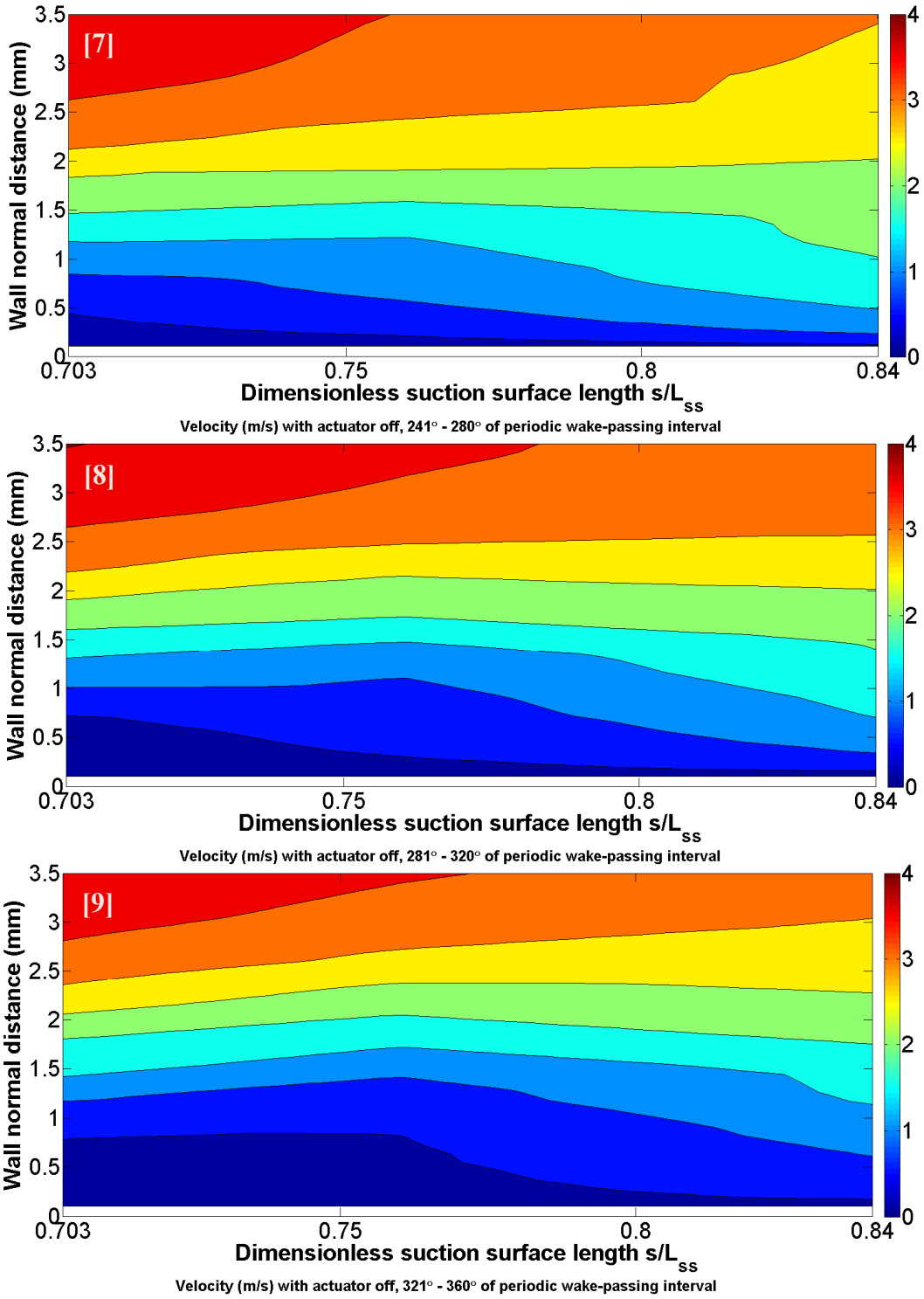

Figure 6-4 Velocity field (m/s) in the final one-third of the periodic wake-passing cycle, with the actuator off

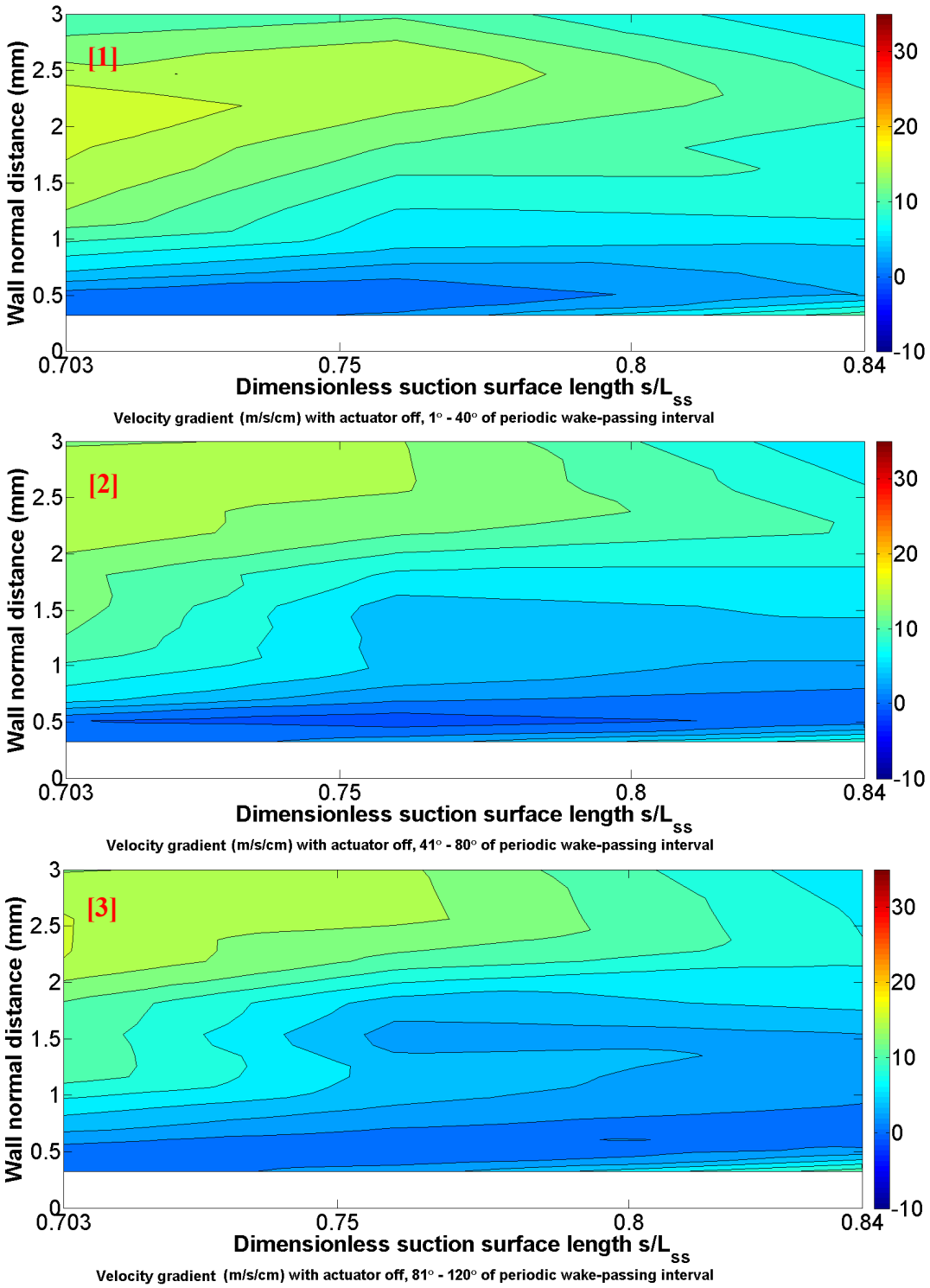

Figure 6-5 Wall-normal velocity gradient field (m/s/cm) in the first one-third of the periodic wake-passing cycle, with the actuator off

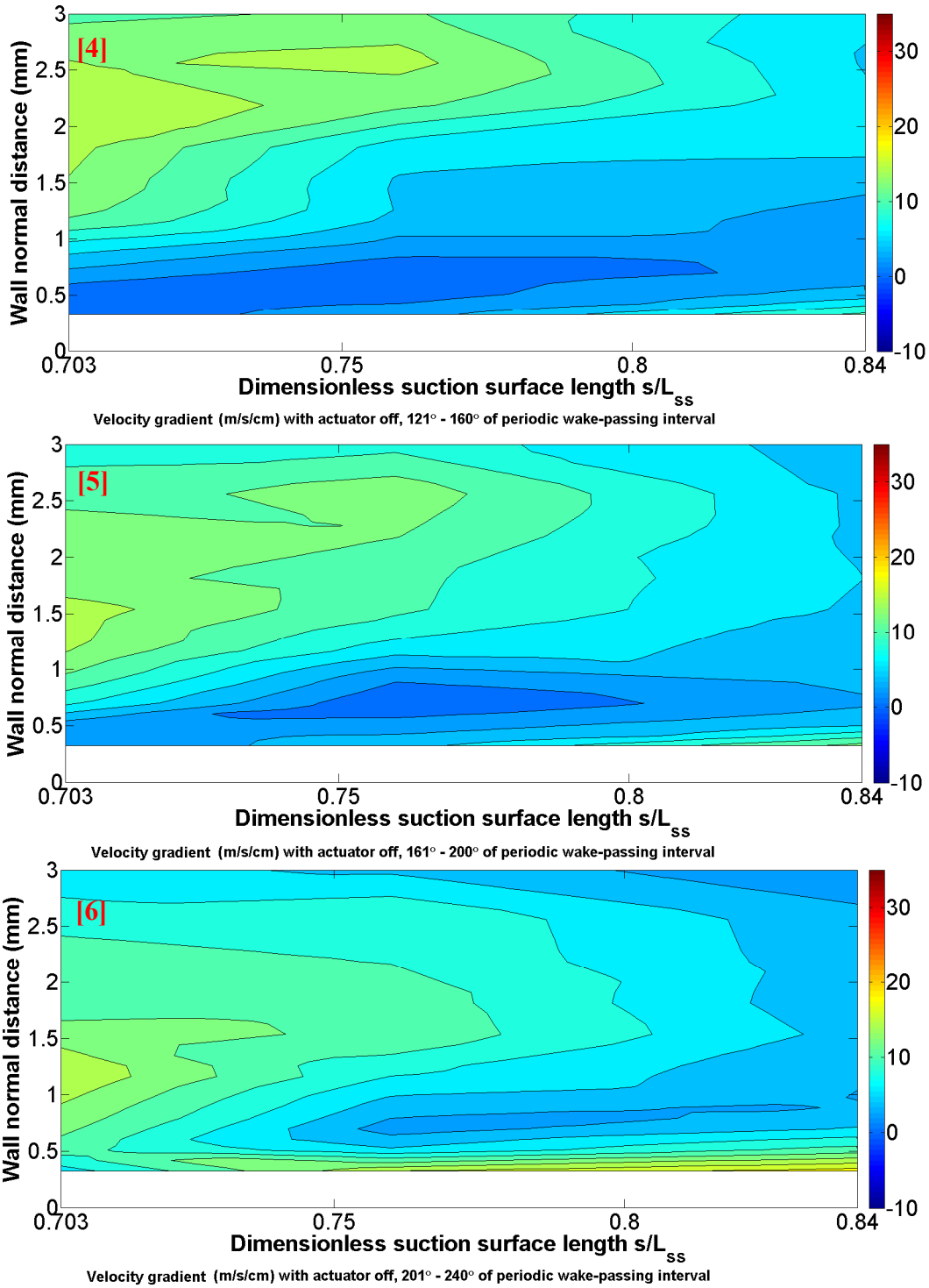

Figure 6-6 Wall-normal velocity gradient field (m/s/cm) in the middle one-third of the periodic wake-passing cycle, with the actuator off

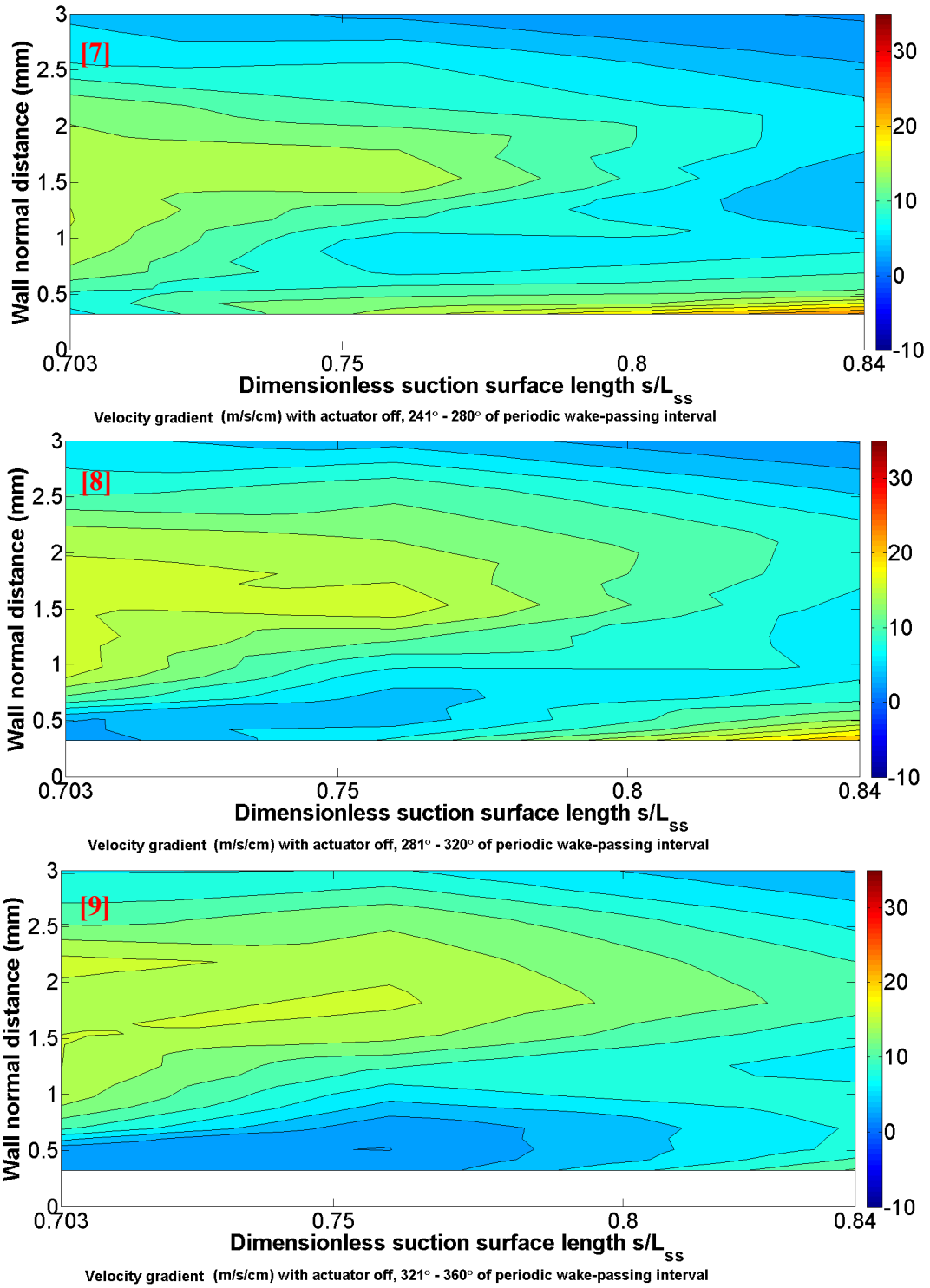

Figure 6-7 Wall-normal velocity gradient field (m/s/cm) in the final one-third of the periodic wake-passing cycle, with the actuator off

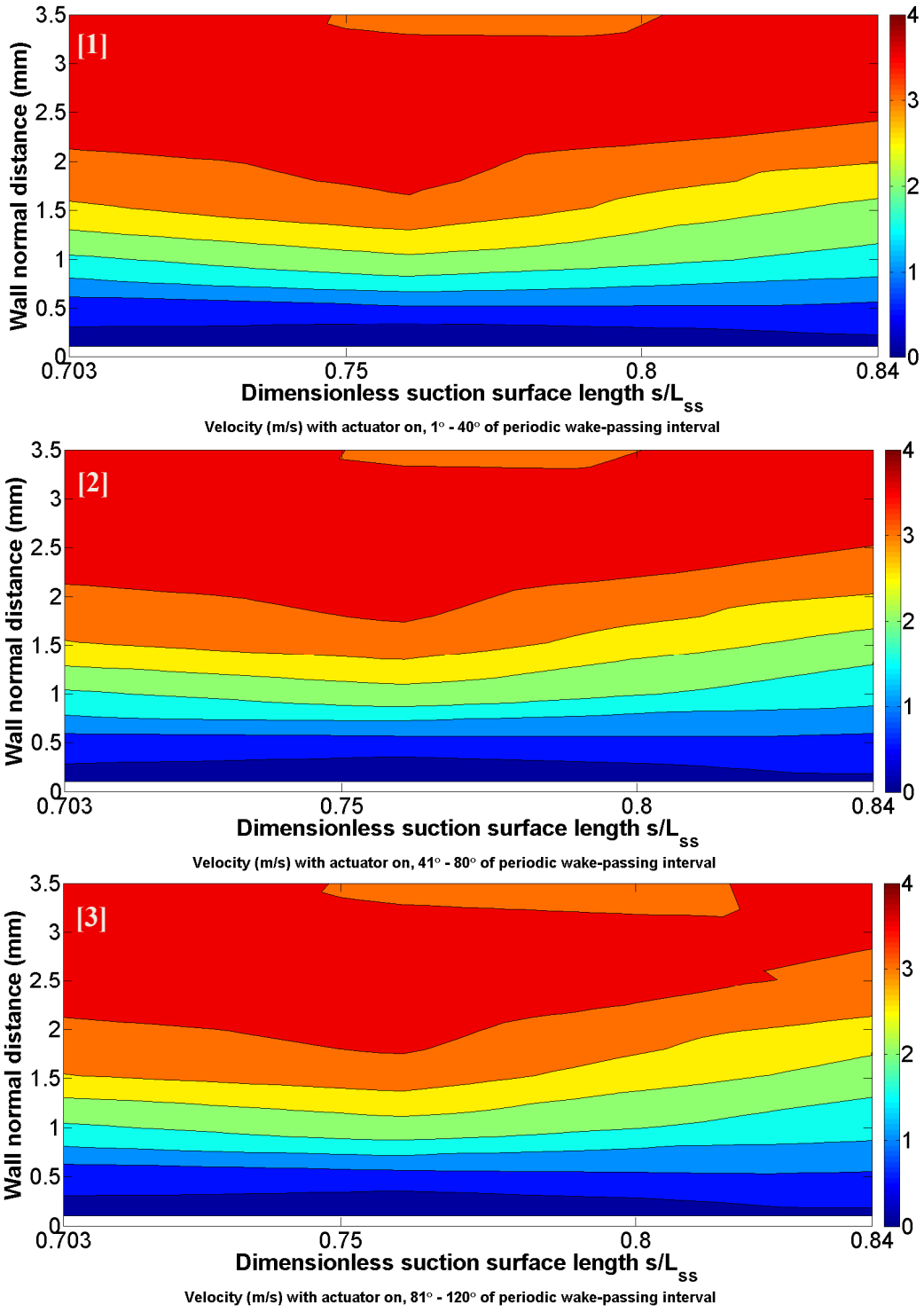

Figure 6-8 Velocity field (m/s) in the first one-third of the periodic wake-passing cycle, with the actuator on

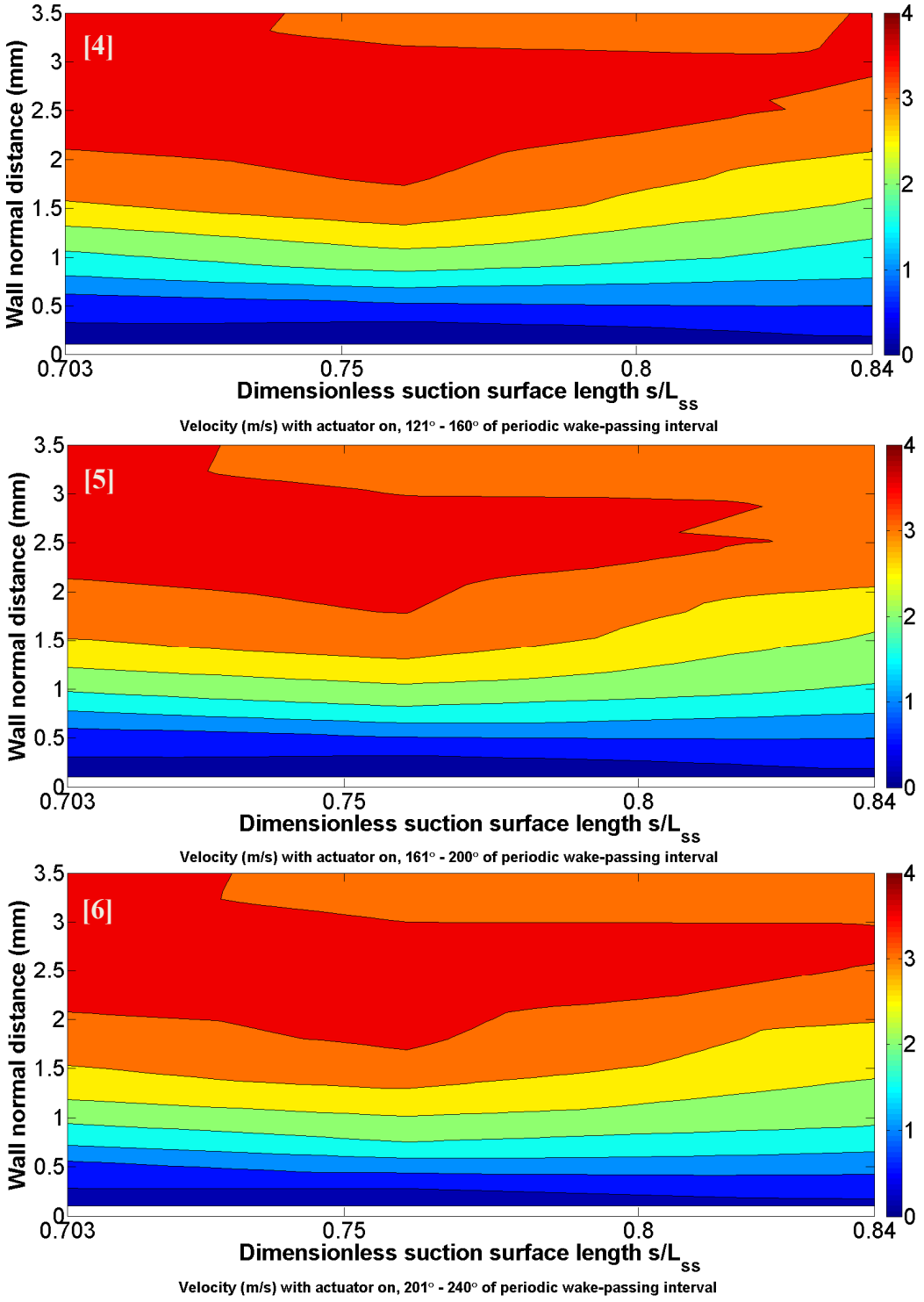

Figure 6-9 Velocity field (m/s) in the middle one-third of the periodic wake-passing cycle, with the actuator on

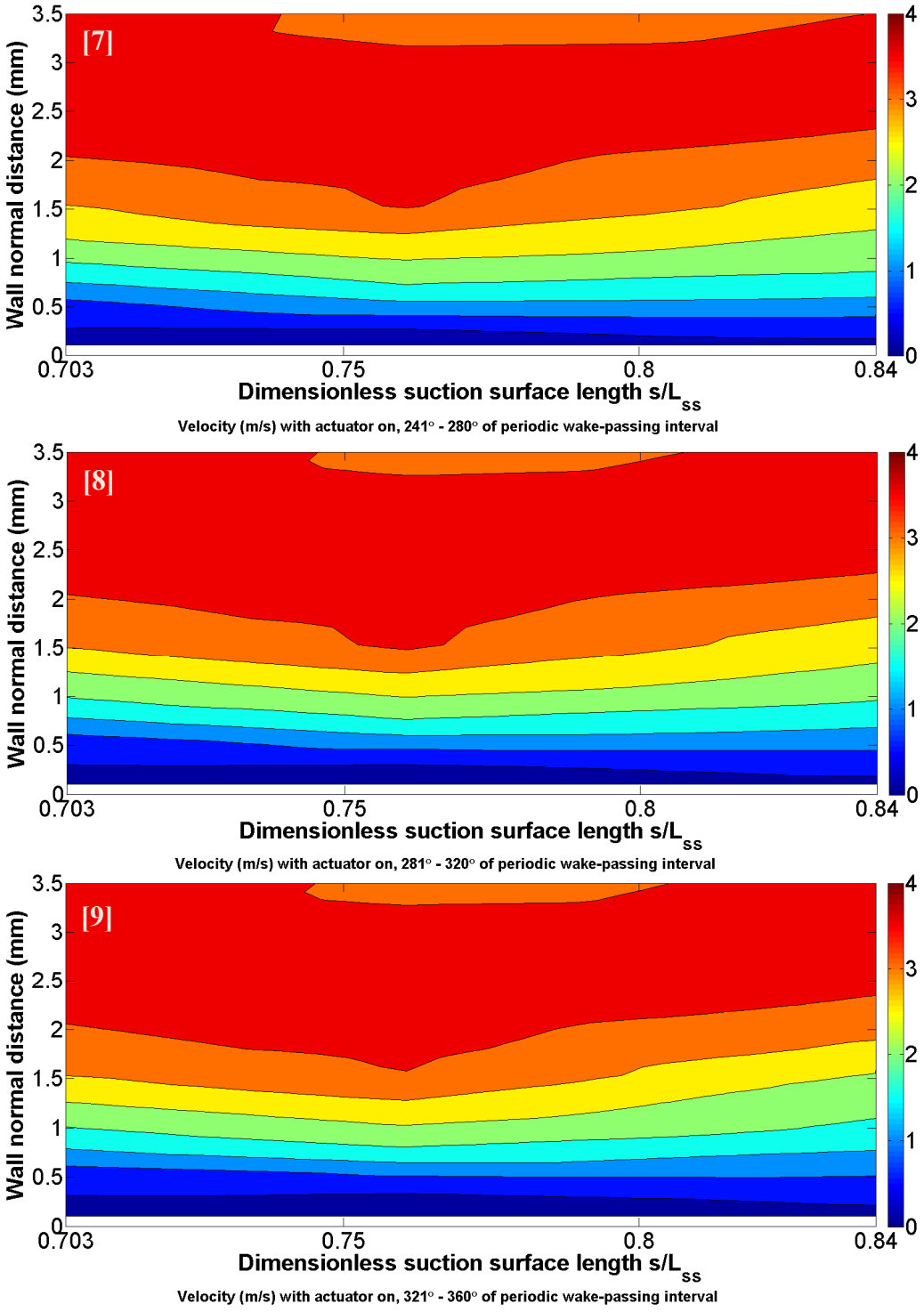

Figure 6-10 Velocity field (m/s) in the final one-third of the periodic wake-passing cycle, with the actuator on

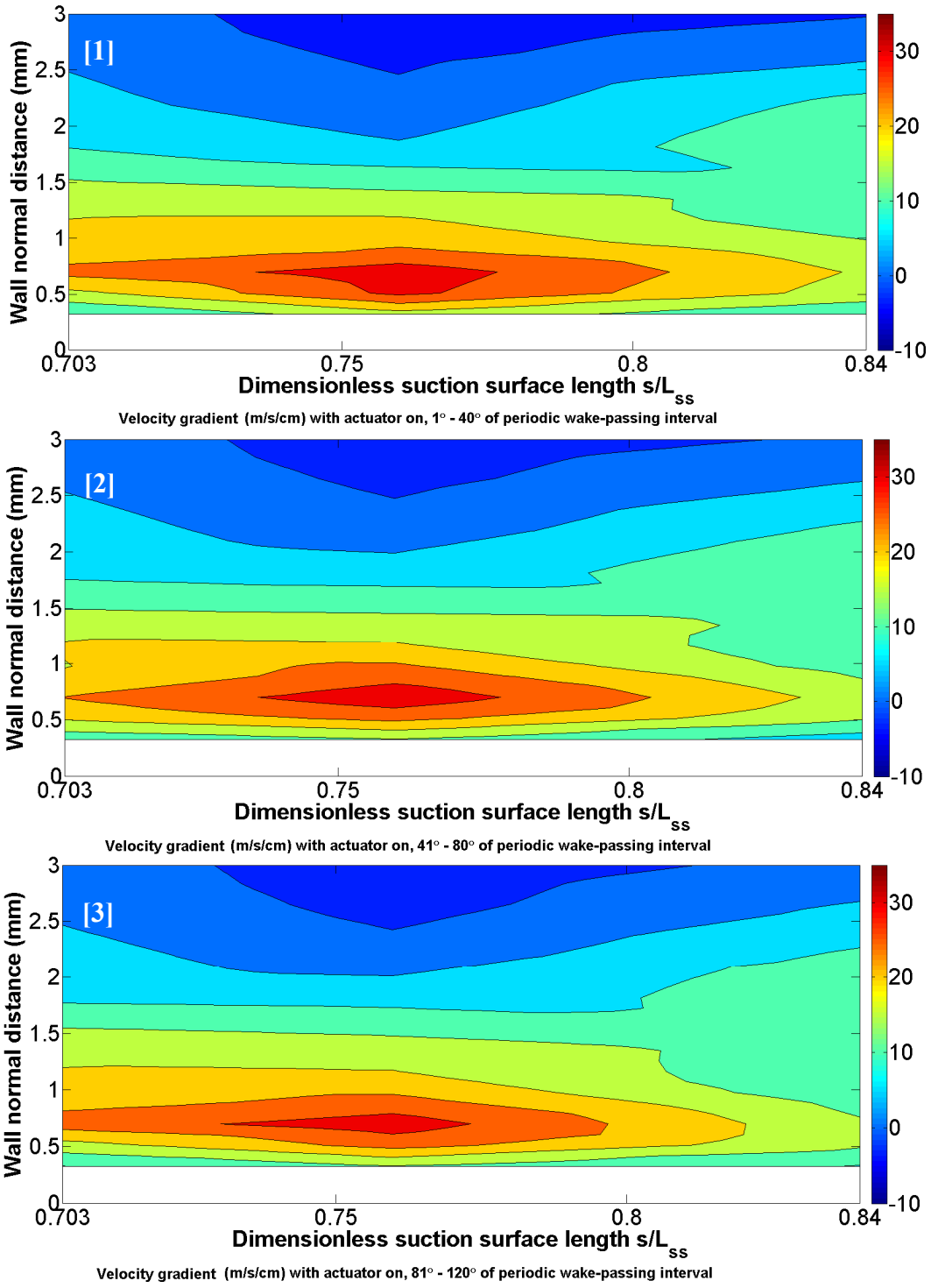

Figure 6-11 Wall-normal velocity gradient field (m/s/cm) in the first one-third of the periodic wake-passing cycle, with the actuator on

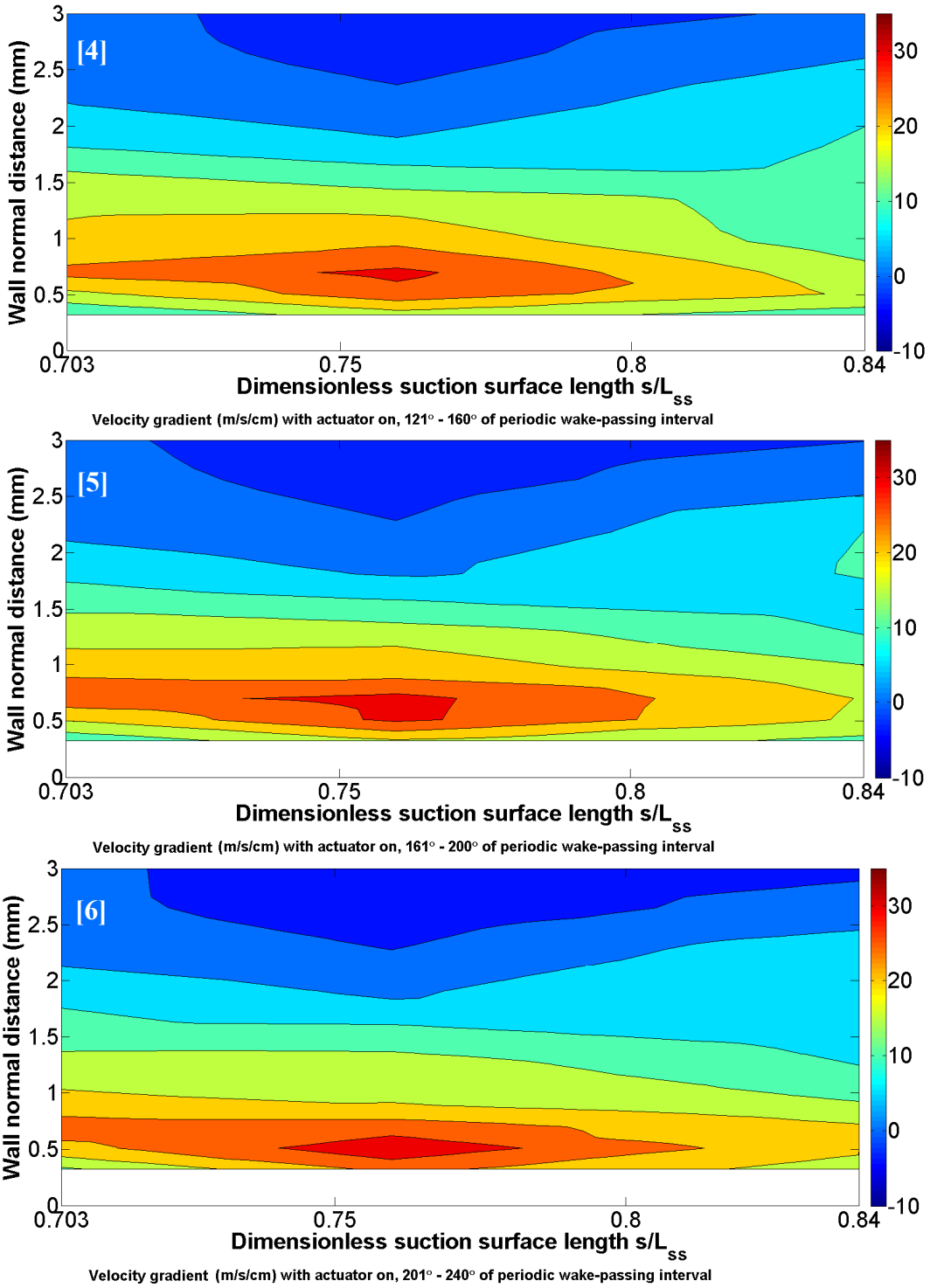

Figure 6-12 Wall-normal velocity gradient field (m/s/cm) in the middle one-third of the periodic wake-passing cycle, with the actuator on

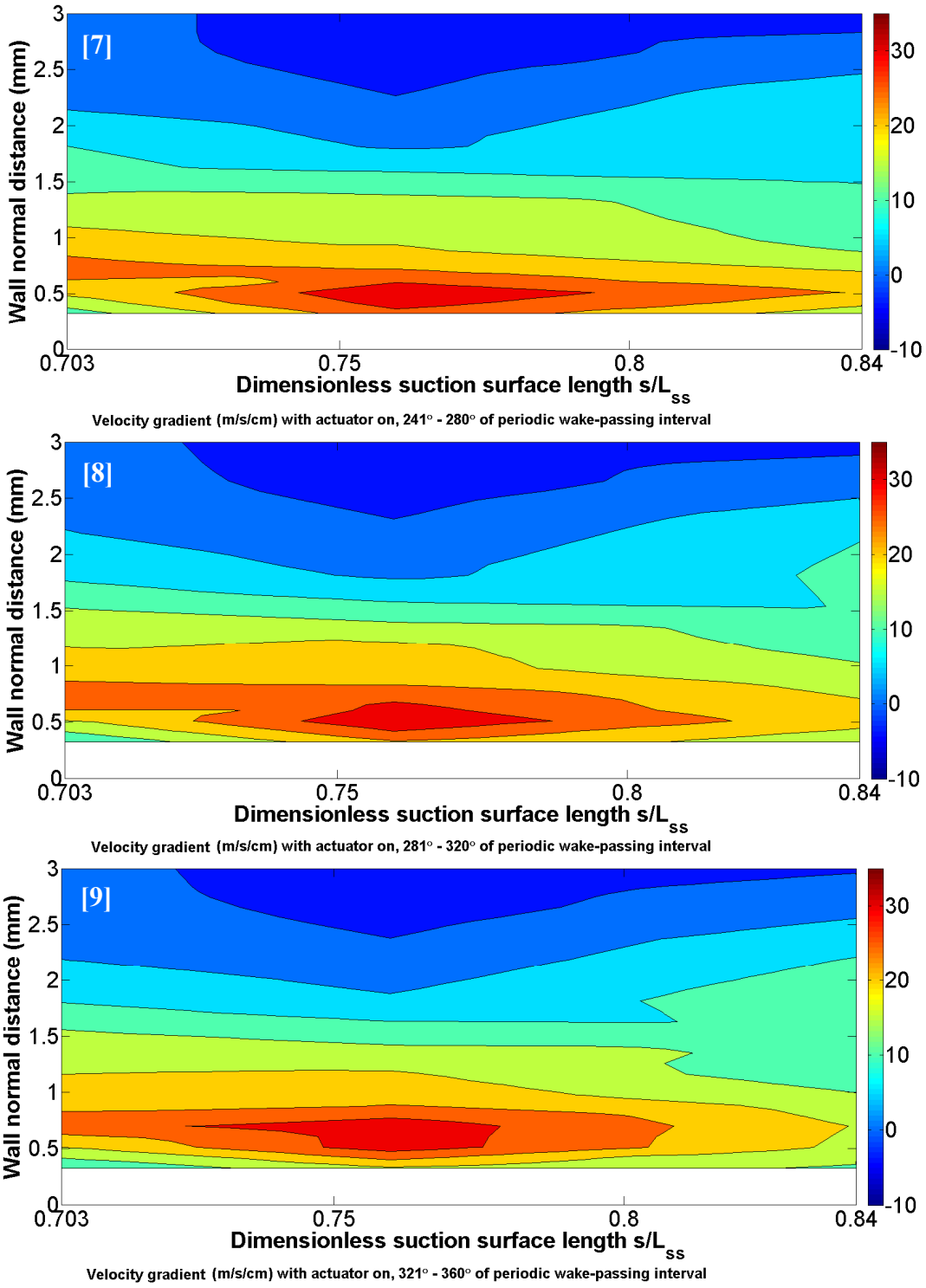

Figure 6-13 Wall-normal velocity gradient field (m/s/cm) in the final one-third of the periodic wake-passing cycle, with the actuator on

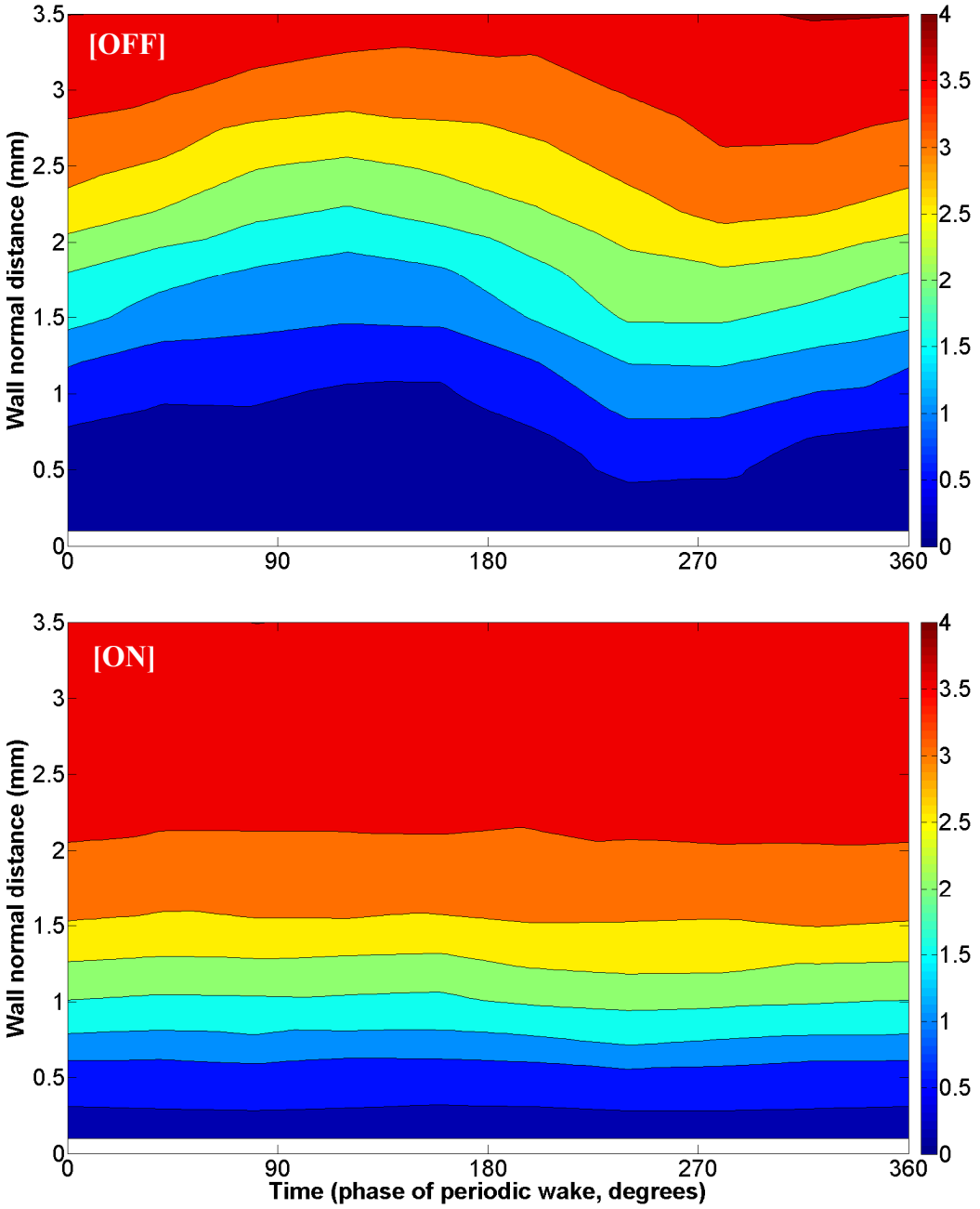

Figure 6-14 Time-varying velocity (m/s) through the periodic wake-passing cycle, with the actuator off (above) and on (below), at non-dimensional stream-wise location s/L_{ss} = 0.703

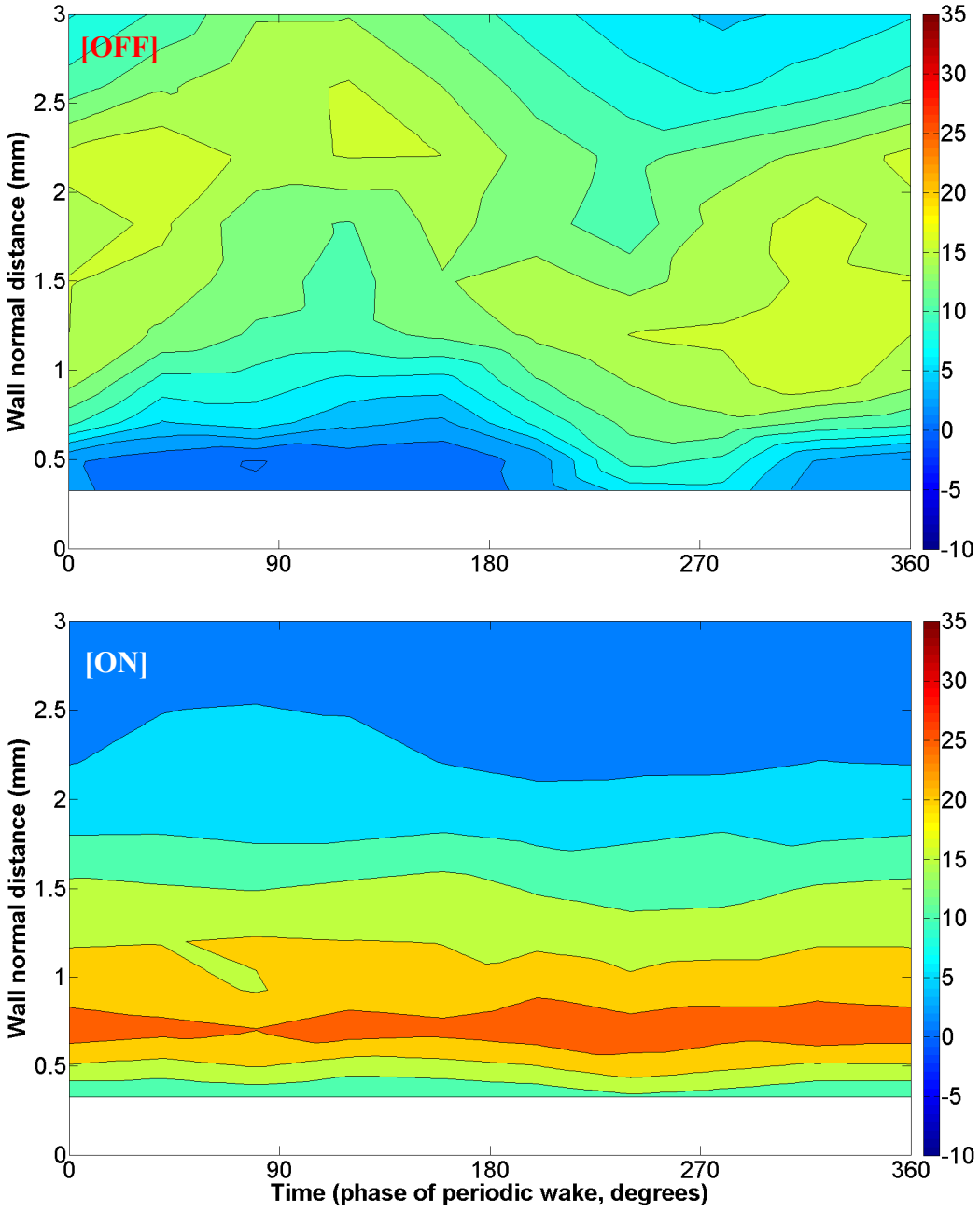

Figure 6-15 Time-varying wall-normal velocity gradient (m/s/cm) through the periodic wake-passing cycle, with the actuator off (above) and on (below), at non-dimensional stream-wise location s/L_{ss} = 0.703

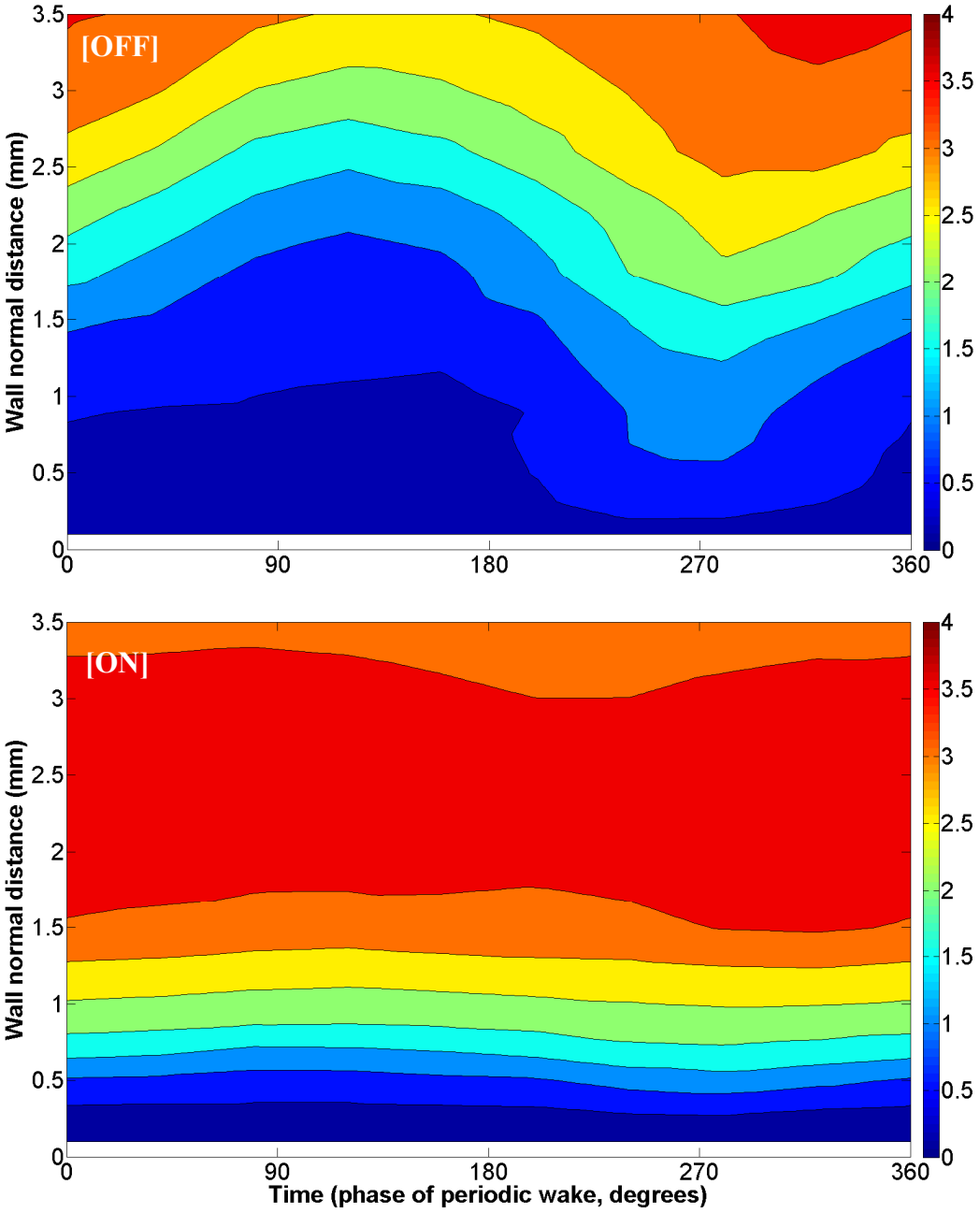

Figure 6-16 Time-varying velocity (m/s) through the periodic wake-passing cycle, with the actuator off (above) and on (below), at non-dimensional stream-wise location s/L_{ss} = 0.76

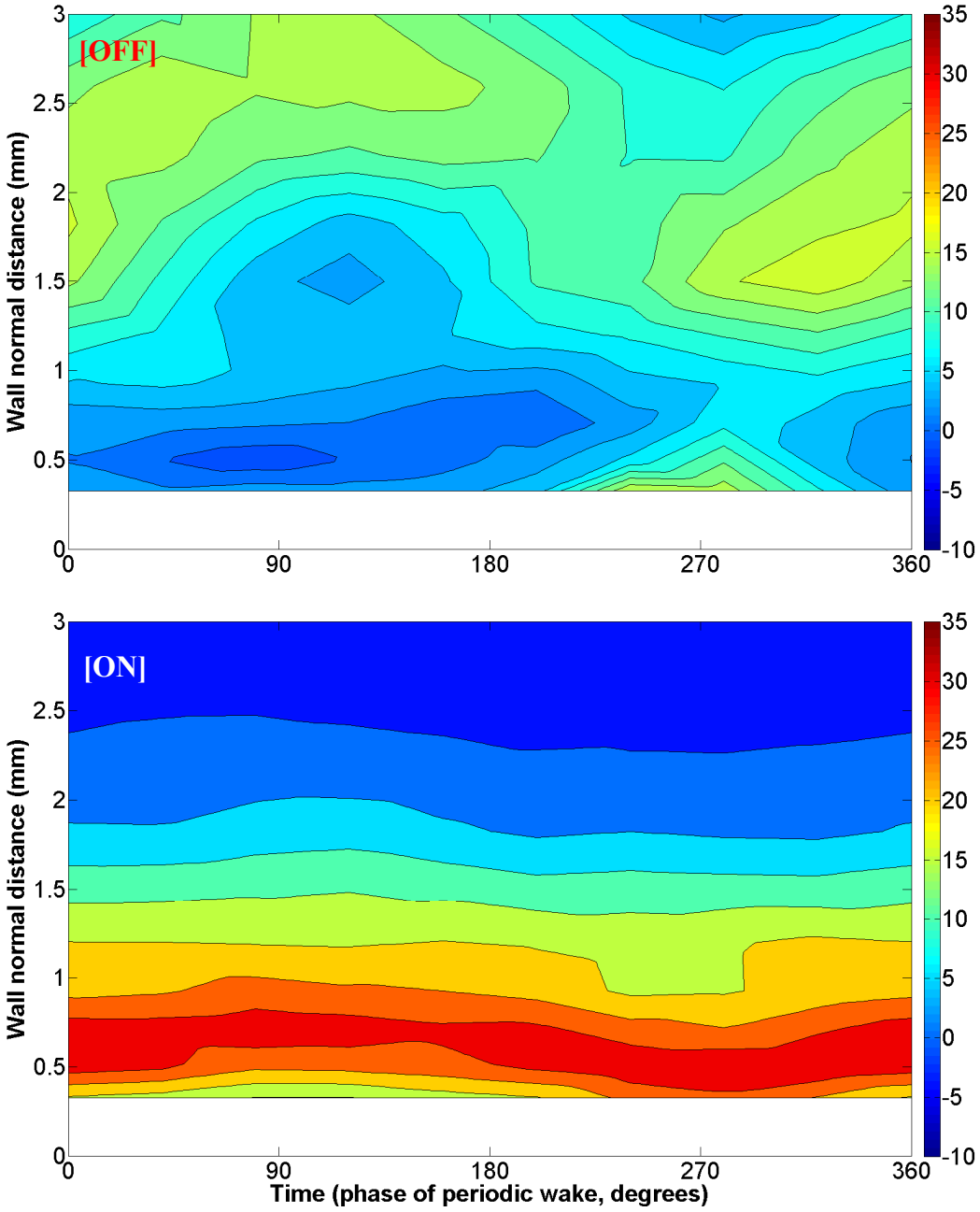

Figure 6-17 Time-varying wall-normal velocity gradient (m/s/cm) through the periodic wake-passing cycle, with the actuator off (above) and on (below), at non-dimensional stream-wise location s/L_{ss} = 0.76

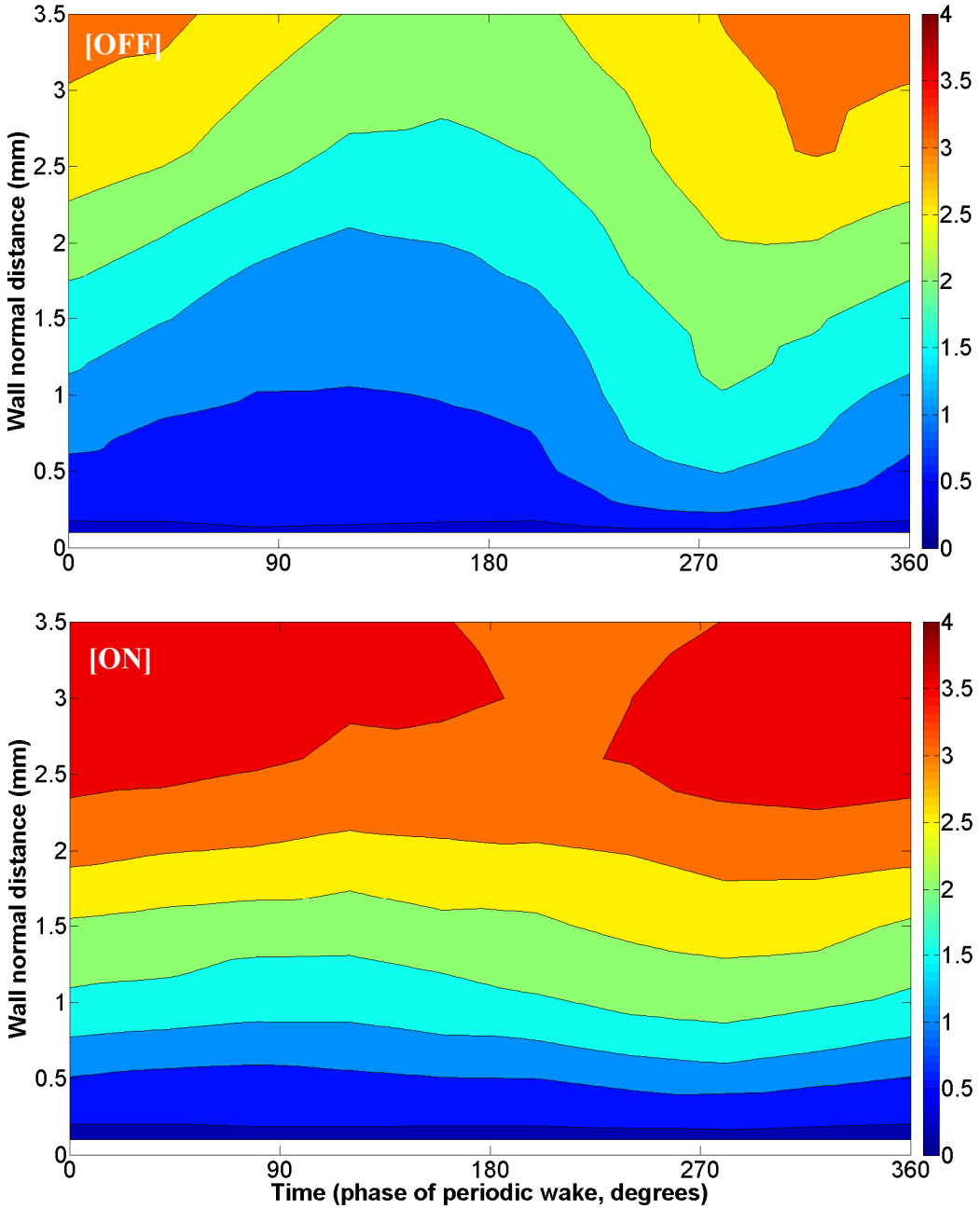

Figure 6-18 Time-varying velocity (m/s) through the periodic wake-passing cycle, with the actuator off (above) and on (below), at non-dimensional stream-wise location s/L_{ss} = 0.84

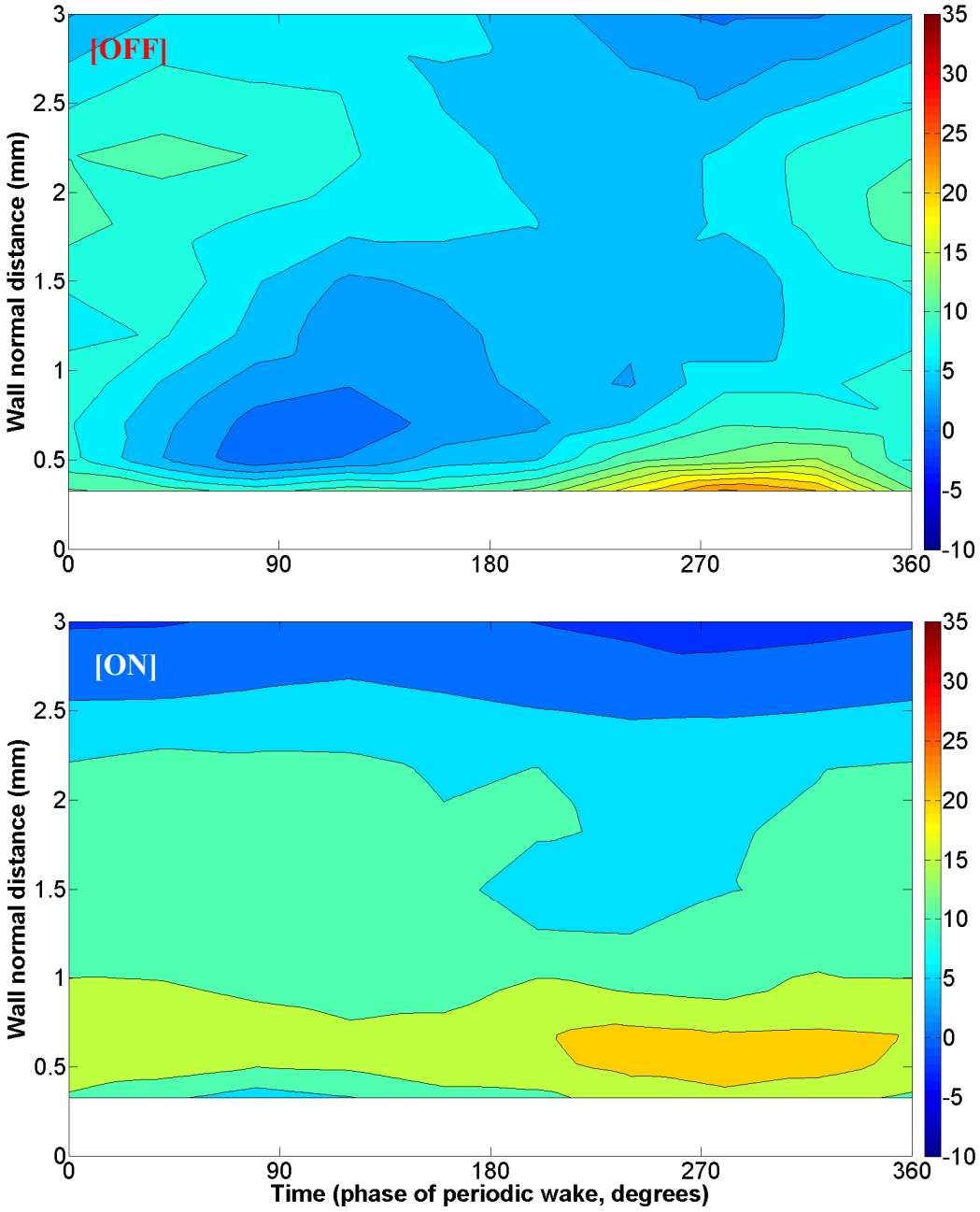

Figure 6-19 Time-varying wall-normal velocity gradient (m/s/cm) through the periodic wake-passing cycle, with the actuator off (above) and on (below), at non-dimensional stream-wise location s/L_{ss} = 0.84.

Summary

Near-wall measurements of velocity and wall-normal gradient of velocity were used to study flow separation control using a plasma actuator for the suction surface of a Pack-B LPT airfoil, with passing wakes. Hot-wire anemometry was used for taking these measurements, which are presented in this chapter.

Taking these measurements in the vicinity of the plasma discharge presented many challenges. As described in Section 3.3, the hot-wire signal was strongly affected by the operation of the discharge. In addition, sudden hot-wire probe failure occurred for each of the three stream-wise profile measurements taken. Strong electrical interference caused the photo-gate detector as well as the motor controller for the wake generator mechanism to intermittently malfunction.

Flow measurements taken with the actuator off show the presence of an unsteady separation bubble in the aft section of the suction surface. The passing wake triggers transition in the unstable shear layer, leading to re-attachment. A thin, fully attached becalmed region follows the wake, growing somewhat in extent as it moves downstream. After the passage of the becalmed region, the re-attachment point shifts downstream, the flow separates again, and bubble growth is observed.

Measurements taken in the flow with passing wakes show fully attached flow (or very thin separation zones) throughout the wake-passing cycle. Relatively few time-varying features were observed in the boundary layer. Good qualitative agreement of flow field features was found with the actuator-on steady flow case. Since the two sets of measurement were taken using entirely different instruments, methods and corrections, this agreement bolsters confidence in the validity of both sets of measurements. As previously seen in the steady flow, a zone of high velocity flow associated with the free-stream encountering the “virtual bump” of the actuator’s presence is observed over the

boundary layer. This feature in the free-stream did show time varying behavior: it is partially suppressed by the negative jet effect of the passing wake.

7. Discussion on aspects of flow control physics

While considerable background and literature exists on the topics of flow separation, bypass transition, wake-induced transition, and active flow control, low pressure turbines flows occur in environments that involve the complex interactions of multiple phenomena. The objective of this chapter is to relate some results of the present study to the recent literature of these topics, and to comment on several aspects of the pulsed control of separation in a high free-stream turbulence environment and the passage of wakes.

Nature of disturbances leading to separated-flow transition

Under low free-stream turbulence conditions, the span-wise KH vortices, or "rollers," shed from the separated shear layer are largely two-dimensional. Recent studies (Brinkerhoff and Yaras, 2011, Rao et al., 2013) show that stream-wise vortices associated with the hairpin structures generated upstream of separation from the late stages of the development of TS waves interact with these KH vortices, and produce growing waviness in them. The KH vortices break down to smaller three-dimensional structures, and eventually lead to turbulence in the shear layer.

As will be briefly discussed, the incremental addition of different combinations of high free-stream turbulence, upstream wakes, and forcing disturbances from an upstream control mechanism to this flow situation modifies this base-line physical picture. A unifying feature in all these situations, including the low free-stream turbulence case, is the interaction of stream-wise oriented and span-wise oriented flow structures; the origin of these structures varies according to the situation.

In the presence of high free-stream turbulence, Klebanoff streaks are produced near the leading edge, experiencing transient growth in the pre-separation boundary layer, as

expected. The low-speed streaks preferentially amplify in the decelerating part of the attached flow, and produce strong waviness in the shedding KH vortex in the separated flow (Rao et al., 2013). Turbulent spots are produced in the shear layer; proposed mechanisms involve the secondary instability of the amplified streaks (McAuliffe and Yaras, 2010), or the excitation of KH instability in the outer (near free-stream) parts of the low-speed streaks by the high frequency disturbances in the free-stream (Zaki and Durbin, 2005). The frequency of the primary instability closely matches the KH frequency for plane shear layers.

Wakes passing in the high free-stream turbulence environment are packets of disturbed flow in the free-stream, and can be considered to be a "negative jet" relative to the mean flow. In the boundary layer, a convecting zone of strongly amplified Klebanoff streaks travels with the wake, with leading- and trailing-edges speeds that match those of a classic turbulent spot: 88% and 50% of the free-stream velocity, respectively. This zone in the boundary layer lags behind the wake in the free-stream. The KH instability of the shedding vortices of the separated shear layer is influenced by the wake in the free-stream, as well as the weaker Klebanoff streaks generated in the upstream boundary layer by the high background free-stream turbulence, as before (Rao et al, 2013). The strongly amplified streaks associated with the effect of the wakes on the boundary layer arrive after the vortex shedding, and produce strong span-wise variations that cause rapid break down to turbulence, and correspond to the most upstream location of time-varying separation (Coull and Hodson, 2011)..

The nature and effect of disturbances introduced by flow control mechanisms can vary according to the frequency, amplitude, distribution, and relative orientation of the forcing perturbations to the mean flow. For efficient control, it is important to optimize these parameters so that small disturbances introduced into the flow experience growth by energy transfer from the mean flow.

Geometric considerations for forcing: distribution and orientation

Vortex generating jets (VGJs) and plasma actuators are topics of current research on active separation control methodologies. VGJs involve injection of fluid into the free-stream flow. The structure associated with injection through a discrete hole is a hairpin-like vortex (Zhang and Zhong, 2010). Even for injection in the span-wise direction, the hairpin vortices are seen to be oriented so that the legs align with the mean flow direction (Postl et al., 2011). Being highly localized, injection through a single hole is inherently three-dimensional.

Postl et al. (2011) and Gross and Fasel (2010) have hypothesized that intact span-wise vortices play a more important role in separation control than three-dimensional structures and breakdown to turbulence. The former authors showed that pulsed VGJs injecting flow in either stream-wise or span-wise directions had nearly identical effects of reducing the extent of separation; a two-dimensional component of the disturbance excited the inherent KH instability of the separated shear layer. The latter authors found harmonic blowing through a span-wise slot to be much more effective at separation control than a set of pulsed discrete VGJs with higher combined momentum. This was attributed to the high two-dimensional component of the slot flow, and corresponding suppression of three-dimensional structures that weaken the coherent span-wise vortices.

Note that the harmonic blowing through a slot is a case that Gross and Fasel (2010) considered to correspond to a conventional plasma actuator, such as used in this study: a two-dimensional (relatively long, non-distributed) span-wise oriented arrangement.

Frequencies of flow instability

As has been discussed previously, the disturbance of interest for transition of a laminar separation bubble corresponds to the inviscid Kelvin-Helmholtz (KH) instability of the inflectional separated shear layer for a broad range of conditions. The wavelength of the most unstable KH disturbance depends on the shape of the inflectional velocity profile of

the shear layer, and the thickness of the layer. The mean velocity profile between two parallel laminar flows of different velocities can be modeled, for example, as an idealized vortex sheet, by using a piece-wise linear approximation, or as a symmetric hyperbolic-tangent profile.

For a vortex sheet of infinitesimal thickness, the stream-wise wavelength λ of the disturbance that undergoes maximum KH instability growth is arbitrarily small, i.e., it has no lower limit. For a real free shear layer, such as that of a laminar separation bubble, the change in velocity occurs over a finite thickness.

This value may be calculated for the commonly used symmetric hyperbolic-tangent profile. The non-dimensional optimal frequency for KH instability, from Diwan and Ramesh (2009), is $\omega^* = (\pi/2).f.\delta_w/U_m$, where the mean velocity U_m is $(U_1 + U_2)/2$, and the vorticity thickness $\delta_w = (U_2 - U_1)/(\partial U/\partial y)_{max}$. Using data from Station 11 (non-dimensional stream-wise distance $s/L_{ss} \approx 0.76$), which is near the maximum bubble thickness, $U_2 \approx 4.65$ m/s, and $(\partial U/\partial y)_{max} \approx 2000\ s^{-1}$. The vorticity thickness is calculated to be $\delta_w \approx 2.3$ mm. Using $\omega^* \approx 0.22$ from the analysis of Monkewitz and Huerre (1982), the corresponding dimensional frequency for the present study is $f \approx 140$ Hz. While the analysis of Monketwitz and Huerre (1982) was developed for co-flowing layers only, others have found it to work well at the thickest part of a separation bubbles (Diwan and Ramesh, 2009), where a weak reversed flow may be present between the shear layer and the wall.

To further check for agreement with the literature, it is possible to use integral data from the boundary layer condition at the separation location, instead of using information from the thickest part of the bubble with the assumption of a tanh-like profile, as above. The non-dimensional frequency (Strouhal number) of maximum amplification based on these conditions is $St = f.\theta_s / U_{\infty,s}$, where θ_s is the momentum thickness of the boundary layer at separation, and $U_{\infty,s}$ is the free-stream velocity at the same location. Using data from Station 08 (incipient separation, $s/L_{ss} \approx 0.553$), $\theta_s \approx 0.4$ mm, and $U_{\infty,s} \approx 5.2$ m/s.

Using f = 140 Hz from the previous calculation, the Strouhal number St ≈ 0.011, similar to the value obtained by McAuliffe and Yaras (2010), and within the range of values of St ≈ (0.005 to 0.016) reported from the literature (Brinkerhoff and Yaras, 2011).

As an aside: it has been noted by some (such as Brinkerhoff and Yaras (2011)) that the most amplified TS frequency of the pre-separation boundary layer is very close to the KH instability frequency of the separated shear layer. Walker (1989) provided an equation for calculating the frequency of maximum TS wave growth, based on displacement thickness: $2\pi\nu f/U_\infty^2 = 3.2\ Re_{\delta*}^{-3/2}$. Using data from Station 8 ($s/L_{ss} \approx 0.553$), with $\delta* \approx 1$ mm, the frequency of interest for TS waves for the present study is calculated to be f ≈ 140 Hz, which is indeed similar to the KH instability frequency calculated above.

Optimal pulsing frequency for flow control

Despite the possibility of calculating a relatively distinct optimal frequency for flow control, as demonstrated above, experimental evidence from the literature indicates that a sharp peak in a spectrum of forcing frequencies is not usually found. Instead, a spread of effective frequencies exists.

For example, Volino (2002) reported that a broad band of frequencies were effective for flow control. Bons et al. (2002) found nearly no change in effectiveness for a range of forcing frequencies. Coull and Hodson (2011) noted that the distinct instability frequency predicted by Rayleigh analysis was usually absent in measurements. Accordingly, they found a range of frequencies in their measurement, rather than a sharp peak. Brinkerhoff and Yaras (2011) found that a range of Strouhal numbers of dominant instability existed in the literature: St = 0.005 to 0.016, where St is the Strouhal number based on free-stream velocity and momentum thickness at separation point.

Postl et al. (2011) also observed that an optimal frequency is often not present in experimental flow control data. Based on the results of their work, they proposed that forcing frequencies introduced into the flow generate a broad range of higher harmonic frequencies. As a result, for a forcing frequency that is equal to or less than the optimal

frequency, the flow "picks" the optimal frequency from the resultant broad band of higher harmonics. The effectiveness of flow control was found to decline rapidly for forcing frequencies higher than the optimal disturbance frequency. An additional consideration is the introduction into the flow of a large range of frequencies (in a Fourier decomposition sense) associated with the square wave nature of the on/off pulsing scheme.

Pulsed control parameters: present study

For this discussion, the data from the preliminary study on the effect of varying pulsing frequencies and duty cycles (sections 4.1 and 4.2) have been plotted along axes for the off time (t_{OFF}) versus on time (t_{ON}) of each pulsing cycle, in milliseconds (Figure 7-1). Lines of constant pulsing frequency and constant duty cycle are shown. The areas of the circles correspond to the relative effectiveness of separation control, measured as the gain of total pressure from the no-control case at a fixed probe location in the separation bubble. The tests involved variation of duty cycle at a constant pulsing frequency of 10 Hz (silver circles), and variation of pulsing frequency at a constant duty cycle of 20% (red circles). All cases had the same conditions of plasma discharge excitation frequency (600 Hz) and amplitude (16 kV_{p-p}).

Recall that the most unstable frequency calculated for this study is approximately 140 Hz, as calculated above. Comparing the set of cases in Figure 7-1 marked 'HF' to the 'LF' case, it is seen that despite dramatically different on-time periods and duty cycles (corresponding to power consumption of the actuator), the HF and LF cases have nearly the same effect on the separation bubble. As the pulsing frequency approaches the most unstable frequency, separation control becomes more efficient.

As pulsing frequency deviates to much lower frequencies, such as case LF, it takes significantly higher power to produce the same separation control effect as the HF cases. This is in agreement with the results of pulsed VGJ separation control of Volino et al.

(2011), who found that higher duty cycles or blowing velocities were needed at low pulsing frequencies.

Postl et al. (2011) postulated that the flow was able to pick out the most unstable frequency from a broad spectrum if the forcing frequency was the most unstable frequency, or lower. As discussed previously, at higher frequencies thereafter, the effectiveness of the actuator may be expected to drop off relatively rapidly. Based on these results, it can be expected that for the present study, as pulsing frequency is increased past the 85 Hz HF case shown in Figure 7-1, modest gains in separation control effectiveness will likely continue until a forcing frequency of approximately 140 Hz, the calculated most-unstable frequency for the flow, decreasing relatively quickly at higher frequencies.

Perspective of time scales and flow patterns induced by plasma actuator

Several recent studies showed that when a plasma actuator is initially switched on in quiescent air, fluid is entrained from around the actuator, and a coherent span-wise starting vortex is formed. If the actuator is not pulsed, the starting vortex continues to grows and move away from the actuator at an angle to wall. Growth continues until a critical distance between the vortex core and the feeding shear layer is reached; then the starting vortex separates from the shear layer (Sattari et al., 2012). The time scale for maximum growth ($t_{max\text{-}growth}$) of the starting vortex is typically in tens of milliseconds, and depends on the details of the global flow field. For the quiescent air cases of Sattari et al. (2012) and Benard and Moreau (2011), for example, this time scale is 20-30 ms.

For continuous operation, several recent studies (Kotsonis and Ghaemi, 2012; Sattari et al., 2012; Benard and Moreau, 2011) found that it takes a time scale $t_{start\text{-}up}$ of few (2 to 3) milliseconds after switching on the actuator to initiate the plasma discharge and produce an observable change in the flow field.

Kotsonis and Ghaemi (2012) observed that for pulsed flow induced by a plasma actuator in quiescent air, a train of discrete starting vortices is formed. They found that if the delay time of the pulses (off-time) was not sufficiently long, successive vortices merged into each other, forming a flow field that resembled the wall-jet flow of continuously-on case, lacking vortex structures. It appears reasonable that the timescale $t_{off\text{-}crit}$ for the minimum off-time needed for each starting vortex to completely leave the vicinity of the actuator and restore conditions for generation of the next discrete vortex should be related to the size and convection velocity of the vortices. A rough calculation from the data of Kotsonis and Ghaemi (2012) confirms this hypothesis. Based on the expected vortex sizes (O(mm)) and convection velocities (O(m/s)) in the non-quiescent situation of the present study, this time-scale can be expected to be on the order of a few milliseconds.

As can be inferred from the above discussion, the quantitative details depend on the specific flow field. Much of the available information from the most recent literature relates to induced flow in quiescent air; a majority of these studies consider continuous operation of the actuator only. However, a potentially useful qualitative picture of the flow patterns generated by the actuator may be visualized based on the existence of these time-scales.

Consider the flow control model sketched in Figure 7-2, in the same coordinate system as the results of Figure 7-1. Based on the $t_{max\text{-}growth}$ and $t_{off\text{-}crit}$ timescales, the map can be divided into zones A through D. The size of the starting vortices in a pulsed cycle can be expected to scale with increasing t_{ON}, until the limiting case of $t_{max\text{-}growth}$ is reached (zones A and B). For $t_{ON} \approx t_{max\text{-}growth}$, the growth of the starting vortex saturates, and the vortex separates from the actuator-induced shear layer for higher values of t_{ON}, as discussed above. Any additional on-time in the pulsing cycle drives the wall-jet behind the starting vortex (zones C and D).

Pulsing cases with $t_{off} < t_{off\text{-}crit}$ do not provide sufficient off-time to convect away the plasma induced flow features and restore the conditions for generating the next discrete

starting vortex. For these cases (zones A and C), a single leading starting vortex is produced when the actuator is first switched on; t_{off} is short enough that thereafter, the flow field resembles a continuously-on case.

The description of the experimental conditions for data point HF in Figure 7-1 indicate that at this low pulsing frequency of 10 Hz, duty cycles greater than about 80% showed poor repeatability. Based on the map of Figure 7-2, a possible explanation for this behavior is that the flow was at the boundary of zones C and D, fluctuating between occasionally producing a series of starting vortices, and producing a continuous wall jet. Based on the preceding discussion, efficient separation control depends on exciting frequencies that the flow is unstable to. The continuously-on configuration to increase momentum locally obtains all its energy from the plasma actuator; it is not an efficient means of flow control.

If the $t_{max\text{-}growth}$ for the flow field of the present study were in the 20-30 ms range observed in quiescent air, the trends of Figure 7-2 imply that a train of discrete partly-formed starting vortices is more effective for separation control than a less frequent series of mature starting vortices, or continuously-on flow.

The map of Figure 7-2 also includes a thin zone for cases of $t_{ON} < t_{start\text{-}up}$. As discussed above, it has been observed that a few (2 to 3) milliseconds of on-time is required to produce viable flow features. This observation places a limit on obtaining higher pulsing frequencies. For instance, in the present study, to obtain a pulsing frequency of the 140 Hz frequency of flow instability at 0.6 duty cycle, the plasma would have a corresponding on-time of 4 ms. If the process of forming a starting vortex did initiate, the vortex would receive a very small fraction of the on-time for growth. At much lower duty cycles, the production of flow features would likely cease altogether.

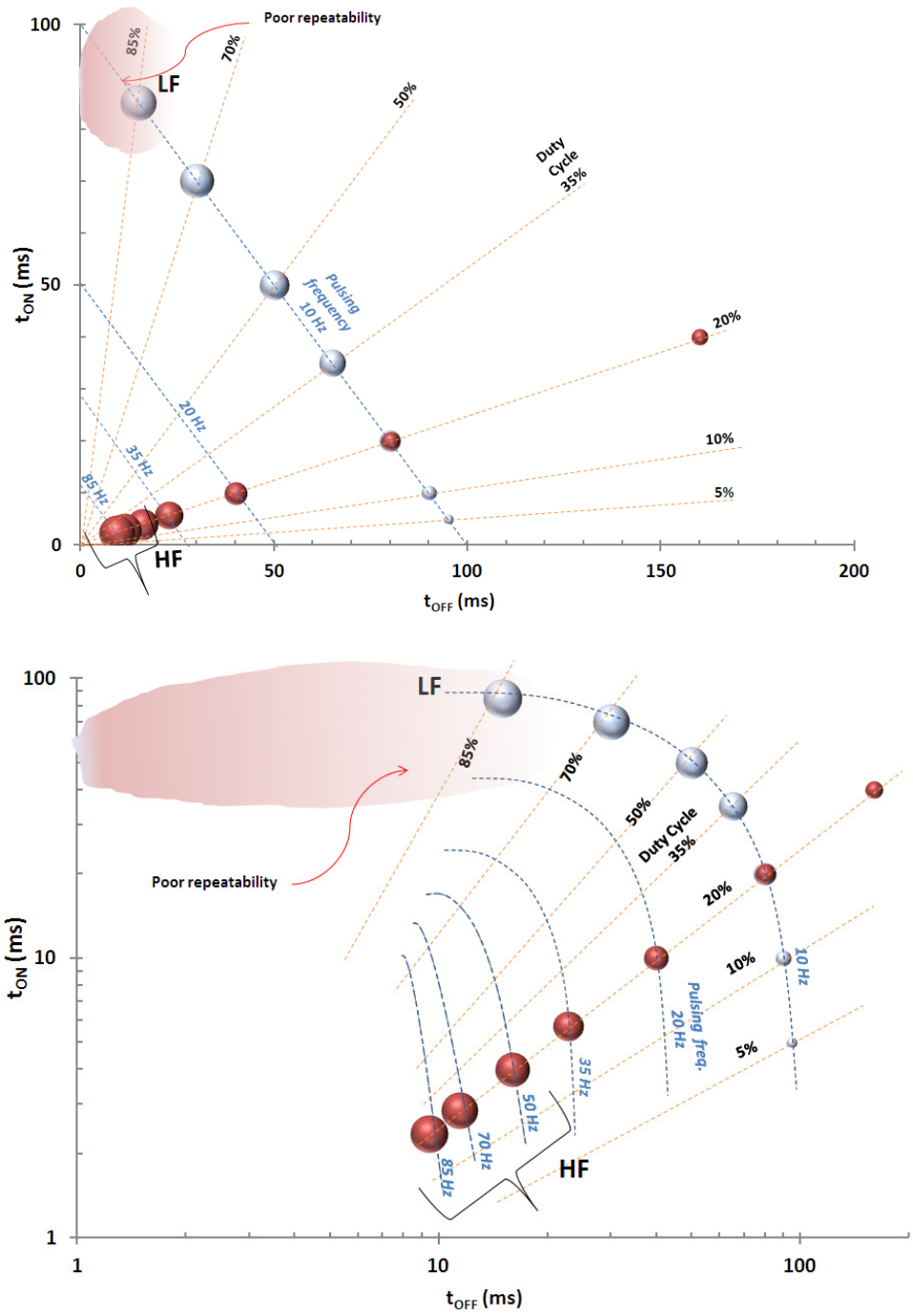

Figure 7-1 Rescaled results of parametric study of the effect of pulsing frequency and duty cycle (with linear and log scales). The areas of the circular markers correspond to a total pressure change as a measure of relative separation control effectiveness.

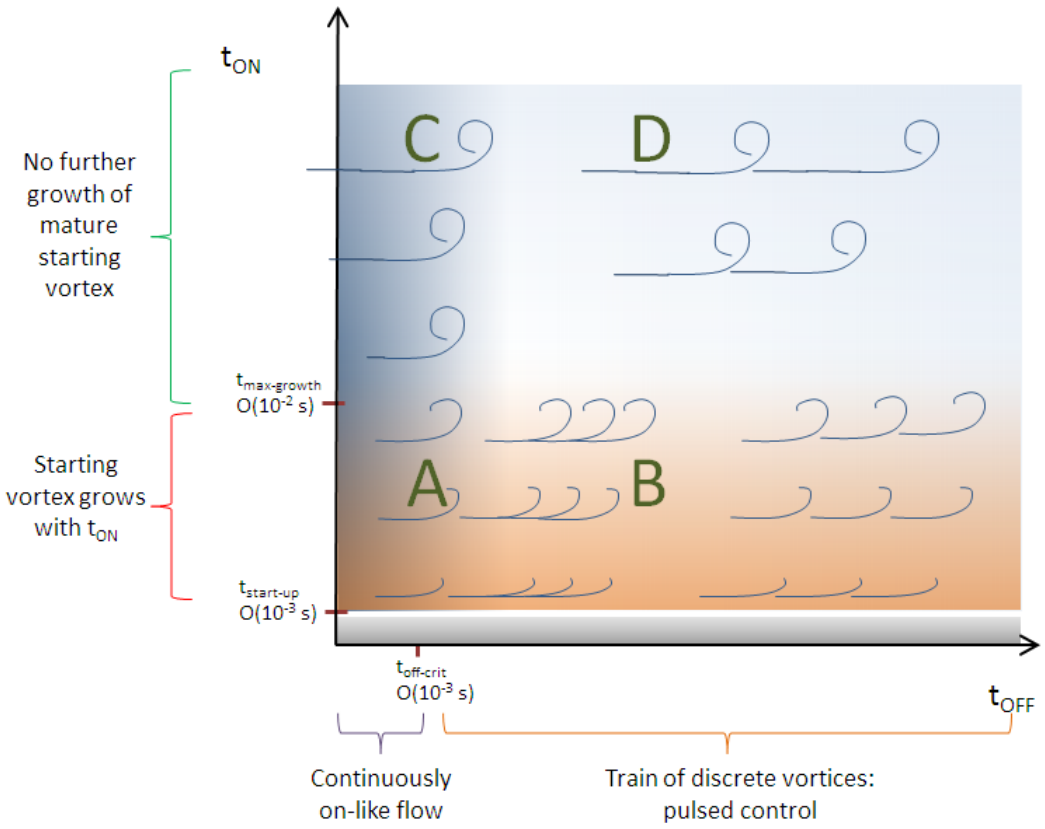

Figure 7-2 Schematic of flow control model based on size and patterns of vortices produced

8. Conclusions and recommendations

The efficiency of the low pressure turbine (LPT) strongly affects the overall engine efficiency, with suction surface flow separation being the primary contributor toward losses in the LPT. Incremental improvements in LPT component efficiency have major implications on engine fuel consumption, weight, and cost.

The present work demonstrates effective control of separation in a Pack-B LPT airfoil passage using a Dielectric Barrier Discharge (DBD) plasma actuator. The flow conditions, with a Reynolds number Re_{Lss} of 50,000 and inlet free-stream turbulence intensity of 2.5%, may be considered to be representative of a small engine at cruise conditions.

Preliminary experiments for characterizing actuator performance indicated that for pulsed operation of the actuator in the turbine airfoil facility, the extent of separation control authority monotonically increases with increasing pulsing frequency and duty cycle. In agreement with the literature, no obvious resonant frequencies or frequency bands were observed in the range tested. This suggests a broad band of effective frequencies. In another characterization study, the actuator was operated in a reversed orientation to successfully demonstrate separation control, suggesting that at least part of the control authority is due to disturbances destabilizing the separated laminar shear layer alone, rather than by near-wall momentum addition. Further comparison of the control due to a reversed actuator with an aligned one showed that the latter is more effective for flow control, possibly due to the higher shear strength in the thinner boundary layer that it produces, relative to the reversed actuator, and that higher shear leads to more upstream transition. Finally, a study of the edge effects of the plasma discharge, undertaken to investigate the role of span-wise flow variation on stream-wise transition location as well as to assess the two-dimensionality of the remaining flow field, demonstrated that considerably higher separation control authority is available near the actuator edges.

For the flow control study without passing wakes, total pressure measurements were taken with a glass tube, corrected for streamline displacement due to wall and shear effects, and validated using previous hot-wire data. Effective control of separation was demonstrated using a plasma actuator in two different configurations. The first configuration uses a buried grounded electrode located downstream of an exposed energized electrode. The other configuration adds a third electrode downstream of the first two electrodes. This third electrode is connected to the first exposed electrode when the latter is at a higher potential than the former, via a diode. Both configurations showed fully attached flow (or very thin separation zones) when the actuator was activated. The three-electrode configuration was somewhat more effective than the two-electrode configuration. The presence of the third electrode can limit performance by direct arcing, depending upon the applied signal and the distance between the exposed electrodes. The greater effectiveness of the three-electrode configuration was attributed to surface charge re-distribution due to the third electrode, leading to increased stream-wise acceleration of the charged particles in the plasma, which is imparted to the neutral fluid by collisions.

For the flow control study with passing wakes, velocity measurements were taken using hot-wire anemometry, corrected for near-wall effects, known temperature changes, and the interference of the plasma discharge during the active fraction of pulsed operation. The third electrode was electrically disconnected to prevent arcing with the hot-wire probe, but was left physically intact on the dielectric, in order to keep the airfoil surface hydro-dynamically unchanged from the study without wakes. Identical actuator geometry and signal parameters were used for both studies. The near-wall flow field in the aft section of the airfoil suction surface was found to be highly unsteady with the actuator off, with the passage of the wake periodically triggering a sequence of events: transition and re-attachment of the unstable, separated laminar shear layer; appearance of a thin, becalmed attached boundary layer; downstream movement of the re-attachment

point following the passage of the becalmed zone; and re-establishment of a separation bubble.

Measurements taken in the flow with passing wakes showed fully attached flow (or very thin separation zones) throughout the wake-passing cycle. The boundary layer showed nearly time-invariant behavior, and qualitatively closely resembled the boundary layer from the study without passing wakes and with the actuator on. This is noteworthy, since the two measurement sets were taken using entirely different instruments and experimental techniques.

Recommendations

The strong electric field associated with the plasma discharge present significant challenges for flow measurement in the vicinity.

The hot-wire measurement system can be affected by plasma actuator operation in several ways: interference and modification of the anemometer output voltage signal during the active fraction of pulsed operation; unexplained and repeated sudden failure of probes, with no obviously visible signs of physical damage to the sensor wire; and arcing damage to the probe due to physical proximity to the discharge. A non-intrusive technique, such as Particle Image Velocimetry (PIV) or Laser Doppler Velocimetry (LDV), appears to be an attractive alternative. However, to ensure that the measurements purely follow the motion of the fluid only, care must be taken to isolate or eliminate the response of seeding particles such as oil droplets to the electric field. Visualization techniques using tracers such as smoke can be subject to similar effects. Additionally, seeding particles have been observed to modify the characteristics of the plasma discharge. Care should taken to prevent this effect.

The nearly time-invariant nature of the attached boundary layer observed in this study with the actuator on suggests that it is potentially operating in “overkill” mode, and is an

excellent candidate for optimization. This is especially true when the naturally stabilizing effect of the becalmed region observed in the actuator off measurements is considered. Using open- or closed-loop feedback techniques, the actuator could be powered for only the fraction of the wake-passing cycle that is not influenced by the transition and re-attachment inducing passage of the wake, and the stabilizing becalmed period. Such optimization would dramatically reduce the power consumption of the actuator.

Bibliography

Adolfson, D. A. (2003). Oscillatory and Unidirectional Fluid Mechanics Investigations in a Simulation of a Stirling Engine Expansion Space. *Masters Thesis, University of Minnesota*.

Alam, M., & Sandham, N. D. (2000). Direct Numerical Simulation of Short Laminar Separation Bubbles With Turbulent Reattachment. *J. Fluid Mech.*

Andersson, P. (1999). Modelling of Boundary Layer Stability. *Technical Reports from Royal Institute of Technology*.

Andersson, P., Brandt, L., Bottaro, A., & Henningson, D. (2001). On the breakdown of boundary layer streaks. *J. Fluid Mech.*

Asada, K., Ninomiya, Y., Oyama, A., & Fujii, K. (2009). Airfoil flow experiment on the duty cycle . *AIAA 2009-531*.

Asai, M., Minagawa, M., & Nishioka, M. (2002). The instability and breakdown of a near-wall low-speed streak. . *J. Fluid Mech.*

Ashpis, D. E., & Thurman, D. R. (2011). DBD Plasma Actuators for Flow Control in Air Vehicles and Jet Engines - Simulation of Flight Conditions in Test Chambers by Density Matching. *NASA/TM 2011-217006/REV1*.

Baird, C., Enloe, C. L., McLaughlin, T. E., & Baughn, J. W. (2005). Acoustic testing of the dielectric barrier discharge (DBD) plasma actuator. *AIAA 2005-0565*.

Bearman, P. W., & Harvey, J. K. (1993, October). Control of circular cylinder flow by the use of dimples. *AIAA Journal*.

Benard, N., & Moreau, E. (2011). Separation Control by single nonthermal plasma discharge. *IEEE Trans. Plasma Sci.*

Bohl, D. G., & Volino, R. J. (2006). Experiments With Three-Dimensional Passive Flow Control Devices on Low-Pressure Turbine Airfoils. *J. Turbomachinery, 128*.

Boiko, A. V., Dovgal, A. V., Grek, G. R., & Kozlov, V. V. (2012). *Physics of Transitional Shear Flows.* Springer.

Bons, J. P., Hansen, L. C., Clark, J. P., Koch, P. J., & Sondergaard, R. (2005). Designing low-pressure turbine blades with integrated flow control. *ASME GT2005-68962*.

Bons, J. P., Sondergaard, R., & Rivir, R. B. (2002). The Fluid Dynamics of LPT Blade Separation Control Using Pulsed Jets. *ASME J. Turbomachinery*.

Brandt, L., Schlatter, P., & Henningson, D. S. (2004). Transition in boundary layers subject to free-stream turbulence. *J. Fluid Mech.*

Brinkerhoff, J. R., & Yaras, M. I. (2011). Interaction of viscous and inviscid instability modes in separation–bubble transition. *Phys. Fluids*.

Butler, K. M., & Farrell, B. F. (1992). Three-dimensional optimal perturbations in viscous shear flow. *Phys. Fluids*.

Chew, Y. T., Shi, S. X., & Khoo, B. C. (1995). On the Numerical Near-Wall Corrections of Single-Wire Measurements. *International Journal of Heat and Fluid Flow*.

Corke, T. C., & Matlis, E. (2000). Phased plasma arrays for unsteady flow control. *AIAA 2000-2323*.

Corke, T. C., Enloe, C. L., & Wilkinson, S. P. (2010). Dielectric Barrier Discharge Plasma Actuators for Flow Control. *Annu. Rev. Fluid Mech.*

Corke, T. C., Post, M. L., & Orlov, D. M. (2007). SDBD Plasma Enhanced Aerodynamics: Concepts, Optimization and Applications. *Prog. Aero. Sciences*.

Corke, T. C., Post, M. L., & Orlov, D. M. (2009). Single dielectric barrier discharge plasma enhanced aerodynamics: physics, modeling and applications. *Exp. Fluids*.

Corke, T., He, C., & Patel, M. (2004). Plasma flaps and slats: an application of weakly-ionized plasma actuators. *AIAA 2004-2127*.

Corke, T., Jumper, E., Post, M., Orlov, D., & McLaughlin, T. (2002). Application of weakly-ionized plasmas as wing flow-control devices. *AIAA 2002-0350*.

Coull, J. D., & Hodson, H. P. (2011). Unsteady boundary-layer transition in low-pressure turbines. *J. Fluid Mech.*

Criminale, W. O., Jackson, T. L., & Joslin, R. D. (2003). *Theory and Computation of Hydrodynamic Stability.* Cambridge University Press.

Debien, A., Bernard, N., David, L., & Moreau, E. (2012). Unsteady aspects of the electrohydrodynamic force produced by surface dielectric barrier discharge actuators . *Appl. Phys. Lett.*

Diwan, S. S., & Ramesh, O. N. (2009). On the origin of the inflectional instability of a laminar separation bubble . *J. Fluid Mech.*

Durbin, P., & Wu, X. (2007). Transition Beneath Vortical Disturbances. *Ann. Rev. Fluid Mech*.

Ellingsen, T., & Palm, E. (1975). Stability of linear flow. *Phys. Fluids*.

Enloe, C. L., McHarg, M. G., & McLaughlin, T. E. (2008). Time-correlated force production measurements of the dielectric barrier discharge plasma aerodynamic actuator. *J. Appl. Phys*.

Enloe, L., McLaughlin, T., VanDyken, R., Kachner, K., Jumper, E., & Corke, T. (2004). Mechanisms and Response of a Single Dielectric Barrier Plasma Actuator: Plasma Morphology. *AIAA Journal*.

Enloe, L., McLaughlin, T., VanDyken, R., Kachner, K., Jumper, E., Corke, T., et al. (2004). Mechanisms Mechanisms and Responses of a Single Dielectric Barrier Plasma Actuator: Geometric Effects. *AIAA Journal.*

Font, G. I., Enloe, C. L., McLaughlin, T. E., & Orlov, D. (2007). Plasma characteristics and experimentally determined boundary conditions for a plasma actuator. *45th AIAA Aerospace Sciences Meeting*.

Fransson, J. H., Brandt, L., Talamelli, A., & Cossu, C. (2004). Experimental and theoretical investigation of the nonmodal growth of steady streaks in a flat plate boundary layer. *Phys. Fluids*.

Fransson, J. H., Brandt, L., Talamelli, A., & Cossu, C. (2005). Experimental study of the stabilization of Tollmien–Schlichting waves by finite amplitude streaks. *Phys. Fluids*.

Gibbings, J. C. (1959). On Boundary-Layer Transition Wires. *Aeronautical Research Council, Current Papers*.

Glauert, M. B. (1956). The wall jet. *J. Fluid Mech*.

Gostelow, J. P., Walker, G. J., Solomon, W. J., Hong, G., & Melwani, N. (1997). Investigation of the Calmed Region Behind a Turbulent Spot. *ASME J. Turbomachinery*.

Greenblatt, D., Goksel, B., Rechenberg, I., Schule, C., Romann, D., & Paschereit, C. (2008). Dielectric Barrier Discharge flow control at very low flight Reynolds numbers. *AIAA Journal*.

Gregory, J., Enloe, C., Font, G., & McLaughlin, T. (2007). Force production mechanisms of a Dielectric-Barrier Discharge plasma actuator. *AIAA 2007-0185*.

Gross, A., & Fasel, H. F. (2010). Numerical Simulation of Low-Pressure Turbine Blade Separation Control. *AIAA Journal.*

Guo, S. (2010). private communication.

Häggmark, C. P., Bakchinov, A. A., & Alfredsson, P. H. (2000). Measurements with a flow direction boundary-layer probe in a two-dimensional laminar separation bubble. *Experiments in Fluids*.

Halfon, E., Nishri, B., Seifert, A., & Wygnanski, I. (2004). Effects of elevated free-stream turbulence on actively controlled separation bubble. *J. Fluids Engg*.

Halstead, D. E., Wisler, D. C., Okiishi, T. H., Walker, G. J., Hodson, H. P., & Shin, H.-W. (1997). Boundary layer development in axial compressors and turbines. *ASME J. Turbomachinery*.

Hodson, H. P. (1991). Aspects of Unsteady Blade-Surface Boundary Layers and Transition in Axial Turbomachines. *Boundary Layers in Turbomachines, VKI Lecture Series 1991–2006.*

Hodson, H. P., & Howell, R. J. (2005). Blade row interactions, transition, and high-lift airfoils in low-pressure turbines. *Ann. Rev. of Fluid Mech*.

Horton, H. P. (1968). Laminar Separation in Two and Three-Dimensional Incompressible Flow. *PhD Dissertation, University of London*.

Hourmouziadis, J. (1989). Aerodynamic Design of Low Pressure Turbines. *AGARD Lecture Series, 167*.

Howell, R. J., Ramesh, O. N., Hodson, H. P., Schulte, V., & Harvey, N. W. (2000). High lift and aft loaded profiles for low pressure. *ASME 264-GT-2000*.

Huang, J., Corke, T. C., Thomas, F. O., Ashpis, D., Hultgren, L., McLaughlin, T., et al. (2006). Plasma actuators for separation control of low-pressure turbine blades. *AIAA Journal*.

Huang, J., Corke, T., & Thomas, F. (2003). Plasma actuators for separation control of low pressure turbine blades. *AIAA 2003-1027*.

Hughes, J. D., & Walker, G. J. (2001). Natural Transition Phenomena on an Axial Compressor Blade. *ASME J. Turbomachinery*.

Hultgren, L. S., & Ashpis, D. E. (2003). Demonstration of Separation Delay with Glow-Discharge Plasma Actuators. *AIAA 2003-1025*.

Jacobs, R. G., & Durbin, P. A. (2001). Simulations of bypass transition. *J. Fluid Mech.*

Johnson, M. W. (2004). Receptivity calculations as a means to predicting transition. *NASA TM 2004-212913*.

Jolibois, J., Forte, M., & Moreau, E. (2008). Application of an AC barrier discharge actuator to control airflow separation above a NACA 0015 airfoil: Optimization of the actuation location along the chord. *J. Electrostatics*.

Jukes, T. N., & Choi, K.-S. (2012). Dielectric-barrier-discharge vortex generators: characterisation and optimisation for flow control. *Exp. Fluids*.

Jukes, T. N., Choi, K.-S., Johnson, G. A., & Scott, S. J. (2006). Characterization of Surface Plasma-Induced Wall Flows Through Velocity and Temperature Measurements. *AIAA Journal*.

Jukes, T. N., Choi, K.-S., Segawa, T., & Yoshida, H. (2008). Jet induced by a surface plasma actuator. *Proc. IMechE J. Systems and Controls Engineering*.

Kachanov, Y. S. (1994). Physical Mechanisms of Laminar-Boundary Layer Transition. *Annu. Rev. Fluid Mech.*

Kaszeta, R. W. (1998). Measurements in Film Cooling Flows with Lateral Injection. *M.S. Thesis, University of Minnesota*.

Kaszeta, R. W. (2000). Experimental investigation of transition to turbulence as affected by passing wakes. *Ph.D. Thesis, University of Minnesota*.

Kaszeta, R. W., & Simon, T. W. (2002). Experimental Investigation of Transition to Turbulence as Affected by Passing Wakes. *NASA/CR 2002-212104*.

Kaszeta, R. W., Simon, T. W., & Ashpis, D. E. (2001). Experimental Investigation of Transition to Turbulence as Affected by Passing Wakes. *ASME 2001-GT-195*.

Kaszeta, R. W., Simon, T. W., Ottaviani, F., & Jiang, N. (2003). The Influence of Wake Passing Frequency and Elevated Free Stream Turbulence Intensity on Transition in Low-pressure Turbines. *AIAA 2003-3633*.

Kim, J. (1990). Freestream turbulence and concave curvature effects on heated, transitional boundary layers. *Ph.D. Thesis, University of Minnesota*.

Kim, W., Do, H., Mungal, G., & Cappelli, M. (2007). On the role of oxygen in Dielectric Barrier Discharge actuation of aerodynamic flows. *Applied Physics Letters*.

Kotsonis, M., & Ghaemi, S. (2012). Experimental and numerical characterization of a plasma actuator in continuous and pulsed actuation. *Sensors and Actuators, Elsevier*.

Leger, L., Moreau, E., & Touchard, G. (2002). Effect of a DC Corona electrical discharge on the airflow along a flat plate. *IEEE Transactions on Industry Applications*.

Lin, J. C., Robinson, S. K., McGhee, R. J., & Valarezo, W. O. (1994). Separation control on high-lift airfoils via micro-vortex generators. *Journal of Aircraft*.

Little, J., Nishihara, M., Adamovich, I., & Samimy, M. (2009). Separation control from the flap of a high-lift airfoil using DBD plasma actuators. *AIAA 2009-145*.

Little, J., Takashima, K., Nishihara, M., Adamovich, I., & Samimy, M. (2010). High lift airfoil leading edge separation control with nanosecond pulse driven DBD plasma actuators. *AIAA 2010-4256*.

Liu, Y., Zaki, T. A., & Durbin, P. A. (2008). Boundary-layer transition by interaction of discrete and continuous modes. *J. Fluid Mech*.

Lundell, F. (2007). Reactive control of transition induced by free-stream turbulence: an experimental demonstration. *J. Fluid Mech.*

MacMillan, F. A. (1954). Viscous effects on Pitot tubes at low speeds. *J. R. Aero. Soc*.

MacMillan, F. A. (1956). Experiments on Pitot tubes in shear flow. *Ministry of Supply, Aero. Res. Council R & M 3028*.

Magnier, P., Hong, D., Leroy-Chesneau, A., Bauchire, J.-M., & Hureau, J. (2007). Control of separated flows with the ionic wind generated by a DC corona discharge. *Exp. Fluids*.

Mandal, A. C., & Dey, J. (2011). An experimental study of boundary layer transition induced by a cylinder wake. *J. Fluid Mech.*

Mandal, A. C., Venkatakrishnan, L., & Dey, J. (2010). A study on boundary-layer transition induced by free-stream turbulence. *J. Fluid Mech.*

Mans, J., de Lange, H. C., & van Steenhoven, A. A. (2007). Sinuous breakdown in a flat plate boundary layer exposed to free-stream turbulence. *Phys. Fluids*.

Mans, J., Kadijik, E. C., de Lange, H. C., & van Steenhoven, A. A. (2005). Breakdown in a boundary layer exposed to free-stream turbulence. *Exp. Fluids*.

Matsubara, M., Kozlov, V. V., Alfredsson, P. H., Bakchinov, A. A., & Westin, K. J. (1996). On flat plate boundary layer perturbations at high free stream turbulence level. *Proc. Eighth Internat. Conf. on Methods of Aerophysical Research*.

Mayle, R. E. (1991). The Role of Laminar-Turbulent Transition in Gas Turbine Engines. *ASME J. Turbomachinery*.

Mayle, R. E., Dullenkopf, K., & Schulz, A. (1998). The Turbulence That Matters. *ASME J. Turbomachinery*.

McAuliffe, B. R., & Yaras, M. I. (2010). Transition Mechanisms in Separation Bubbles under Low- and Elevated-Freestream Turbulence. *J. Turbomachinery*.

McKeon, B. J., Li, J., Jiang, W., Morrison, J. F., & Smits, A. J. (2003). Pitot probe corrections in fully developed turbulent pipe flow. *Meas. Sci. Technology*.

Meyer, R. X. (1958). The effect of wakes on the transient pressure and velocity distributions in turbomachines. *ASME J. Basic Engg.*.

Monkewitz, P. A., & Huerre, P. (1982). Influence of the velocity ratio on the spatial instability of mixing layers. . *Phys. Fluids*.

Morkovin, M. (1984). Bypass Transition to Turbulence and Research Desiderata. *Transition in Turbines, NASA Conf. Publ. 2386*.

Murphy, J. P., Kriegsis, J., & Lavoie, P. (2013). Scaling of maximum velocity, body force, and power consumption of dielectric barrier discharge plasma actuators via particle image velocimetry. *J. Appl. Phys.*

Nagabhushana Rao, V., Tucker, P. G., Jefferson-Loveday, R. J., & Coull, J. D. (2013). Large eddy simulations in low-pressure turbines: Effect of wakes at elevated free-stream turbulence. *Int. J. Heat Fluid Flow*.

Narasimha, R. (1998). *Minnowbrook II - Workshop on Boundary Layer Transition in Turbomachines*.

Neumann, M., Friedrich, C., Czarske, J., Kriegsis, J., & Grundmann, S. (2013). Determination of the phase-resolved body force produced by a dielectric barrier discharge plasma actuator. *J. Phys. D: Appl. Phys.*

Olson, D. H., Reimann, D., Bloxham, M., & Bons, J. P. (2005). The effect of elevated freestream turbulence on separation control with Vortex-Generating Jets. *AIAA 2005-1114*.

Opaits, D., Roupassov, D., Starikovskaia, S., Starikovskii, A., Zavialov, I., & Saddoughi, S. (2005). Plasma Control of Boundary Layer using Low-Temperature Non-Equilibrium Plasma of Gas Discharge. *AIAA 2005-1180*.

Orlov, D. M. (2006). Modelling and simulation of single dielectric barrier discharge plasma actuators. *Dissertation, University of Notre Dame*.

Patel, M., Ng, T., Vasudevan, S., Corke, T., Post, M., McLaughlin, T., et al. (2008). Scaling effects of an aerodynamic plasma actuator. *Journal of Aircraft*.

Poon, D. (2011). Separation Control using Plasma Actuators: Experimental Studies of Plasma Actuator Performance. *M.S. Thesis, University of Minnesota*.

Porter, C. O., Baughn, J. W., McLaughlin, T. E., Enloe, C. L., & Font, G. I. (2006). Temporal force measurements on an aerodynamic plasma actuator. *44th AIAA Aerospace Sciences Meeting*.

Post, M., & Corke, T. (2003). Separation control on high angle of attack airfoil using plasma actuators. *AIAA Paper 2003-1024*.

Postl, D., Balzer, W., & Fasel, H. F. (2011). Control of laminar separation using pulsed vortex generator jets: direct numerical simulations. *J. Fluid Mech.*

Postl, D., Gross, A., & Fasel, H. F. (2003). Numerical investigation of low-pressure turbine blade separation control. *AIAA-2003-0614*.

Qiu, S. (1996). An experimental study of laminar to turbulent flow transition with temporal and spatial acceleration effects. *Ph.D. thesis, University of Minnesota*.

Reed, H. L., Saric, W. S., & Arnal, D. (1996). Linear Stability Theory Applied to Boundary Layers. *Annu. Rev. Fluid Mech*.

Reshotko, E., & Tumin, A. (2006). Application of Transient Growth Theory to Bypass Transition. *IUTAM Symposium on One Hundred Years of Boundary Layer Research*.

Roth, J. R., & Dai, X. (2006). Optimization of the Aerodynamic Plasma Actuator as an Electrohydrodynamic (EHD) Electrical Device. *AIAA 2006-1203*.

Roth, J. R., Sherman, D., & Wilkinson, S. (1998). Boundary Layer Flow Control with One Atmosphere Uniform Glow Discharge Surface Plasma. *AIAA-98-0328*.

Roupassov, D. V., Nikipelov, A. A., Nudnova, M. M., & Starikovskii, A. Y. (2009). Flow Separation Control by Plasma Actuator with Nanosecond Pulsed-Periodic Discharge. *AIAA Journal*.

Samimy, M., Breuer, K. S., Leal, L. G., & Steen, P. H. (2003). *A Gallery of Fluid Motion.* Cambridge University Press.

Saric, W. S., Reed, H. L., & Kerschen, E. J. (2002). Boundary-Layer Receptivity to Freestream Disturbances. *Annu. Rev. Fluid Mech*.

Sattari, P., Rival, D. E., Martinuzzi, R. J., & Tropea, C. (2012). Growth and separation of a start-up vortex from a two-dimensional shear layer. *Phys. Fluids*.

Sayadi, T., Hamman, C. W., & Moin, P. (2011). Direct numerical simulation of H-type and K-type transition to turbulence. *Annual research briefs, Stanford Center for Turbulence Research*.

Schmid, P. J., & Henningson, D. S. (2001). *Stability and Transition in Shear Flows*. Springer.

Schobeiri, M. T., Read, K., & Lewalle, J. (2003). Effect of unsteady wake passing frequency on boundary layer transition, experimental investigation, and wavelet analysis. *J. Fluids Engg*.

Schubauer, G. B., & Klebanoff, P. S. (1955). Contributions on the Mechanics of Boundary Layer Transition. *NACA TN 3489 1955/NACA Rep. 1289 1956*.

Schubauer, G. B., & Skramstad, H. K. (1948). Laminar Boundary Layer Oscillations and Transition on a Flat Plate. *NACA Report 909*.

Seifert, A., Theofilis, V., & Joslin, R. D. (2002). Issues in Active Flow Control: Theory, Simulation and Experiment. *AIAA 2002-3277*.

Seifert, A., Theofilis, V., & Joslin, R. D. (2002). Issues in Active Flow Control: Theory, Simulation and Experiment. *AIAA 2002-3277*.

Sharma, O. (1998). Impact of Reynolds Number on Low Pressure Turbine Performance. *NASA CP-1998-206958*.

Simon, T. W., & Kaszeta, R. W. (2001). Transition to turbulence under low-pressure turbine conditions. *Annals of the New York Academy of Sciences*.

Simon, T. W., Qiu, S., & Yuan, K. (2000). Measurements in a transitional boundary layer under low-pressure turbine airfoil conditions. *NASA/CR-2000-209957*.

Simoni, D., Uhaldi, M., Zunino, P., & Bertini, F. (2012). Transition mechanisms in laminar separation bubbles with and without incoming wakes and synthetic jet effects. *Exp. Fluids*.

Solomon, W. J. (2000). Effects of Turbulence and Solidity on the Boundary Layer Development in a . *ASME 2000-GT-0273*.

Sondergaard, R., Rivir, R. B., & Bons, J. P. (2002). Control of low-pressure turbine separation using vortex-generator jets. *J. Prop. Power*.

Sosa, R., Artana, G., Grondona, D., Kelly, H., Marquez, A., & Minotti, F. (2007). Discharge characteristics of plasma sheet actuators. *J. Phys.D: Applied Physics*.

Stadtmüller, P., Fottner, L., & Fiala, A. (2000). Experimental and Numerical Investigation of Wake-Induced Transition on a Highly Loaded LP Turbine at Low Reynolds Numbers. *ASME 2000-GT-0269*.

Stieger, R. D., & Hodson, H. P. (2004). Convection of a turbulent bar wake through a low-pressure turbine cascade. *ASME GT2004-53061*.

Suder, K. S., O'Brien, J. E., & Reshotko, E. (1988). Experimental Study of Bypass Transition in a Boundary Layer. *NASA Tech. Memorandum 100913*.

Sung, Y., Kim, W., Mungal, M. G., & Capelli, M. A. (2006). Aerodynamic Modification of Flow over Bluff Objects by Plasma Actuation. *Experiments in Fluids*, 479-486.

Thomas, F. O., Corke, T. C., Iqbal, M., Kozlov, A., & Schatzman, D. (2009). Optimization of Dielectric Barrier Discharge Plasma Actuators for Active Aerodynamic Flow Control. *AIAA Journal*.

van Ingen, J. L. (2008). The e^N method for transition prediction. Historical review of work at TU Delft. *AIAA 2008-3830*.

Volino, R. J. (2002). Separated Flow Transition Under Simulated Low-Pressure Turbine Airfoil Conditions: Part 1- Mean Flow and Turbulence Statistics. *ASME J. Turbomachinery*.

Volino, R. J. (2002). Separated Flow Transition Under Simulated Low-Pressure Turbine Airfoil Conditions: Part 2 - Turbulence Spectra. *ASME J. Turbomachinery*.

Volino, R. J. (2003). Separation Control on Low-Pressure Turbine Airfoils Using Synthetic Vortex Generator Jets. *ASME 2003-GT-38729*.

Volino, R. J., & Simon, T. W. (1995). Measurements in Transitional Boundary Layers Under High Free-Stream Turbulence and Strong Acceleration Conditions. *NASA Contractor Report 198413*.

Volino, R. J., Kartuzova, O., & Ibrahim, M. B. (2009). Experimental and computational investigations of low-pressure turbine separation control Using Vortex Generator Jets. *ASME GT2009-59983*.

Volino, R. J., Kartuzova, O., & Ibrahim, M. B. (2011). Separation control on a very high lift low pressure turbine airfoil using pulsed vortex generator jets. *ASME J. Turbomachinery*.

Walker, G. J. (1989). Transitional Flow on Axial Turbomachine Blading. *AIAA Journal.*

Wang, J.-J., Choi, K.-S., Feng, L.-H., Jukes, T. N., & Whalley, R. D. (2013). Recent developments in DBD plasma flow control. *Prog. Aero. Sciences*.

Wang, T. (1984). An experimental investigation of curvature and freestream turbulence effects on heat transfer and fluid mechanics in transitional boundary layer flows. *Ph.D. Thesis, University of Minnesota*.

Whalley, R. D., & Choi, K.-S. (2010). Starting, traveling, and colliding vortices: Dielectric-barrier-discharge plasma in quiescent air. *Phys. Fluids*.

Whalley, R. D., & Choi, K.-S. (2012). The starting vortex in quiescent air induced by dielectric-barrier-discharge plasma. *J. Fluid Mech.*

Wilson, D. J. (1970). An experimental investigation of the mean velocity, temperature, and turbulence fields in plane and curved two-dimensional wall jets: Coanda effect. *Ph.D. Thesis, University of Minnesota*.

Wisler, D. C. (1998, February 9-12). The technical and economic relevance of understanding Blade Row interactions effects in turbomachinery. *von Karman Institute for Fluid Dynamics Lecture series 1998-02*.

Yajnik, K. S., & Gupta, R. P. (1973). A new probe for measurement of velocity and flow direction in separated flows. *J. Phys. E: Sci. Instrum*.

Yaras, M. I. (2001). Measurements of the effects of pressure-gradient history on separation-bubble transition. *ASME 2001-GT-0193*.

Yuan, K. (1999). Simulation of wakes: The development of a linear cascade wake generator. *M.S. Thesis, University of Minnesota*.

Zaki, T. A., & Durbin, P. (2005). Mode Interaction and the Bypass Route to Transition. *J. Fluid Mech.*

Zhang, S., & Zhong, S. (2010). Experimental Investigation of Flow Separation Control Using an Array of Synthetic Jets. *AIAA Journal.*

Zhang, X. F., & Hodson, H. (2004). Combined Effects of Surface Trips and Unsteady Wakes on the Boundary Layer Development of an Ultra-High-Lift LP Turbine Blade. *ASME J. Turbomach*.

Zhong, S., Kittichaikarn, C., Hodson, H. P., & Ireland, P. T. (1998). A study of unsteady wake-induced boundary layer transition with thermochromic liquid crystal. *IMECH Conf. Opt. Methods Data Process. Heat Fluid Flow*.

Appendix – Dielectric selection for the plasma actuator

In collaboration with other researchers at the University of Minnesota, early parts of this study were conducted with different grades, thicknesses, and layered combinations of range of dielectric materials, including alumina, Kapton, PET, PMMA, and mica.

Polymer-based dielectrics were initially especially attractive because they are available in thin sheets that conform easily to airfoil shapes without significantly altering the shape of the profile. Several of these materials offer high dielectric breakdown strength, typical specified in kV/mm, theoretically assuring failure-free performance at the signal amplitudes of interest. Other parameters being equal, it was also expected that a thin dielectric would offer lower dielectric losses (Roth and Dai, 2006) than a more massive dielectric.

Two major issues characterized these preliminary experiments:

a) Rapid failure of polymer-based dielectrics due to burn-through, requiring frequent and time-consuming re-testing with a freshly fabricated actuator.

Failure occurred approximately once for every hour of plasma operation. Discussions with collaborators at the University of Minnesota concluded that this failure was likely due to attack by oxygen radicals formed during the discharge. Figure A-1 shows burn-through failure occurring during a test with Kapton as the dielectric material. The flash of light seen is an electric arc forming between the high voltage electrodes, passing through the failure site in the dielectric. Figure A-2 shows a close-up of the site of the failure in a PET polyester dielectric. The scale shown is in millimeters.

Efforts to overcome this failure included experimenting with multiple thin layers sandwiched together, and using a top layer of Kapton CR (a grade of Kapton specifically developed by DuPont to be resistant to corona discharges). Thicker samples of polyester were found to last for several hours before failure. These were first approximately molded to the shape of the suction surface of the airfoil by careful operation of a heat gun over a template (Figure A-5).

Since the need for frequent replacement made gluing impractical, these dielectrics were attached to a specially-machined recess in the airfoil using a vacuum pump. Vacuum grease was used to seal the perimeter and reduce through-flow of air. Silver paint was used to enhance electrical contact with the connectors.

b) Saturation of the discharge, where increasing input signal amplitude provided no significant increase in flow control authority.

Saturation is accompanied by formation of coarse, bright streamers in the discharge. Typical electrical characteristics of the discharge at saturation are shown in Figure A-3. The input waveform from the function generator shows the original sinusoidal form of the signal. The current waveform of the plasma discharge resembles a heavily clipped sinusoid, with large discharge current spikes corresponding to the streamer channels superposed on it. The discharge voltage has been distorted into a nearly triangular waveform. Figure A-4 (Thomas et al., 2009) shows the visual appearance of streamers at the saturation condition.

The high-voltage amplifier that was used for these early studies (Trek 20/20C) was replaced by a model (Trek PD05034-L) with noticeably improved slew rate, large signal bandwidth, and peak output current ratings.

Table 2-3 compares the specifications of both devices. Significantly, testing with thicker dielectrics was also found to alleviate this issue. As others have also noted (Thomas et al., 2009), thicker dielectrics permit the application of larger amplitude signals before the onset of saturation.

An impedance-matching circuit was also considered to optimize power transfer by minimizing the power reflected back to the amplifier, but was not pursued due to the high cost of the circuit components needed for this high voltage application.

Following the persistent failure of the thin and relatively flexible materials described above, the following dielectric materials were considered: glass, quartz, and MACOR. While MACOR is a machinable ceramic, discussions with machinists at the University of Minnesota suggested that it can be quite fragile, and prone to breaking up when clamped. Quartz has a softening temperature of about 1700 ºC, which was beyond the capability of the furnace facilities available. Glass was selected as an appropriate dielectric material for fabricating into a suitable actuator. Based on the expected voltages, the dielectric breakdown strength of glass, and material availability, 1.3 mm thick sheets of glass were obtained.

To fabricate a glass dielectric of the correct shape, a mandrel in two parts was machined out of graphite in the shape of the Pack-B suction surface profile. A flat glass sheet was pinned at the trailing edge of the convex lower section of the mandrel, and the assembly was placed in an oven. When the oven reached a temperature of approximately 700 ºC (1300 °F), the glass sheet would soften sufficiently to slump loosely over the mandrel. At this point, the oven was briefly opened, and the concave upper section of the mandrel was carefully placed over the slumped glass sheet. The oven was closed again, and held at temperature until the glass sheet sandwiched within the two sections of the mandrel perfectly conformed to the prescribed contour.

Graphite was selected as a material for the mandrel because it retained its integrity at the high temperatures used, was relatively easy to machine, and had a smooth machined surface that transferred to the glass surface well. It was, however, prone to rapid oxidation during the cooling phase, leading to the outer surfaces becoming porous and eventually disintegrating. Machined fire-brick was also attempted, but it was not possible to achieve an acceptable surface finish. It was also challenging to cool down the mandrel/dielectric assembly to room temperature without unacceptable warping of the glass surface.

Eventually, a single sample of glass dielectric was obtained that was acceptably free of defects. The results documented in this thesis were obtained using this sample.

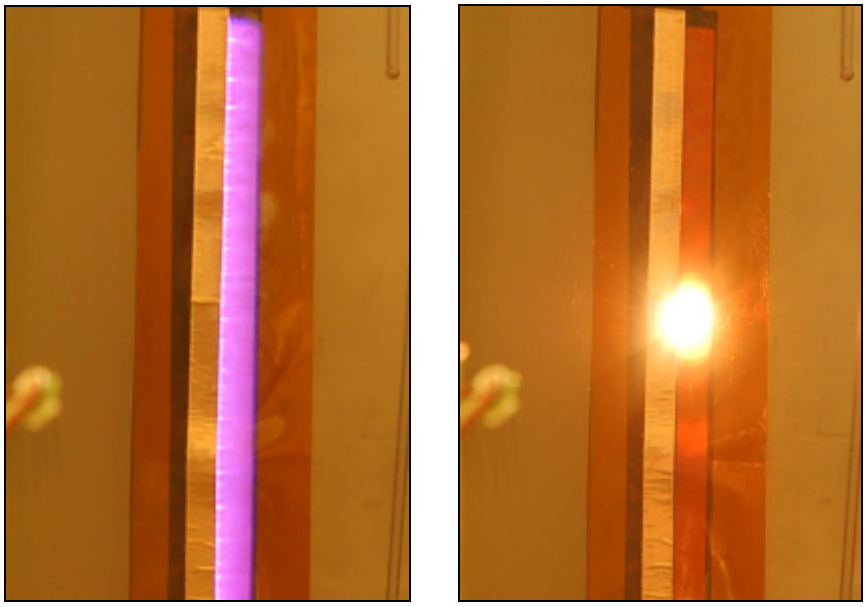

Figure A-1 The actuator showing the DBD plasma discharge during normal operation (left), and at the instant of burn-through failure (right).

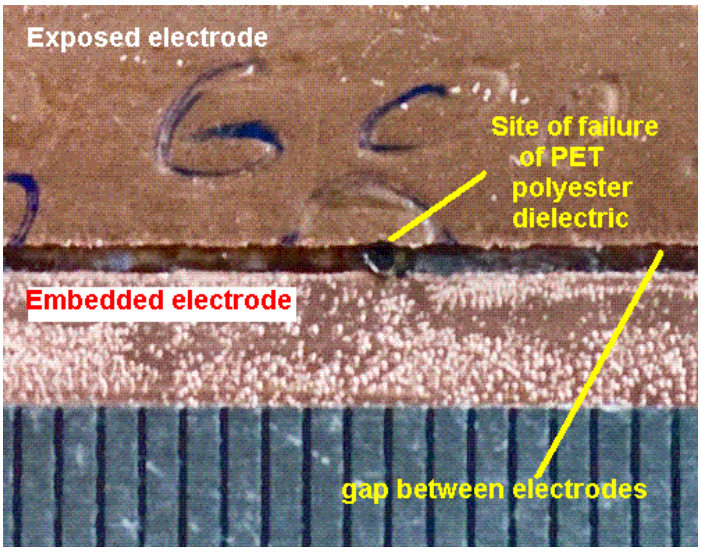

Figure A-2 PET polyester dielectric showing the site of the burn-through failure typical of early experiments undertaken during this study. The scale is in millimeters.

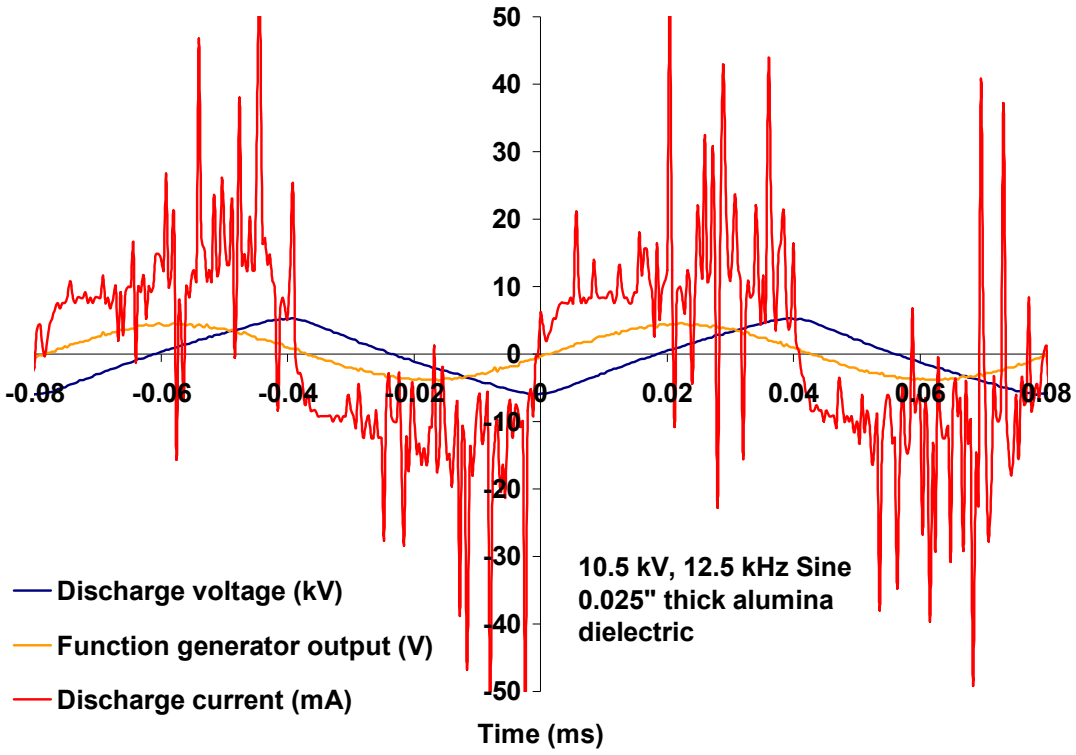

Figure A-3 Electrical characteristics of the discharge at saturation conditions.

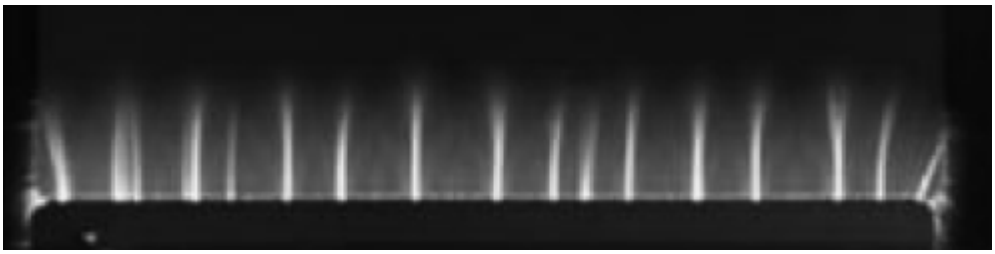

Figure A-4 Structure of discharge at saturation, showing coarse, bright streamers (Thomas et al., 2009).

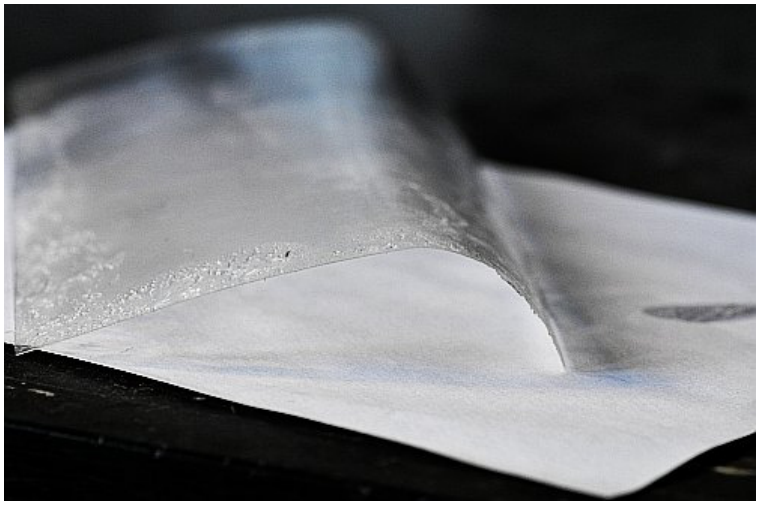

Figure A-5 A dielectric sample that was deformed by use of a heat gun, to better conform to the airfoil shape. The residue is vacuum grease.

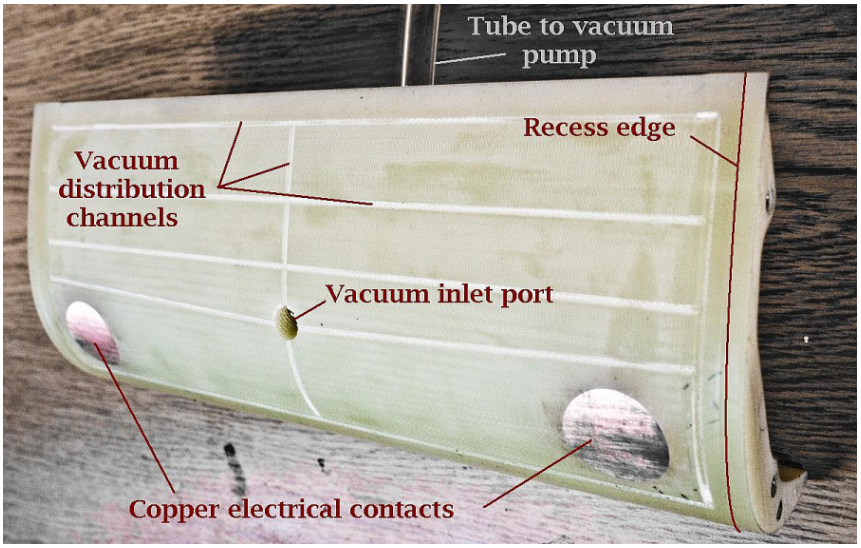

Figure A-6 A replaceable airfoil insert section for the Pack-B low-pressure turbine experiment.